Aus der Klinik für Neurochirurgie mit Arbeitsbereich Pädiatrische Neurochirurgie

der Medizinischen Fakultät Charité – Universitätsmedizin Berlin

DISSERTATION

Effects of ephrinB2 – EphB4 signaling on spinal metastasis

zur Erlangung des akademischen Grades
Doctor of Philosophy in Medical Neurosciences
(Ph.D. in Medical Neurosciences)

im Rahmen des
International Graduate Program Medical Neurosciences

vorgelegt der Medizinischen Fakultät
Charité – Universitätsmedizin Berlin

von

Thomas Broggini

aus Heiden, Schweiz

Datum der Promotion: 4.09.2015

Contents

1 Abstract

1.1 Introduction

The incidence of spinal metastasis has been increasing constantly over the last 20 years as a consequence of improved diagnostics and oncological therapy. Spinal metastases require extensive surgical intervention in the case of spinal instability or in the presence of a neurological deficit, which impose a significant burden to patients. While surgical procedures are becoming more and more complex for treating spinal metastasis, the molecular principles remain elusive. EphB4 – ephrinB2 has been linked to organ-specific tumor cell dissemination by mediating tumor cell – endothelial cell adhesion and repulsion. In this study we investigated the effect of EphB4 – ephrinB2 interaction on B16 tumor cell dissemination and long-term metastasis formation.

1.2 Methods

B16-F1 melanoma were lentivirally infected with a firefly luciferase, green fluorescence protein, puromycin resistance construct (B16-luc). Spinal metastasis of these cells were explanted and recultivated (mB16-luc). EphB4 was retroviraly overexpressed in B16-luc (B16-luc-EphB4). The cells were *in-vitro* characterized for proliferation (MTT), migration (wound healing) and EphB4 gene expression (qPCR / Immunoblot). After retrograde left carotid artery injection, metastasis formation was observed by *in-vivo* bioluminescence imaging. Spinal metastases were identified by T2 small animal magnetic resonance imaging. Number of disseminated cells / metastasis was measured after tissue homogenization using *ex-vivo* bioluminescence. The experiments were performed in wild type and inducible endothelial ephrinB2 knockout animals (iΔ*efnb2).*

1.3 Results

Endothelial ephrinB2 depletion (1738 ± 806 cells) or EphB4 kinase inhibition (1009 ± 334 cells), led to increased tumor cell dissemination. EphB4 overexpression reduced osseous dissemination of tumor cells (bone: 322 ± 90 cells other: 612 ± 206 cells). In long-term metastasis experiments, the time to neurological deficit was significantly

reduced in i∆*efnb2* animals (i∆*efnb2* median: 21 days, control median: 26 days). Number of spinal metastasis (control: 1.2 ± 0.4472, i∆*efnb2*: 3.2 ± 1.643) and tumor volume (control: 2.815mm^3 ± 2.558mm^3 and i∆*efnb2* 9.999mm^3 ± 5.596mm^3) was significantly increased in i∆*efnb2* mice. In contrast, EphB4 overexpression significantly reduced spinal metastasis number (B16-luc-pLXSN: 1.4 ± 0.5477, B16-luc-EphB4: 0.4 ± 0.5477). Secondary metastatic tumor cells (mB16-luc) lead to increased, organ unspecific cell dissemination. Long-term metastasis showed faster neurological deficits (B16-luc median: 26 days, mB16-luc median: 22 days), higher number of spinal metastasis (B16-luc 1.2 ± 0.4472, mB16-luc 3.8 ± 1.643) and increased tumor volume in the spine (B16-luc 2.815mm^3 ± 2.558mm^3 and mB16-luc 9.209mm^3 ± 5.561mm^3).

1.4 Conclusion

We found generally increased aggressiveness of sequential metastatic cells *in-vivo*. Endothelial ephrinB2 depletion mediates metastasis formation to the spine and may predispose to increased metastasis formation in osseous organs. EphB4 overexpression on tumor cells decreased spinal metastasis. This research helps facilitate the development of a priory-targeted therapy for spinal metastasis.

2 Abstrakt

2.1 Einführung

Die Entstehung klinisch relevanter spinaler Metastasen ist in den vergangenen 20 Jahren stetig gestiegen. Diese Prognose limitierende onkologische Manifestation kann momentan nicht suffizient therapiert werden. Die molekularen Mechanismen, welche dieser Krankheit zu Grunde liegen, sind weitestgehend unbekannt. Tumorzell – Endothelzell-Interaktionen vermitteln die Extravasation von Tumorzellen und nehmen damit bei der Entstehung von Metastasen eine entscheidende Rolle ein. Der EphrinB2 – ephB4 Signalweg vermittelt in diesem Zusammenhang Tumorzell – Endothelzell-Interaktionen und könnte damit eine zentrale Rolle in der Pathophysiologie dieser Erkrankung einnehmen. In dieser Studie wurde der Effekt des EphrinB2-ephB4-Systems auf die Dissemination von B16 Melanomzellen und die Manifestation von spinalen Metastasen untersucht.

2.2 Methodik

Luziferase infizierte B16-F1 Melanomzellen (B16-luc) sowie EphB4 überexprimierende Tumorzellen (B16-luc-EphB4) wurden retrograd über die Arteria carotis interna in die Aorta descendens injiziert. Spinale Metastasen dieser Zellen wurden explantiert und rekultiviert (mB16-luc). Alle Zellen wurden in-vitro auf Proliferation (MTT), Migration (Wundheilungs assay) und Genexpression von EphB4 (qPCR / Immunoblot) charakterisiert. Die Metastasenbildung wurde mittels *in-vivo* Biolumineszenzbildgebung überwacht. Bei Nachweis spinaler Metastasen wurden die Größe und Anzahl mittels T2 Kleintier-Magnetresonanztomographie charakterisiert. Anschließend wurden die Organe extrahiert. Mittels Gewebehomogenisation sowie anschließender Lumineszenzanalyse wurde die Anzahl disseminierter Tumorzellen bzw. metastatischer Tumorzellen pro Organ bestimmt. Die Experimente wurden in Kontrollen und induzierbaren endothelspezifischen ephrinB2 knockout Tieren (iΔ*efnb2*) durchgeführt.

2.3 Ergebnisse

Die Depletion von ephrinB2 auf dem Endothel (1738 ± 806 Zellen) oder die Inhibition der EphB4 Kinase (1009 ± 334 Zellen) führten zu einer verstärkten Tumorzelldissemination, während im Gegensatz dazu eine EphB4 Überexpression zu einer reduzierten ossären Dissemination führte (Knochen: 322 ± 90 Zellen, Weichteilorgane: 612 ± 206 Zellen). Dementsprechend zeigten iΔ*efnb2* Tiere eine signifikant erhöhte Metastasierung (Kontrolle: 2.815mm^3 ± 2.558mm^3, iΔ*efnb2*: 9.999mm^3± 5.596mm^3) mit multiplen spinalen Metastasen (Kontrolle: 1.2 ± 0.4472, iΔ*efnb2*: 3.2 ± 1.643) sowie ein korrespondierend früher einsetzendes neurologisches Defizit als Kontrolltiere (iΔ*efnb2* median: 21 Tage, Kontrolle: median: 26 Tage). Unter Überexpression von EphB4 wurde eine signifikante Reduktion spinaler Metastasen beobachtet (B16-luc-pLXSN:1.4 ± 0.5477, B16-luc-EphB4: 0.4 ± 0.5477) mit einem signifikant später einsetzenden neurologischen Defizit. Die Reinjektion von spinal metastasierten Tumorzellen (mB16-luc) hatte eine organunspezifische Dissemination zur Folge mit einer unspezifischen Erhöhung spinaler Metastasen (B16-luc: 1.2 ± 0.4472, mB16-luc: 3.8 ± 1.643) und einem früher einsetzenden neurologischen Defizit (B16-luc median: 26 Tage, mB16-luc median: 22 Tage) im Vergleich zur Kontrollgruppe (B16-luc median: 26 Tage, mB16-luc median: 22 Tage).

2.4 Schlussfolgerung

EphrinB2 – EphB4-Interaktionen spielen eine zentrale Rolle bei der organspezifischen Metastasierung mittels Steuerung der Tumorzelldissemination. Insbesondere bei der Entstehung experimenteller spinaler Metastasen stellt dieser Signalweg damit ein vielversprechendes therapeutisches Ziel dar.

3 Introduction

3.1 Clinical significance

The incidence of spinal metastasis has developed to a major problem in the treatment of cancer patients [1]. Of total metastatic cancer patients, 70% will develop spinal metastasis and 10% will develop tumors, with significant myelon compression and neurological deficits [1-3]. The most common tumors that develop spinal metastasis are mamma-, lung-, renal cell and prostate carcinoma [1-3]. The development of spinal metastasis significantly reduces clinical prognosis and results in a massive clinical burden. The destruction of the bone structures by the tumor leads to spinal instability. This results in massive and chronic pain. Additionally, spinal metastases are the most common cause of oncologically induced paraplegia. The National Institute of Health Annual Report to the Nation on the Status of Cancer (USA; 1998) revealed a 500 fold increase in the incidence rate of spinal metastasis during the past 20 years. This increase is generated by improved diagnostics and therapy of primary tumors. Hence, spinal surgery techniques have evolved from palliative laminectomy to complex reconstruction and fixation of the spine in order to improve patient outcome and quality of life. Despite surgical improvements, understanding of spinal metastatic formation on a molecular level is lacking and therefore there are currently no targeted, adjuvant therapies available. Gold standard therapy to date involves resection of the primary and metastatic tumors, chemotherapy and radiation. The combination of the available therapeutic strategies only marginally increases the survival time of metastatic patients.

3.2 Metastatic cascade

Metastasis formation was conventionally divided into six steps [4]. First: primary tumor growth, angiogenesis and invasion of surrounding tissue; second: tumor cell endothelium invasion (intravasation) third: survival in the blood circulation and emboli formation, fourth: extravasation of the tumor cell and interaction with organ specific microenvironment, sixth: metastatic colonization, tumor proliferation / dormancy in distinct organs (*Figure 1*). Each step in this cascade requires the acquisition of specific mutations allowing the cells to survive these biological barriers. From a clinical perspective, most of these steps occur before a cancer specialist has seen the patient.

Invasion, intravasation, survival in the circulation and extravasation are undetectable in today's routine clinical scenario.

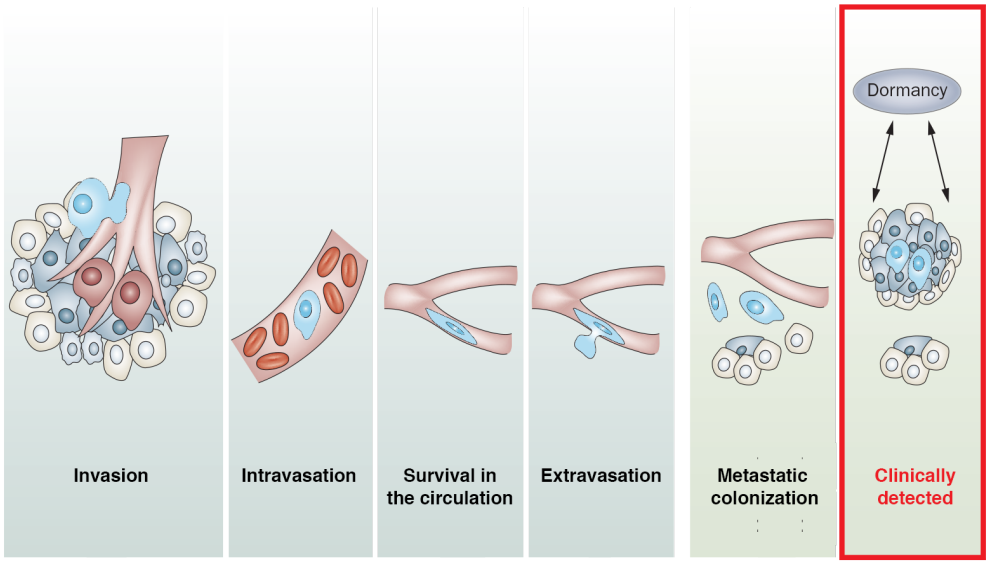

Figure 1: Metastatic tumor formation. *After successful angiogenesis, primary malignant neoplasms invade into the blood stream, from embolisms and arrest in distant micro capillary systems. Cancer cells adhere to the vascular wall and extravasate. In growth promoting microenvironments tumor cells receive positive input and proliferate. Finally metastases develop. Adapted and modified from [4]*

The current clinical understanding of intravasation is very limited. It remains elusive how frequently metastasis develop before adjuvant therapy of the primary tumor. In consequence, the here presented experiments are focused on tumor cell extravasation and metastatic colonization.

3.2.1 Primary tumor growth, angiogenesis and invasion

Primary tumors show massive proliferation and related high-energy consumption caused by the Warburg Effect [5]. This energy demand leads to hypoxia in the tumor area and expression of proangiogenic factors inducing the formation of new blood vessels [6]. These blood vessels supply the tumor with oxygen and nutrients and drain waste products [6]. Moreover, these blood vessels serve as the main route for intravasation of tumor cells because of their distinct morphology and functional disorder. The vascular system created by tumors is leaky, often dilated, tortuous and chaotic [7]. This phenotype of immature unorganized vessels that leak pericyte-endothelial contact has been shown to increase metastatic potential [8]. Hence, pericytes (capillary diameter regulating mural cells) have been proposed as gatekeepers to metastasis [9].

3.2.2 Intravasation of tumor cells

Endothelial intravasation is fostered by leaky blood vessels formed by the tumor. There are several gene mutations that allow cancer cells to invade the surrounding tissue. These mutations incorporate functions relevant for immune system evasion, epithelial-mesenchymal transition (EMT), bone marrow progenitor mobilization, cell motility promotion and extracellular matrix degradation [4]. EMT was hypothesized as a critical pro metastatic switch [10]. EMT is regulated by increased expression of Twist-related protein 1 (*TWIST1)*, snail family zinc finger 1 *(SNAIL1)* and snail family zinc finger 2 *(SNAIL2)*, three generally abundant transcription factors [11]. Hence, they are readily deregulated by common mutations in cancer cells. After intravasation tumor cells have to develop immune escape mutations in order to survive in the blood circulation.

3.2.3 Survival in the blood circulation and emboli formation

Circulating tumor cells post intravasation are encountered and bound to platelets. Inhibition of tumor cell platelet interactions has been shown to reduce hematogenous metastasis [12, 13]. Consequently, reconstitution of platelets restored the metastatic phenotype [14]. Additional studies in Protease-activated receptor 4 (*PAR-4)* and *fibrinogen* knockout mice demonstrated that activation of platelets significantly contributes to metastasis formation [12, 15]. Platelet – tumor cell protection mechanisms depend on coagulation factors. First, platelet - tumor cell adhesion is mediated by integrins (*αIIbβ3*), followed by thrombin activation and fibrinogen cleavage. Fibrin and fibrinogen induce tumor cell thrombus formation followed by arrest within the vasculature system [16-18]. Lysis of circulating tumor cells is insufficient, even though natural killer (NK) cells and leukocytes are found in close proximity of these thrombi [19]. The coagulated platelets probably inhibit direct tumor cell – NK cell contact and lysis (*Figure 2*).

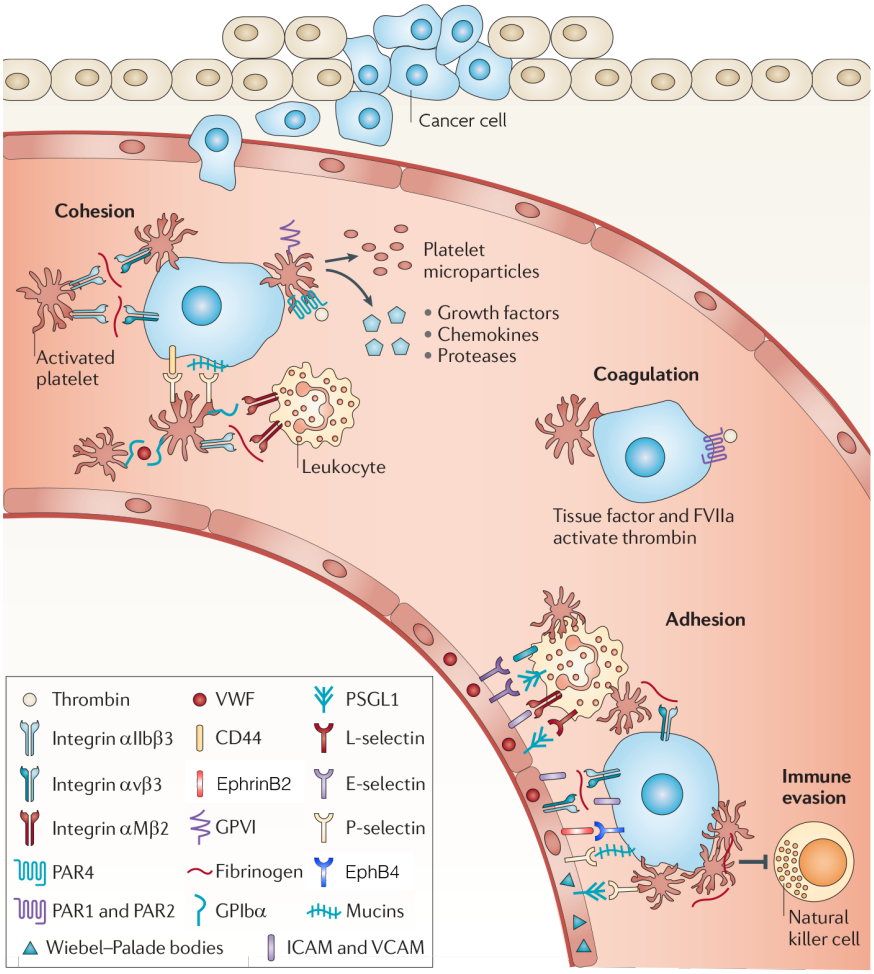

Figure 2: Metastatic tumor cell in blood circulation. *Tumor cells are confronted with different cell types after entering the endothelium. Generally the first cell type interacting with tumor are platelets. They get activated by cancer cells and thereby increase their adhesiveness to them. Simultaneously they release micro particles, which contain growth factors, chemokine's and proteases. These factors might contribute to tumor cell survival via positive paracrine stimulation. The activated platelets and their fibrinogen facilitate immune system evasion by protecting the circulating cancer cells from natural killer cells. Moreover, FVIIa and tissue factor activate thrombin to cleave PARs on tumor cells and platelets this further promotes invasion and metastasis. Adapted and modified from [20]*

However, tumor cell arrest in vascular structures is a rare event and difficult to observe in deep tissues *in-vivo*, unlike the long established concept of leukocyte rolling and extravasation. Metastatic tumor cell rolling has just recently been shown to occur *in-vivo* [21]. Lack of metastatic models limits *in-vivo*, real-time visualization of tumor cell – endothelial cell interaction [17, 18]. Therefore, current research strategies focus on metastatic dissemination approaches. Inhibition of endothelial cell – platelet interaction via P-selectin – PSGL-1 decreased metastatic dissemination and long-term metastasis formation [22, 23]. The ephrinB2 – EphB4 system has been shown to

mediate tumor cell – endothelial cell interaction, which might play a dominant role in mediating metastatic tumor cell dissemination. In this context, ephrinB2 – EphB4 interaction was shown to induce lung specific dissemination [24].

3.2.4 Extravasation of the tumor cell and interaction with organ specific microenvironment

Extravasation into the microenvironment of different organs can only be achieved by a subset of disseminated tumor cells as every organ provides a different microvascular system. Examples are described in *Figure 2*. Disseminated cancer cells to the brain face the blood brain barrier, a tight multilayer sandwich composed of multiple cell types. Cancer cells, which arrive in the lung, are confronted with endothelial cells surrounded by alveolar cells only. Finally, tumor cells in bone only face loosely attached sinusoids, which contain large pores for the exchange of hematopoietic cells. Individual tumor cell properties largely determine the extravasation target microvascular system [25].

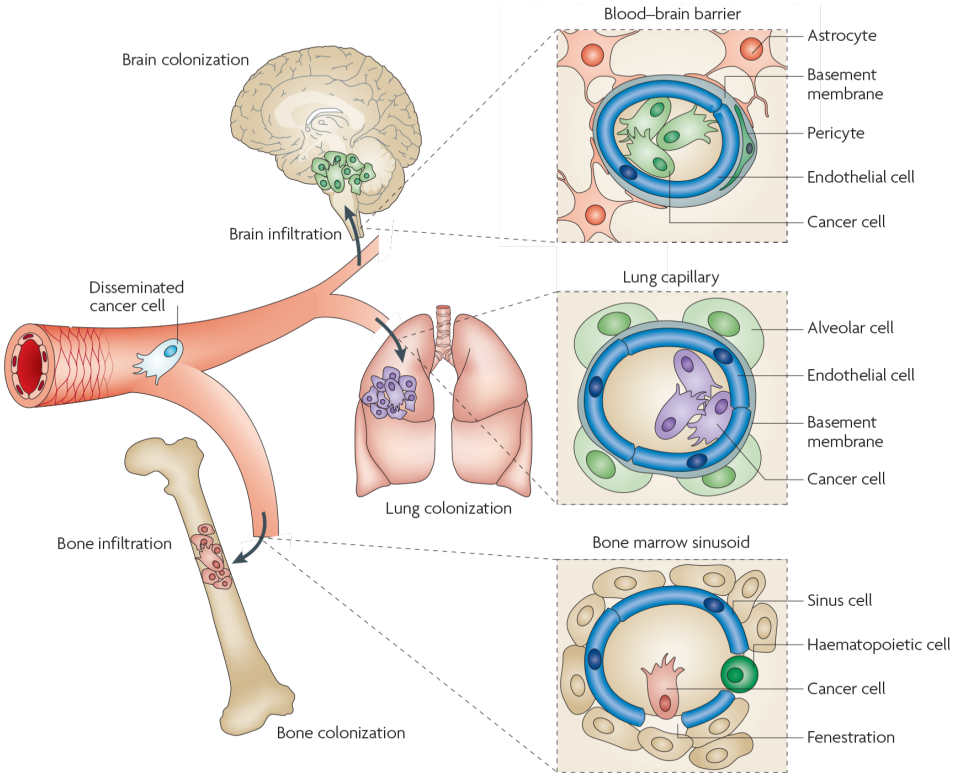

Figure 3: Dissemination of tumor cells to different endothelial environments. *There are extensive vascular anatomy differences between organs. Disseminating cancer cells are confronted with organ specific challenges regarding vascular adhesion and extravasation. For example: The brain is protect by the blood brain barrier which consists of a sandwich made by endothelial cells, basement*

membrane, pericyte, basement membrane and astrocyte end feet. In the lung, cancer cells have to overcome only endothelial cells and one basement membrane. In the bone, sinusoids form the blood bone barrier, keeping undifferentiated hematopoietic cells in the bone marrow. But, sinusoids are generally loose with large pores between endothelial cells. Adapted and modified from [25]

It was hypothesized that repeated injection of metastasized cells would lead to the selection of tumor cell subclones, which only metastasize to the organ of resection. Stackpole et al. failed to prove this hypothesis [26]. Multiple cycles of spontaneous metastasis increased general aggressiveness and unspecific metastasis formation of the tumor cell clones [26]. This findings strengthened Paget's 'seed and soil' hypothesis, which suggested an intrinsic preference of certain tumors to specific microenvironments of certain organs [27]. This preference persists even after multiple rounds of injection to a different organ [26]. However, extravasation was shown to occur in three different ways. First, clustered tumor cells and platelets form vascular thrombi, then tumor cells proliferate inside the vascular system until it collapses [28]. Second, pulmonary metastases adhere to the endothelium and post adhesion endothelial cells slowly migrate over the adhesive tumor cell [17]. Third, B16 melanoma adhere to skin microvessels and extravasate after maximum deformation of the nuclei (diameter < 1µm) [21]. Multiple tumor cells would perform this extravasation in a bead chain mode one after the other [21].

3.2.5 Tumor proliferation / dormancy in distinct organs

Once extravasated, the tumor cell receives organ specific inputs from the novel microenvironment [29]. Again, Paget's 'seed and soil' hypothesis holds true, which postulates only specific cancer cells survive in distinct microenvironments. Tumor formation is mostly dependent on the tumor cell paracrine signaling. In some cases tumor cells are present in distinct organs without establishing a tumor, which is referred to as oligometastasis or dormant metastasis [29, 30]. Tumor cell dormancy is hypothesized to have various reasons all involving paracrine signaling of tumor cells: Tumor cells fail to induce appropriate proangiogenic factors, tumor cell proliferation factors are absent in the target microenvironment, the tumor cell progeny fails to escape the immune system or the tumor cell needs to acquire extra mutations to proliferate [31-33].

Melanoma cells (B16) were shown to metastasize to spinal and femoral bone after intracardiac injection [34]. Besides the ability of B16 to induce osteolysis in an MMP

dependent manner, the inherent microenvironment is reprimed to facilitate bone digestion [35, 36]. The general concept of metastasis induced osteolysis involves the release of 4 different cytokines: parathyroid hormone-related protein (PTHrP), interleukin 6 (IL-6), interleukin 11 (IL-11) and tumor necrosis factor alpha (TNFα). These cytokines activate receptor activator of nuclear factor kappa-B ligand (RANKL) secretion of osteoblasts. RANKL promotes the differentiation of myeloid precursor cells into osteoclasts. Bone digestion by osteoclasts again releases cytokines (transforming growth factor beta (TGFβ), insulin-like growth factor 1 (IGF1) and bone morphogenetic proteins (BMPs)), which promote metastatic growth. This cascade accelerates metastasis formation in the bone (*Figure 4*).

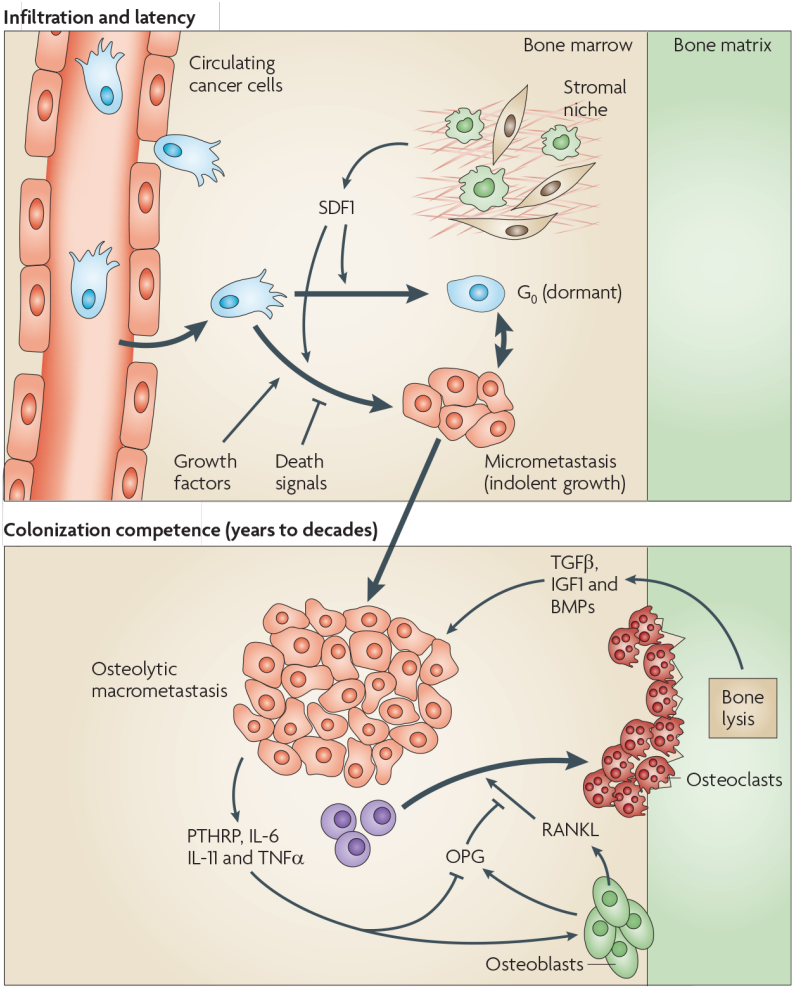

Figure 4 Successful infiltration of boney tissue is not a prerequisite for metastasis. *After the extravasation of circulating tumor cells into the bone marrow the cells are confronted with growth factors (example: stromal cell-derived factor 1; SDF1) and apoptosis signals. The balance of signals available and receptors expressed on tumor cells determine the fate (apoptosis, dormancy, proliferation to micro metastasis) of the cancer cell. In the case of micro metastasis formation and further proliferation to osteolytic macro metastasis, PTHrP, IL-6, IL-11 and TNFα need to be secreted by the*

tumor. These factors hinder osteoblast differentiation and induce RANKL secretion by osteoblast, which differentiates myeloid precursors into osteoclasts. During bone lysis multiple growth factors are secreted that promote tumor growth further (TGFβ, IGF1 and BMP's). Image adapted from [25]

3.3 Eph / ephrin receptor tyrosine kinases

The Eph receptor tyrosine kinase family is the largest subfamily of the total 58 receptor-tyrosine-kinases found in humans. They were discovered in erythropoietin producing hepatocellular (Eph) carcinoma cell lines and their ligands were described as Eph receptor family interacting proteins (ephrin) [37]. The ephrin ligands and the Eph receptors are both bound to the cell membrane [37]. In consequence, Eph receptor signaling only occurs after direct cell to cell interaction. Moreover, signaling is not limited to the Eph receptor (forward signaling), the ephrin ligand-expressing cell can also receive a signal upon binding (reverse signaling). Based on sequence homology and binding preference, two subclasses (ephrinA – EphA, ephrinB – EphB) were classified. The first subclass consists of six ephrinA (ephrinA1-6) ligands plus nine EphA (EphA1-8 and EphA10) receptors. The second subclass incorporates tree ephrinB (ephrinB1-3) ligands plus five EphB (EphB1-4 and EphB6) receptors (*Figure 5 B*). The ephrin ligands both contain a receptor-binding domain (RBD) but ephrinA ligands lack the internal PDZ domain (*Figure 5 A*). Thus, reverse signaling of ephrinA only occurs after binding of co-receptors. EphrinB ligands in contrast contain a transmembrane domain including a phosphorylation site and a PDZ domain, which allows the generation of reverse signaling in an independent manner. EphA and EphB receptor structures are very similar both contain a ligand binding domain, a transmembrane domain, the intracellular kinase, the SAM and PDZ motives.

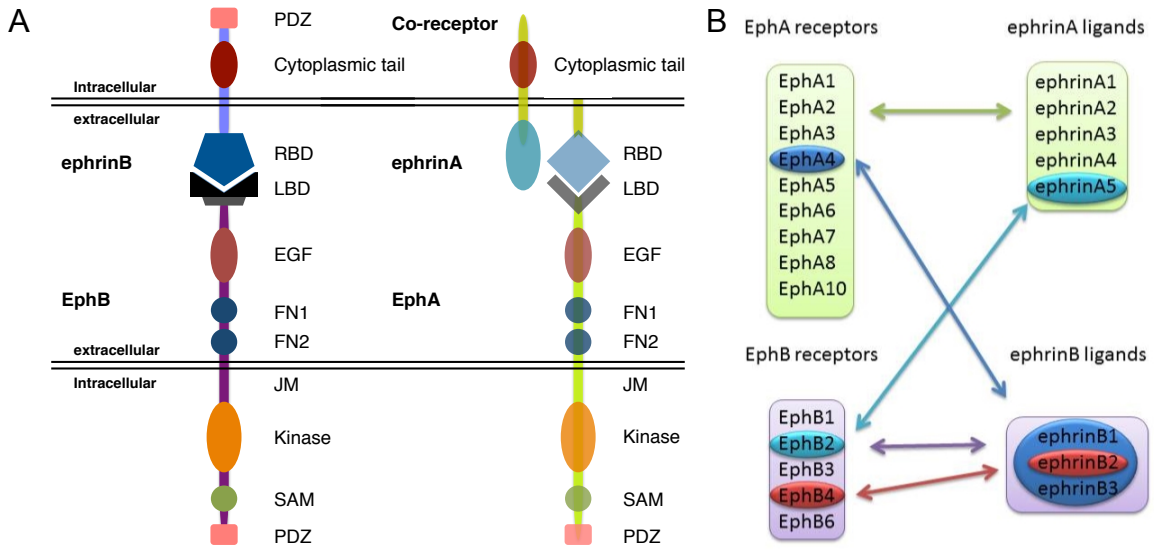

Figure 5 Ephrin – Eph receptor interactions. *A) EphrinB2 receptor binding domain (RBD) activation induces reverse signaling independently whereas ephrinA reverse signaling requires activation of RBD and co-receptor binding. Eph receptors contain: ligand binding domain (LBD), cysteine-rich region (Sushi / EGF), two fibronectin type-III repeats (FN 1,2), transmembrane domain (TM), Juxtamembrane domain (JM), the Kinase domain, the sterile α-motif (SAM) and the PDZ domain. B) EphB receptors generally bind ephrinB ligand. Exceptions are EphB2 binds to ephrinA5 (cyan arrow), All ephrinB ligand bind to EphA4 (blue arrow) and EphB4 only binds ephrinB2 (red arrow). Adapted form [38, 39]*

The downstream effects of Eph receptor mediated forward signaling may vary on the subsequently activated signaling pathway [37]. Proliferation is induced via the Phosphatidylinositol-4,5-bisphosphate 3-kinase (PI3K) pathway / Ras pathway. Migration is achieved via the Rho pathway. And adhesion can occur via the Abl pathway. Forward signaling of ephrinB leads to actin cytoskeleton remodeling in the short term via rous sarcoma oncogene (Src) and non-catalytic region of tyrosine kinase adaptor protein 2 (Nck2) activation [37]. For long-term changes PDZ domain signaling via protein tyrosine phosphatase BL (PTP-BL) is required [37].

3.4 EphrinB2 – EphB4 in the vascular system and angiogenesis

Wang et al., first described ephrinB2 as an arterial endothelial cell marker and EphB4 as a venous marker [40]. EphB4 and ephrinB2 classical knockout mouse models showed embryonic lethality (EphB4: E10.5, ephrinB2: E11.5) provoked by insufficient vasculogenesis [41, 42]. These results and the absence of lethality in EphB2 and EphA4 knockout mice imply ephrinB2 – EphB4 interaction is essential for vascular

morphogenesis [42]. Detailed development analysis of ephrinB2 – EphB4 showed involvement in cell migration via attraction and repulsion signaling [43, 44]. In neuronal development EphB expressing axons are repelled by ephrinB expressing tissue [43]. In angiogenesis EphB4 positive vessels only fuse with ephrinB2 negative vessels [44]. Functional analysis of this phenotype revealed that EphB4 kinase activation after binding to ephrinB2 positive cells caused Rac activation and internalization of EphB4 – ephrinB2 into the EphB4 positive cell leading to repulsion [45]. Similar to ephrinB2 – EphB4 studies, vascular endothelial growth factor A (VEGF) depletion and the depletion of its main receptor (VEGFR2) caused embryonic lethality by vascular deficits [46, 47]. Recently availability of PDZ domain specific mutant mice and inducible vascular specific knockout animals allowed combining both fields. It has been found that ephrinB2 overexpression causes increased endothelial cell sprouting similar to VEGF treatment [48]. Moreover, ephrinB2 builds a dimer with VEGFR2 and regulates its internalization, which is crucial for angiogenesis signaling (*Figure 6*) [49].

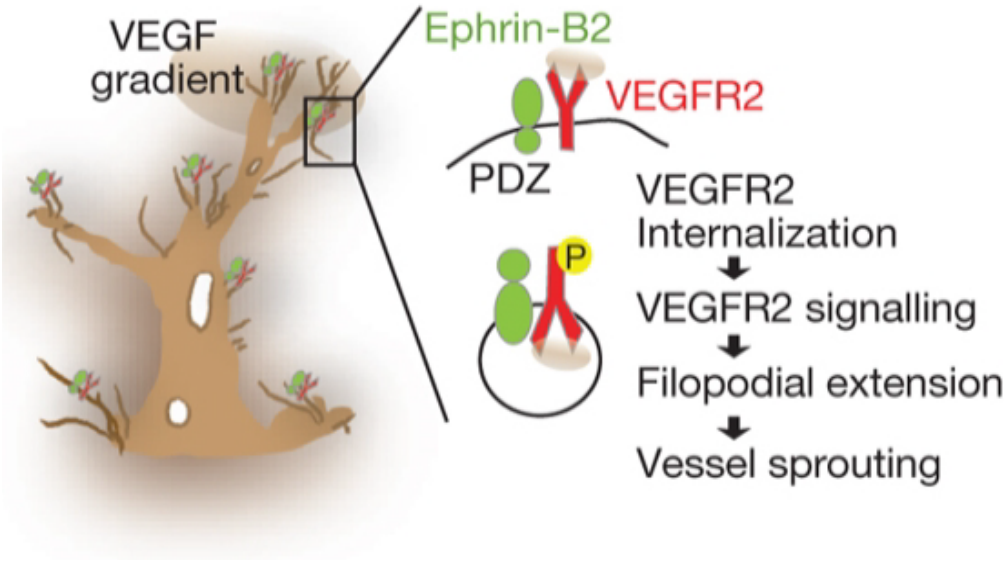

Figure 6 EphrinB2 – VEGFR2 signaling in angiogenesis. *Vascular endothelial growth factor receptor 2 (VEGFR2) and ephrinB2 are expressed in endothelial tip cells invading VEGF secreting tissue. After VEGF binding in tip cells, VEGFR2 gets phosphorylated and internalized with ephrinB2. This process regulates filopodial extension and follow-up vessel sprouting. Adapted from [49]*

EphrinB2 absence and lack of PDZ functionality inhibit VEGFR2 and VEGFR3 internalization and signaling. This resulted in significantly smaller glioma size and significantly reduced vessel density [49].

3.5 EphrinB2 – EphB4 interaction in tumor development

Controversial roles for ephrinB2 – EphB4 signaling in tumors have been described. It has to be mentioned that expression of EphB4 does not necessarily correlate with increased activation of EphB4. In EphB4 overexpressing breast cancer, receptor phosphorylation was reduced in absence of ephrinB2 [50]. EphB4 activation by ephrinB2 was shown to reduce tumor proliferation and invasion [50]. On the other hand EphB4 activation also increased migration and proliferation [51].

3.5.1 Tumor suppressive roles of ephrinB2 – EphB4 interaction

EphB4 activates tumor suppressive pathways after ephrinB2 binding *in-vivo*. MCF-7 cells treated with soluble ephrinB2 (ephrinB2-FC) showed reduced tumor size caused by the activation of the Abl proto-oncogene c-Crk (Crk) pathway [50]. The activation of this pathway in MDA-MB-435c cells constrained their proliferative and invasive phenotype. Phosphorylation of Crk at the Tyr221 residue was found to provoke this change in phenotype. After phosphorylation of Crk by Abl / Arg, p-Crk is unable to function as an adapter protein [52]. Suppression of Crk phosphorylation at Tyr221 via Abl mutation was shown to promote tumorigenesis [50]. Similarly active mutations of Crk Tyr221 also induce pro-migratory and survival signals [50]. *In-vivo* the overexpression of EphB4 in B16 melanoma was shown to reduce subcutaneous tumor size by a change in vascular morphogenesis [53]. This reduction was linked to the absence of blood vessels with arterial phenotype in B16/EphB4 tumors. This effect was further investigated *in-vitro*. Direct contact of B16/EphB4 with ephrinB2 positive endothelial cells *in-vitro* induced endothelial cell apoptosis. This effect could be blocked with soluble EphB4 (EphB4-FC) indicating a mechanism distinct from ephrinB2 forward signaling.

3.5.2 Tumor promoting roles of ephrinB2 – EphB4 interaction

Different cancer cells and endothelial cells were found to activate protein kinase B (PKB) or Src pathways after overexpression of EphB4 [54]. PI3K/PKB activation results in increased proliferation and survival [54]. Overexpression in B16 melanoma cells increased migration *in-vitro* [53]. EphB4 directly activates disintegrin and metalloproteinase domain-containing protein 10 (ADAM10). ADAM10 cleaves E-cadherin, thus impairs cellular adhesion and polarization [55]. Research on the angiogenesis mechanism of EphB4 showed downstream activation of PI3K / PKB disturbed the

extracellular matrix (ECM) by upregulation of MMP2 and MMP9 [56]. Moreover, EphB4 activation in melanoma lead to increased migration through activation of RhoA [57]. This migration was induced via EphB4 kinase phosphorylation [57]. Mutation of EphB4 kinase activity, mutation of the phosphorylation site, or expression of dominant negative RhoA, abolished this phenotype [57].

3.5.3 Role of ephrinB2 – EphB4 in metastasis

EphB4 has been shown to foster spontaneous metastasis in combination with the human epidermal growth factor receptor 2 (Her2) homologue NeuT [58]. Transgenic NeuT mice develop non-malignant tumors within 6 month [58]. NeuT mice crossbred to an EphB4 overexpressing model, changed this phenotype towards spontaneous lung metastasis never observed in single NeuT or EphB4 mice [58]. Further activation of EphB4 after overexpression of dominant negative ephrinB2 (reverse signaling only) increased primary tumor invasion and metastasis formation [59]. In a recent study, EphB4 expression in human A375 melanoma cells induced lung specific cancer cell dissemination [24].

3.6 Hypotheses

In this Ph.D thesis research was conducted to evaluate the following hypotheses:

1) Metastatic tumor cell dissemination is influenced by biological mechanisms and does not represent a sole stochastic (mechanistic) phenomenon.
2) Tumor cell-endothelial cell interactions mediated by ephrinB2 – EphB4 interaction represent a crucial step in metastasis formation influencing organ specific metastatic cell dissemination and metastasis development.

4 Material and Methods

4.1 Materials

4.1.1 Vectors

Table 1 Vectors

Name	Resistance	Control restriction sides	Insert size [kb]	Vector size [kb]
V048[1]	Ampicillin	XhoI, BamHI	-	9.9
V094[1]	Ampicillin	XhoI, Bsu361	-	10.2
V137[1]	Ampicillin	XhoI, BamHI	-	8.1
V197[1]	Ampicillin	XhoI, BamHI	3.137	11.6
V198[1]	Ampicillin	XhoI, BamHI	3.137	12.3
psPAX2	Ampicillin	EcoRI	4.1	6.6
pMD2.G	Ampicillin	NotI, HindIII	2.8	3.0

[1]Vector-maps are available at Prof. Harms C, Experimental Neurology Charité Berlin

4.1.2 Primer

The following primers were used from mouse genotyping and Real-Time PCR analysis.

Table 2 Primers

Name	5’ to 3’ Sequence	Annealing Temp. [°C]
3’ ephrinB2 lox 3 S	CTTCAGCAATATACACAGGATG	62
5’ ephrinB2 lox 3 AS	TGCTTGATTGAAACGAAGCCCGA	62
5’ CreERT^2 S	ATCCGAAAAGAAAACGTTGA	56
5’ CreERT^2 AS	ATCCAGGTTACGGATATAGT	56
3’ ANG1 S	GGATTGAGCTGATGGACTGG	58
5’ ANG1 AS	ACCACCAACCTCCTGTTAGC	58
3’ ANG2 S	GATCTTGTCTTGGCCTCAGC	58

3’ ANG2 AS	GCACTGAGTCGTCGTAGTCG	58
5’ ephrinB2 S	AATCACGGTCCAACAAGACG	58
3’ ephrinB2 AS	GTCTCCTGCGGTACTTGAGC	58
5’ EphB4 S	GAGCTATGTCCACCGAGACC	58
3’ EphB4 AS	GAACTTCCTGAAGGCAATGG	58
3’ Gapdh S	GGCCTTCCGTGTTCCTACC	58
5’ Gapdh AS	AACCTGGTCCTCAGTGTAGCC	58
3’ Notch-1 S	GCTTGTGGTAGCAAGGAAGC	58
5’ Notch-1 AS	CACATTCAAGTGGCTGATGC	58
3’ VEGF-A S	GAAGAAGAGGCCTGGTAATGG	58
5’ VEGF-A AS	AAGCCACTCACACACACAGC	58

4.1.3 Reagents and enzymes

The following reagents and enzymes were used (Table 3).

Table 3: Reagents and enzymes used

Name	Supplier
Ketavet (Ketamine)	Pfizer (#B2502-04; New York City , NY, USA)
Rompun (Xylazine)	Bayer (#KP07TPA, Leverkusen, DE)
Tramal (Tramadol)	Grunenthal (#PZN-7803245, Aachen, DE)
Trizol reagent	Life technologies (#15596-026)
Tamoxifen	Cayman (#CAS 10540-29-1, Ann Arbor, MI, USA)
D-Luciferin sodium salt	Santa Cruz (#Sc-207479, Santa Cruz, CA, USA)
NVP-BHG712	Sigma Aldrich (#SML0333, St. Louis, MO, USA)
IGG control antibody	Jackson ImmunoResearch (#015-000-008, West Grove, PA, USA)
Recombinant Mouse EphB4 Fc Chimera, CF	R&D (#446-B4-200, Minneapolis,

	MN, USA)
PEG 300	Sigma Aldrich (#90878)

4.1.4 Preparation kits

PureLink® RNA Mini Kit (Life technologies, # 12183018A)

QuantiTect ®Reverse Transcription Kit (Qiagen, Venlo, NL, #205310)

PrimeScript™ RT-PCR Kit (Takara, Otsu, JP, #RR014A)

TOPO TA Cloning Kit (Invitrogen, SKU# KNM4600-01)

BCA Protein Assay Kit (Pierce, #PI-23227)

ECL Western Blotting Substrate (Pierce, # 32106)

Bright-Glo™ Luciferase Assay System (Promega, #E2610)

4.1.5 Cell lines

HEK 293 TN (*Homo sapiens* (human), embryonic kidney) ATCC Nr: CRL-11268

PhoenixECO (*Homo sapiens* (human), embryonic kidney) ATCC Nr: CRL-3214

PhoenixECO (*Homo sapiens* (human), embryonic kidney) pLXSN-empty [60]

PhoenixECO (*Homo sapiens* (human), embryonic kidney) pLXSN-EphB4-wt [60]

B16-F1 (*Mus musculus* (mouse), melanoma) ATCC Nr: CRL-6323

4.1.6 Microspheres

Ø 7.3µm ~4.6 x 10^7 beads/ml (Polyscience Europe, Heidelberg, DE, #FS06F/11107)

Ø 15.45µm ~4.9 x 10^6 beads/ml (Polyscience Europe, #FS06F/ FS07F/11034)

4.1.7 Antibodies

The following antibodies were used for western blot and immunofluorescence staining.

Table 4: Antibodies

Name	Article	Distributer	Immunoblot dilution	immunofluorescence dilution and purpose
Anti-actin-HRP	A3854	Sigma Aldrich	1:10000	Western blot loading control
Anti-CD31	550274	BD-Pharmingen, New Jersey, USA	-	1:50 Endothelial marker
Anti-Desmin	ab15200	Abcam, Cambridge, UK	-	1:100 Pericyte marker
Anti-EphB4	sc-5536	Santa-Cruz	1:500	1:100
Anti-ephrinB2	GT15026	Neuromics, Edlna, USA	1:500	1:50

4.1.8 Buffers and media

Table 5 Cell culture media

DMEM, 4.5 g/l D-Glucose, L-Glutamin, Pyruvate (Gibco, 31965)	10%	Fetal calf serum (FCS)
Cell Freezing Media	90% 10% (DMSO)	FCS Dimethoxysulfoxide
Luciferase lysis buffer	0.1 M 0.1% 2mM	TrisHCl Triton X – 100 EDTA

4.1.9 Equipment

Table 6 Equipment

Fluorescence microscope	Zeiss Axiovision2 (Zeiss, Jena, DE)
PCR Cycler	VWRI732-1200 (VWR, Radnor, PA, USA)
Western blot Gel doc imaging system	Syngene Bio Imaging GeneGnome (Syngene, Cambridge, UK)
RT-PCR	Applied Biosystems 7900HT (Invitrogen, Carsbad, CA, UK)
Plate-reader	Tecan Infinite 200M (Tecan, Männedorf, CH)
Cryostat	Microm HM 560 (Thermo Fisher Scientific)
Tissue homogenizator	Xiril Dispomix (Miltenyi biotec, Bergisch Gladbach, DE) Mortar and pistil
Operation microscope	Carl Zeiss OPMI CS-NC Leica WILD M650 (Leica, Wetzlar, DE)
MRI	Pharmascan 70／16AS (Brucker, Billerica, MA USA)
In-vivo luminometer	Lumina II (Caliper LS, Hopkinton, MA, USA)

4.1.10 Software

Table 7 Software

Amira 5.2	FEI Visualization (San Diego, USA)
GraphPad Prism	GraphPad (San Diego, USA)
Office 2011 Mac	Microsoft (Redmond, USA)
ImageJ	NIH (Maryland, USA)
Axiovision 3	Zeiss
CatWalk XT 8.0	Noldus (Wageningen, NE)
CellProfiler 2.1	Broad Institute (Boston, USA)

4.2 General molecular biology methods

4.2.1 RNA Isolation

Cells were washed with cold PBS and RNA was extracted according to manufacturers protocol (Ambion / Life technologies).

Mice were sacrificed and primary tumors were dissected and transferred to Trizol. Tissue was homogenized using program 3 on the Dispomix. RNA was processed according to manufacturers guidelines (Life technologies).

4.2.2 cDNA generation

RNA concentration was determined with the Tecan M200 spectrometer. RNA (1µg) was reverse transcribed to cDNA according to protocol (Qiagen).

4.2.3 qPCR

Real time PCR was performed with the 7900HT equipment (Applied Biosystems / Life technologies). Master mix and primers were used according to manufacturers instructions (Takara). Primer sequences are listed in Table 2 Primers. PCR reaction was carried out for 40 cycles with annealing temperature of 58°C. GAPDH served as internal standard.

4.2.4 Heat shock transformation of *escherichia coli*

Competent *escherichia coli* (*E. coli*) were thawed on ice for 10 min and subsequently substituted with 100 ng of plasmid DNA, mixed gently and incubated on ice for 5 to 10 minutes. The *E. coli* was heat shocked for 30 sec (90 sec for DH5α) at 42 °C. The transformed bacteria were quickly put back on ice and 200 µl of room temperature (RT) SOC medium was added. The E. coli were pre-incubated for 1 h at 37 °C with 300 rpm's in the Eppendorf tube shaker. The incubated *E. coli* were centrifuged for 1 min at 13'000 g. 100 µl of the SOC medium was added and the pellet was re-suspended. The suspension was plated on an ampicillin or a kanamycin agar plate and cultivated overnight at 37 °C.

4.2.5 Plasmid isolation

For small scale preparation single colonies of the overnight of cultured agar plates were picked and transferred to 3 ml LB medium consisting 50 µg/ml ampicillin or kanamycin. *E. coli* was cultivated for 16 h at 37 °C with a shaking rate of 220 rpm. Frozen glycerol stock was made by 200 µl of the culture to 200 µl glycerin freezing media was added and frozen at -80 °C. Plasmids were isolated with the QIAprep Spin Miniprep Kit (Qiagen), following the instructions of the manufacturer. DNA concentration was measured visually by comparing the ladder (Bioline) fluorescence with

the probe or spectrometrically with the Infinite® 200 PRO (Tecan). The probes were sent to LGC genomics (Berlin, DE) for sequencing.

4.2.6 Genomic DNA isolation

For genetic screening ear biopsies were taken. Basic lysis solution [50 mM NaOH / 0.2 mM EDTA; pH 12.25] was added to each biopsy (100 µl), boiled for 1 h 30 min at 95°C, in PCR cycler. Post incubation biopsies were cooled on ice and neutralized with 100 µl 40 mM TrisHCl pH 4.9. The probes are stable at 4°C for up to 1 year.

4.2.7 Mouse biopsy genotyping

GoTaq GoGreen polymerase master mix (Promega) was used to genotype the animals.

Table 8: Genotyping PCR master mix

Reagent	Concentration	Volume
Tail lyses	Tail lyses direct	1 µl
5’ Primer	10 µM	0.5 µl
3’ Primer	10 µM	0.5 µl
GoTaq GoGreen Master mix	2 x	5.5 µl
Water	Millipore II	3.5 µl
Total		11 µl

ephrinB2 lox and CreERT^2 genotyping PCR has been described previously [61, 62]

4.3 Lentiviral reporter vector cloning

The V048 pFUGW lintiviral transfer plasmid was digested with XhoI and BamHI, the 8552 bp vector backbone was isolated from agarose gel (addgene plasmid 14883, provided by Dr. David Baltimore [63]). The 3137 bp firefly luciferase-2a-eGFP-2a-puromycin insert was isolated from V137 (pcDNA5-FR-FF-EGFP kindly provided by Prof. Mrowka, Jena) cut with XhoI and BamHI. Ligation of the backbone resulted in V197, the ligation product was transformed into DH5α *E.coli* and grown over night at 37°C under ampicillin selection. The Woodchuck hepatitis virus post-transcription regulatory element (WPRE) is crucial for the enhancement of viral packaging, and thus increases the viral titter in the medium. The WPRE fragment (726 bp) was isolated from V094 with Bsu361 and XhoI (addgene plasmid 27232 [64, 65]). V197 was

linearized with Bsu361 and XhoI. The WPRE fragment was ligated with the linearized V197 and coded V198. The resulting lentiviral infection vector was transformed into DH5α *E. coli,* grown on ampicillin agar O/N at 37°C, single colonies were picked and grown in LB medium, control restriction was performed and maxi preparation of one positive clone was performed according to manufacturers instructions (Invitrogen). The Vector was sequenced for mutations. One null mutation was identified in the puromycin resistance gene.

4.4 Biochemical methods

4.4.1 Isolation of proteins

Cells were seeded in a 6 well plate for 2 days then lysed with 200 µl RIPA buffer per well, on ice. The cells were scraped and lysate was transferred into a tube. The lysate was probe sonicated 3 times for 1 sec at 100%. The tube was incubated on ice for 10 min and centrifuged at 10000g at 4°C for 10 min. Protein concentration of the supernatant was measured using BCA standards according to the manufacturers protocol (Thermo Fisher). The supernatant (protein fraction) was stored at -80 °C.

4.4.2 SDS Page

The protein was thawed on ice and 4x Invitrogen denaturation buffer (including 100mM DDT) was added to the sample. The mixture was denatured at 80°C, 5 min. Electrophoresis was carried out whit a 6% Tris-Glycin SDS stack gel and 8% SDS running gel generated according to the manuals instructions (Bio Rad). Sample volumes from 10 - 20 µl were loaded to the gel depending on the pocket size and 5 µl of prestaind protein marker served as control. Stacking was performed for 5 min at 80V separation was performed for 70 min at 140V.

4.4.3 Western Blot preparation

The PVDF acceptor membrane (Pore size exact), SDS-PAGE-Gel and Whatman papers were soaked in 1x western transfer buffer. The transfer sandwich was assembled: Anode, fiber pad, filter paper, gel, membrane, filter paper, fiber pad, cathode. Two transfers were utilized, a fast wet transfer: 1h, 4°C, 1 mA or a slow wet transfer: overnight, 4°C, 0,3 mA. The transfer was controlled with Pierce MemCode Reversible

Protein Stain Kit following the supplier's manual. Incubating in 5 ml in 1% Casein / PBS for 1h, RT, blocked unspecific bindings.

4.4.4 Immuno-incubation

The primary antibody was diluted in 3 ml 1% Casein / PBS and PVDF membranes were incubated for 1h at RT or over night at 4°C on in a roller tube and washed 3x with PBS-Tween (dilution described in Table 4: Antibodies). Incubation with the secondary antibody was in 8 ml 1% Casein / PBS on a shaker for 1h at RT and membranes were washed 3x with PBS-Tween-20.

4.4.5 Enhanced chemiluminescence detection (ECL)

ECL Reagent was freshly prepared (Pierce). The membrane was covered with the solution and the reaction was detected in the Western blot Gel doc imaging system with 1 min to 5 min exposure time.

4.4.6 *In-vitro* bioluminescence

Infected B16-luc cells were plated with 500 cells / cm^2 to 96 well plates. One day after plating, the cells were lysed and measured for 3s with Bright-Glo luciferase assay kit (Promega).

Standard curves for cell dissemination and metastatic cell number were generated as follows: Cells were counted with Casy Model TT (Roche) cell counter and were diluted to 100000, 50000, 25000, 12500, 6250, 3125 and 1562.5 per 96 well. The cells were lysed with 30 µl luciferase lysis buffer, 60 µl of Bright-Glo luciferase substrate was added and luminescence signal was immediately measured during 3 sec as described by the manufacturer (Promega).

4.4.7 *In-vitro* microsphere excitation

Standard curves for micro beads dissemination were generated as follows: GFP microspheres were diluted to 100'000 beads / 100 µl and sub sequential standard curves were generated with the following numbers (100000, 50000, 25000, 12500, 6250, 3125, 1562, 781, 391, 195, 98, 49, 24, 12). For measurement, beads were excited at 485 nm and 530 nm emissions were measured.

4.5 Cell culture

4.5.1 Freezing and thawing of cells

For freezing, approximately 80% confluent cells were washed with PBS and trypsinized. Trypsin reaction was stopped after 4 minutes with Glutamax medium containing FCS. The cells were centrifuged for 4 min at 900 x g. The pellet was resuspended in 1.5 ml Medium and aliquoted into 0.5 ml cryo tubes. 0.5 ml 2 x cell freezing medium was added. The cells were frozen with an interval of – 1 °C/min in a freezing block to -80 °C overnight and stored in liquid nitrogen. The cells were thawed in 37°C water bath. 1 ml medium was added and plated on a T25 flask (BD Bioscience) with additional an additional 5 ml medium.

4.5.2 Metastatic B16-luc (mB16-luc) generation

The B16-luc cells were injected in a separate wild-type C57Bl6/J mouse as described in paragraph 4.6.3. After the occurrence of a neurological deficit, the animal was sacrificed and the identified spinal segment was microsurgically explanted. The tumor was dissociated with scalpels under sterile condition and trypsinised at 37°C for 10 min. Trypsin reaction was stopped and centrifuged as described in paragraph 4.5.1. The cell pellet was re-suspended and routinely maintained at 37°C with 5% CO_2 in DMEM supplemented with 10% FCS, 50 units / ml penicillin, 50 µg/ml streptomycin and 5µg / ml puromycin. The cells were frozen as described in paragraph 4.5.1. Metastatic B16-luc cells were used only until passage 8 past primary explantation.

4.5.3 Calcium phosphate transfection

Lentiviral particles were produced in HEK293TN cells using the 3rd generation infection system described previously [65]. In brief, HEK293TN were plated on T175 Falcon flasks covered by 25 ml medium. The 3rd generation lentiviral vector master mix was prepared in a 15 ml Falcon as followed: 20µg of V198 was mixed with the lentiviral packaging plasmids psPAX2 (12.5µg, addgene plasmid 12260) and pMD2.G (7.5µg, addgene plasmid: 12259, both provided by Dr. Didier Trono). 155 µl of 2 M Calcium solution was added. The final volume of 1250 µl was adjusted with distilled water. 1250µl of 2x HBS solution was added drop wise to the vortexing master mix. The resulting mixture was incubated at RT for 20 min. HEK293 culture media was

renewed and transfection mixture was added slowly. Two days post transfection culture medium was exchanged.

4.5.4 Lenti / Retroviral isolation

Retroviral particles were produced in PhoenixECO pLXSN or pLXSN-mEphB4-wt cells. Retroviral vectors and the generation of virus-producing PhoenixECO cells has been described previously [60]. Lentiviral paricles were produced as described in paragraph 4.5.3. Supernatant media containing viral particles was collected every day for 3 days and stored at 4°C. Supernatants were centrifuged at 4°C, 1790g for 15 min. Cell debris free supernatant was filter sterilized (45µm) into a new 50 ml Falcon tube (similar supernatants were pooled). Viral particles were incubated with PEG-it (BioCat, Heidelberg, Germany) for 2 days at 4°C on end-to-end shaker. PEG bound viral particles was pelleted at 4°C, 3000 g for 20 min and the supernatant was discarded. The viral particle pellet were concentrated 1:100 in PBS and stored at -80°C.

4.5.5 Lenti / Retroviral infection of B16 melanoma cell lines

The cells were plated on 6 well plates with a cell density of 5 x 10^4 cells per cm^2 and infected the following day. The culture medium was renewed and 2, 4, 8 µl of concentrated Virus were thawed and added to individual 6 wells. 2 Days post infection the medium was exchanged with medium containing viral resistance selection compound (puromycin 5 µg/ml, G418 1000 µg/ml). Selection medium was exchanged every day. Selection was kept in place until non-infected cells were killed and infected wells attained an 80% confluence (usually 2 weeks).

4.5.6 MTT-Viability assay

MTT assay has been described previously [66]. Brief, cells were plated to 96 wells in different densities (2500, 5000, 10000 cells / well). After 24 h medium was changed and MTT reagent was added to the medium. The cells were incubated with MTT for 4 h. Supernatant was gently discharged and cells were lysed in 100µl isopropanol / DMSO (1:1). A Tecan 200M spectrometer was used to measure absorbance at 560 nm. Correction for protein precipitate interference was with a 630 nm reading reference.

4.5.7 Cell migration

Scratch assay was performed to measure migration [67]. Cells were seeded with 200'000 cells / 6 well and scratch was performed 12 h post seeding with a 2 ml pipet tip (Falcon, # 13-675-16). Pictures of the same area were taken after 24 and 48 h. Cell coverage was measured in % of total area and migration speed was calculated according to following formula:

$$\frac{cells(A)^{24h}[\%] - cells(A)^{0h}[\%]}{100\% \times 24h} \times ROI(w)[\mu m]$$

$$\frac{cells(A)^{48h}[\%] - cells(A)^{0h}[\%]}{100\% \times 48h} \times ROI(w)[\mu m]$$

Equation 1 Cell migration calculation. *Calculations for time point 24 hours and 48 hours post scratch. Region of interest (ROI) describes image taken.*

Analysis was performed automatically using CellProfiler 2.1 [68].

4.6 *In-vivo* spinal metastasis generation

4.6.1 Animals

Animal experiments were conducted in accordance with German animal care guidelines. Experiments were approved by LaGeSo (Landesamt für Gesundheit und Soziales Berlin; G0260/12 Nov. 26, 2012). Adult endothelial cell specific inducible ephrinB2 knockout *efnb2*$^{lox/lox}$ x *CDH5*-(Pac)-CreERT^2 animals (iΔ*efnb2*) and *efnb2*$^{lox/lox}$ control mice were used for the study [61, 69]. The mice were maintained at 22°C room with reverse 12-hour light/dark cycle. Endothelial specific ephrinB2 knockout was induced by intraperitoneal (i.p.) injections of tamoxifen (according to Jaxon laboratory guidelines). Tamoxifen inducible vascular specific ephrinB2 knockout mice (iΔ*efnb2*) and controls (*efnb2*$^{lox/lox}$, littermates not carrying the *CDH5*-(Pac)-CreERT^2 allele) were injected with 100 µl tamoxifen / corn oil solution (20mg/ml) for 5 days. After 9 additional days the animals were introduced into the experiments.

4.6.2 Workflow

Animals used for dissemination experiments:

Dissemination of cells and microbeads was measured 3 hours post injection. Therapy experiment workflow is shown in *Figure 7* Animals were treated twice with 50 mg / kg i.p. of the small molecule inhibitor NVP-BHG712 dissolved in PEG 300 or vehicle (PEG 300): 24 hours and 1 hour before cell injection. The EphB4-FC 20 µg antibodies were administrated i.p. one hour previous cell injection. Control animals received 10 µg IGG control antibody as described previously [24].

Table 9: Dissemination experiments animal list

Mouse strain	Experiment	Number
efnb2$^{lox/lox}$	7 µm GFP microbeads	5
efnb2$^{lox/lox}$	16 µm GFP microbeads	5
efnb2$^{lox/lox}$	IGG / PEG control	5
efnb2$^{lox/lox}$	NVP-BHG712	5
efnb2$^{lox/lox}$	EphB4-FC	5
iΔ*efnb2*	PEG control	5
efnb2$^{lox/lox}$	mB16-luc	3
efnb2$^{lox/lox}$	B16-luc-pLXSN	5
efnb2$^{lox/lox}$	B16-luc-EphB4	5

Graphical representation of the dissemination experiments is visualized in *Figure 7*

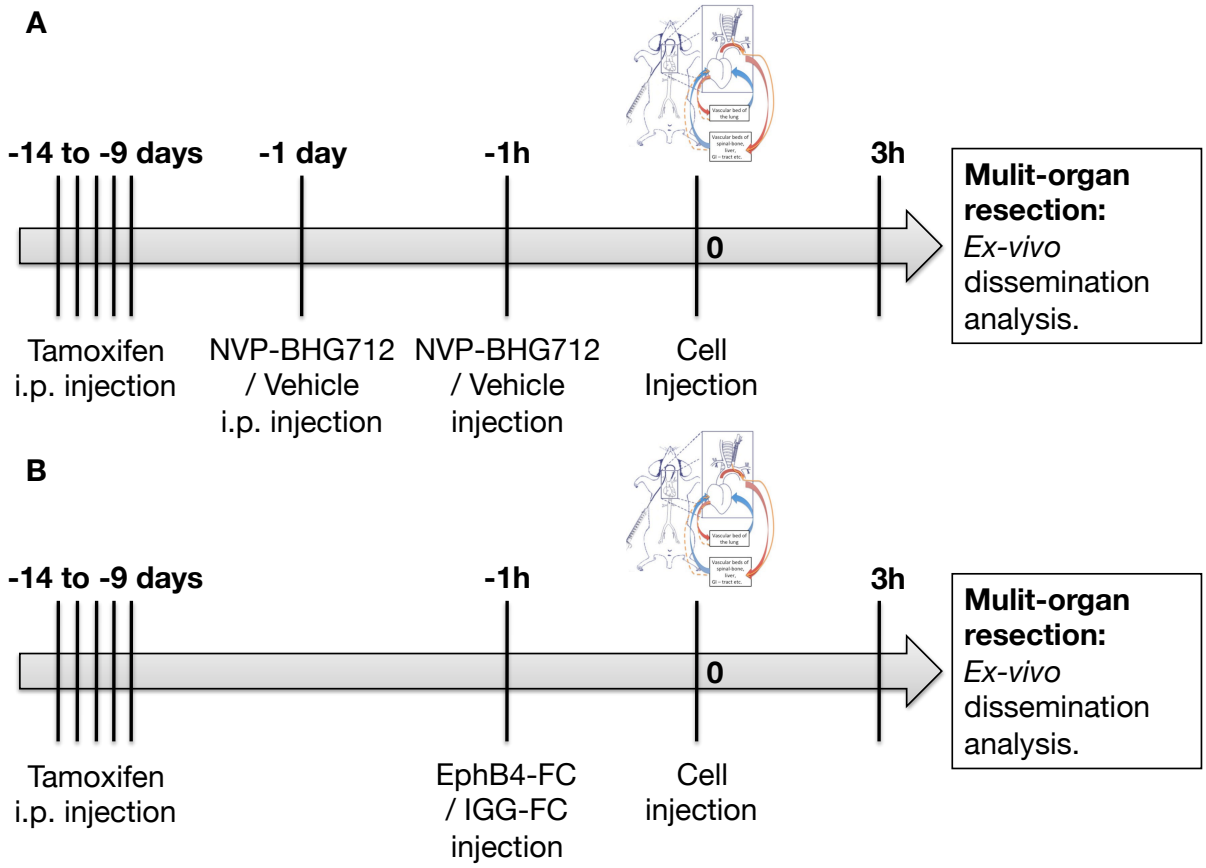

Figure 7 Experimental workflow for cell dissemination experiments. *Mice were i.p. injected with tamoxifen 14 days prior to cell injection. A) The microbeads (7 & 16µm), the iΔefnb2, the mB16-luc, B16-luc-pLXSN and B16-luc-EphB4, NVP-BHG712 and the IGG / PEG control groups received two injections (24h and 1h) before cell injection. B) The EphB4-FC and IGG / PEG control group received one injection 1h before cell injection. Cell dissemination was allowed for 3 h before animals were sacrificed.*

Animals used for long-term experiments:

Long-term experiments were carried out over 25 days or until the occurrence of a neurological deficit. *In-vivo* bioluminescence was measured every 5 days to assess tumor progression. MR imaging was performed at day 15 and day 25 and / or at the day of neurological deficit.

Table 10: Long-term experiments animal list

Mouse strain	Experiment	Number
efnb2$^{lox/lox}$	B16-luc	7 (5 used for MRI)
efnb2$^{lox/lox}$	mB16-luc	5

iΔ*efnb2*	B16-luc	5
efnb2$^{lox/lox}$	B16-luc-pLXSN	5
efnb2$^{lox/lox}$	B16-luc-EphB4	5

Graphical representation of long-term spinal metastasis experiments is visualized in *Figure 8*.

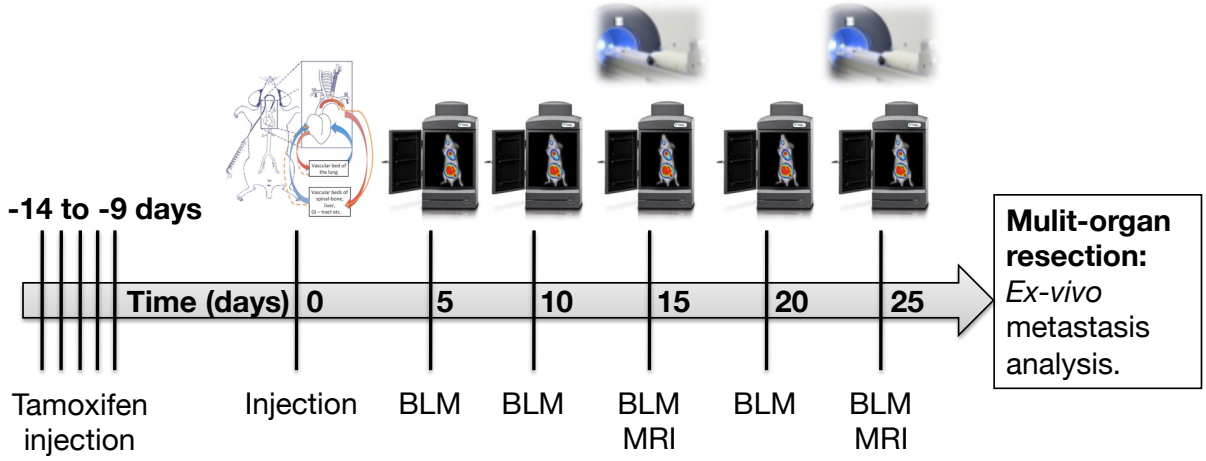

Figure 8 Experimental protocol foe spinal metastasis experiments. *Mice were i.p. injected with tamoxifen 14 days prior to cell injection. In-vivo bioluminescence (BLM) was performed 5, 10, 15, 20 and 25 days post injection to determine metastasis location and progression. Magnetic resonance imaging (MRI) was performed at day 15, 25 and / or at day of neurological deficit.*

4.6.3 Hematogenous spinal metastases model

Adult mice (21 – 32g body weigh (BW)) were anesthetized deeply (100µl anesthesia mix / 10g BW). Anesthesia was verified by foot paw pinching reflex control. The catheter (0.8 mm Ø and 5 cm length) was placed on a 30G injection needle and filled with 0.9% NaCl solution. A longitude skin incision along the trachea was performed. The thymus was divided to expose the left carotid artery. The carotid artery was carefully separated from the vagus nerve and permanently / temporarily ligated distally and proximally of the aortic arch respectively. Drawing shown in *Figure 9*. The artery was opened and the catheter was retrogradely inserted and fixed. The proximal ligature was opened and 100 µl of DMEM / cell suspension (1 x 10^5 cells) was injected followed by 100 µl 0.9% NaCl. The proximal ligature was closed permanently and the catheter was removed. The skin was closed and sutured. Neurological deficit occurrence was recorded in days. Unlike intracardiac injections where animal loss is frequently found due to cardiac arrest or thoracic collapse, retrograde carotid artery in-

jection is well tolerated. Similar to the findings of Arguello et al., injection of 1 x 10^5 led to spinal metastasis in all animals [34].

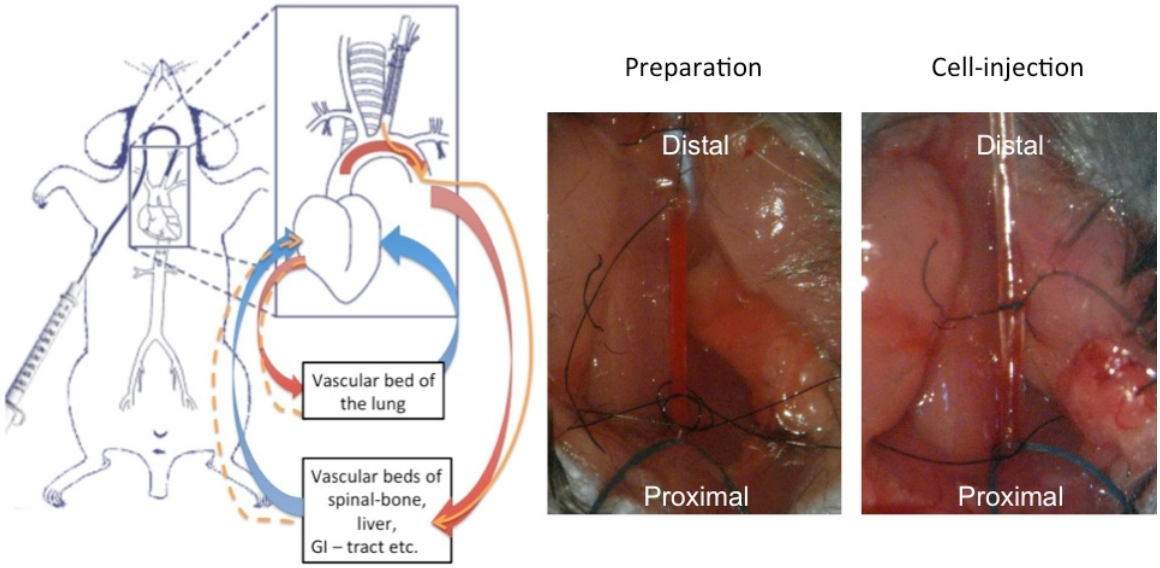

Figure 9: Schematic drawing of the injection protocol and operation window. *Schematic drawing shows hypothetical cell dissemination after retrograde carotid artery injection (red = arterial vessels, blue = venous vessels, orange line straight = direct cell flow and orange line doted = possible further cell flow). Operation window shows preparation prior to catheter insertion (left) and after catheter insertion and during cell injection (right).*

4.6.4 Bioluminescence imaging

Bioluminescence imaging was performed to identify tumor progression *in vivo* using the IVIS Lumina II (Caliper LS) equipment. Three mice could be imaged at the same time. The mice were anesthetized using 2% isoflurane, 10 µl / g BW of d-luciferin solution (30 mg / ml) were injected i.p. as described in the manufacturers protocol (Caliper LS). After 10 min the snout was placed into the isoflurane mask of the Lumina II. *In-vivo* luminescence was measured for 5 min dorsally and 5 min ventrally. This measurement was repeated 5 days, 10 days, 15 days, 20 days and 25 days post operation or at day of phenotype. At the day of phenotype *ex-vivo* luminescence of dissected organs was performed to determine the exact number of metastatic cells.

4.6.5 Magnetic resonance imaging

MRI was performed to identify spinal metastasis loci and progression, using a 7 Tesla rodent scanner (Brucker Pharmascan 70/16AS) with a 16 cm horizontal bore magnet and a ^{1}H-RF-Volumeresonator (72mm) for transmission (Rapid Biomed, Rimpar,

DE) were used. The H-resonance frequency was 300 MHz, the maximum gradient strength was 300mT/m. Paravision 5.1 (Brucker) was used to acquire the images. Mice were anesthetized using 2% isoflurane in O_2/NO_2 (30/70%). Anesthetized mice were placed dorsally on top of a 37°C heating pad with the incisures fixed and constant anesthesia supplied. Ventilation was monitored throughout the scan. A T2-weighted 2D turbo spin-echo sequence was used to visual the spinal cord. 10 sagittal slices (h x l x w = 0.5 x 30 x 30 mm) were positioned over the spine.

4.6.6 Magnetic resonance imaging data analysis

The data was analyzed with Amira software™. Spinal bone tumors were identified using threshold tool and false coloring. Conversion from T2 MRI to false color images is shown in *Figure 10*. False coloring allowed for better quantification of images with varying intensity (*Figure 10*). Tumor volume was assessed by measuring tumor area over one or more sagittal planes ($V = \sum_n^1 A(tumor)\ x\ h(slice)$). The following parameters were quantified: number of spinal metastasis per animal, mean tumor size of individual spinal metastasis in each animal (mean tumor volume) and total tumor size of all spinal metastasis per animal (total tumor volume).

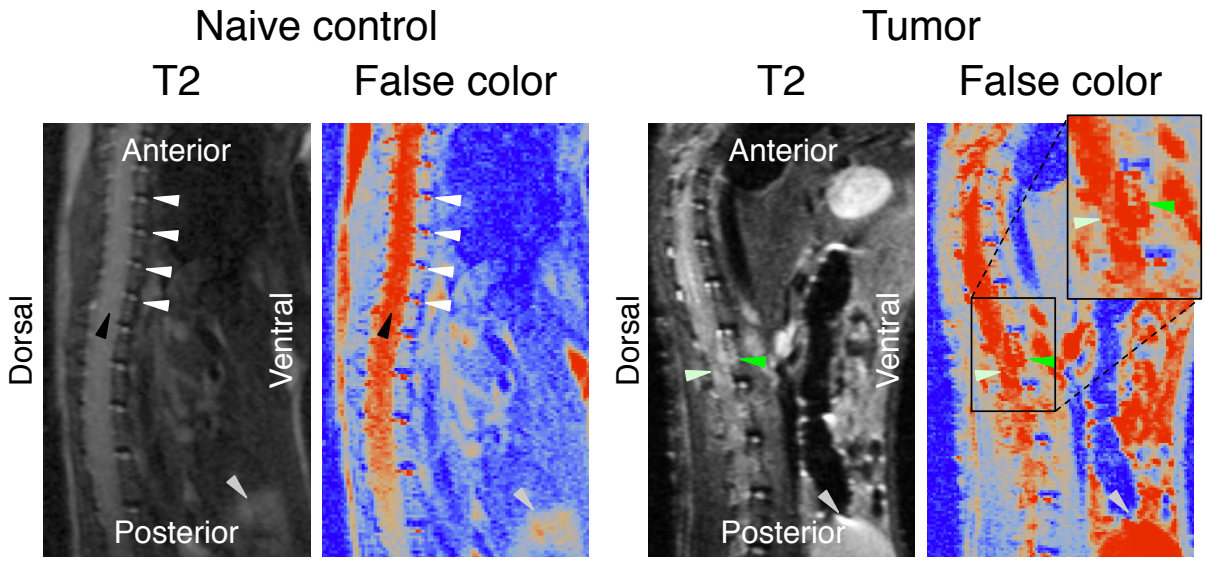

Figure 10 MRI Amira analysis of images with different intensity. *A naive animal shows no sign of spinal cord compression in the T2 MRI sagittal sequence (left, black arrowheads indicate spinal canal). Spinal disks (white arrowheads) are properly aligned and no signs of tumor growth in the vertebral segments are observed. Bladder shows no abnormality (gray arrowhead). Spinal metastatic mice (right) showed different spinal changes. Tumors formed in the vertebral body of spinal segments (green arrowhead). Tumor – myelon compression can be identified using false color images (light green arrowhead). Bladder in mice with neurological deficit was enlarged (gray arrow).*

4.6.7 Immunofixation, cutting and staining

At the day of phenotype mice were killed by cervical dislocation, all organs were harvested and frozen in isopentane at -50°C. Organs were transferred to -80°C for long-term storage. Frozen tissue was embedded in “Tissue Tek” immediately before cutting. Coronal spine sections (25µm) were obtained, air-dried and fixed with 4% PFA for 15 min at RT. Fixed Tissue was blocked in 1% Casein / PBS for 30 min at RT. Primary antibody incubation was performed O/N at 4°C in 0.5 % Casein / PBS (antibody concentration described in Table 4: Antibodies). Sections were washed 3 times with 0.5% Casein / PBS for 5 min at RT. Secondary antibody was incubated for 2 h at RT. Sections were again washed 3 times with PBS for 5 min at RT. Slides were finally embedded using tissue embedding medium Immu-Mount (Thermo Fischer) covered with a glass cover slip. Images were obtained using an Axioscope2 microscope (Zeiss) and Axiovision 3 software (Zeiss)

4.6.8 Tissue Homogenization

For microbeads and cells dissemination, the animals were sacrificed 3 h post beads / tumor cell injection. For metastasis experiments mice were sacrificed at the occurrence of neurological deficits. Multi-organ resection was performed and the organs were frozen in isopentane. Using mortar and pestle hard tissue was homogenized to fine powder at -80°C, cooling with liquid nitrogen. The powder and soft tissue organs were transferred to individual gentle macs tubes. Luciferase lysis buffer was added as followed to soft tissues and to grinded hard tissues: Cranium 5 ml, forelimbs 5 ml, hindlimbs 10 ml, spine 2 ml, thorax 5 ml, brain 5 ml, heart 2 ml, kidney 2 ml, liver 5 ml, skin 10 ml, spleen 2 ml. Dispomix profile 4 (4000 rpm for 15 sec) was performed 4 times. Tissues were kept on ice constantly, 200µl of homogenized tissue was stored as backup. Macs tubes were centrifuged for 5 min at 1200 g / 4° C and 200µl of the supernatant was decanted. Luciferase assay was performed as described in paragraph 4.4.6 and previously [24]. Beads were excited at 485 nm and 530 nm emission was measured.

4.6.9 Mouse behavior analysis

Mice were checked daily for the occurrence of neurological deficits. The occurrence of partial or complete hindlimb paresis in combination with epidural myelon compression by spinal metastasis was defined as neurological deficit.

4.7 Statistics

The diagram error bars indicate +/- of standard deviation (SD). GraphPad Prism was used to compare data between two and more independent group measurements. The statistical test used for the individual experiments are indicated in the corresponding figure legend. One star (*) indicates $p \leq 0.05$, two stars (**) indicate $p \leq 0.01$ and three stars (***) indicate $p \leq 0.001$.

Materials and Methods were partially adapted from [70]

5 Results

5.1 *In-vitro* cell line characterization

5.1.1 Lentiviral infection of B16-F1 melanoma

Lentivirally infected B16-luc and re-cultivated mB16-luc cells showed strong GFP expression *in-vitro* (*Figure 11 A*). Luciferase activity was verified by *in-vitro* luminescence measurement (*Figure 11 B*). B16-luc showed strong relative light unit (RLU) production 136.7 ± 42.73 (mean ± SD) after D-Luciferin supplementation compared to uninfected B16-F1 controls 6.4 ± 10.53. mB16-luc showed reduced luminescence 89.0 ± 36.27 compared to B16-luc but still robust RLU excitation over B16-F1.

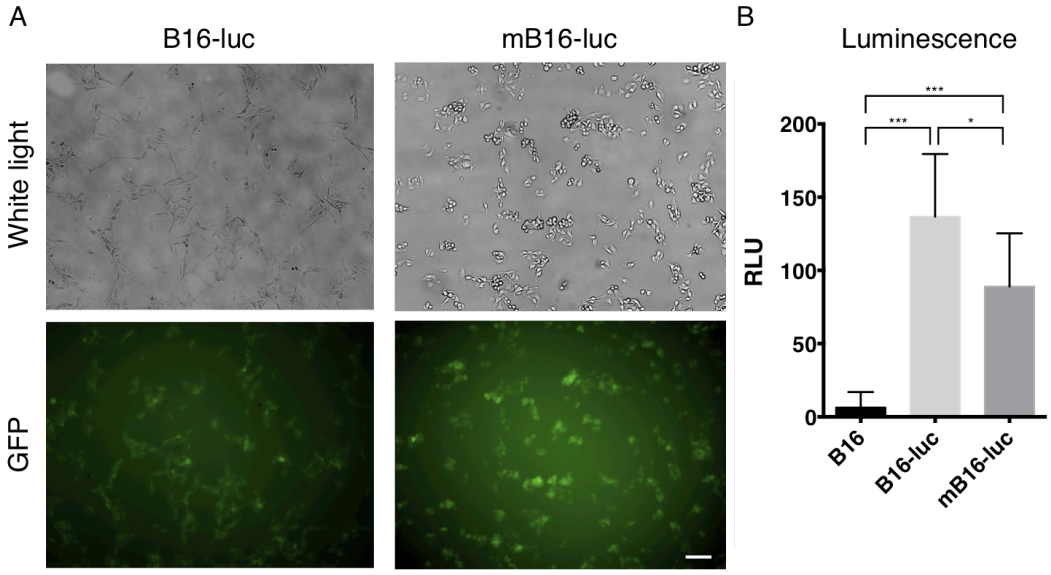

Figure 11: Characterization of B16-luc and mB16-luc cells. *B16-F1 melanoma cells were lentivirally transduced to express fire fly luciferase, enhanced GFP and puromycin (B16-luc). Two weeks post puromycin selection GFP fluorescence was observed. Metastatic B16 cell (mB16-luc) were explanted from vertebral metastasis and re-cultivated with puromycin for 2 more weeks. A) Representative phase contrast and green fluorescence image of B16-luc and mB16-luc cells (scale bar = 100µm). B) Luciferase activity shows relative light units (RLU) emitted by lysed cells post d-luciferin supplementation. Effects were compared by one-way ANOVA ($p<0.0001$) followed by Bonferroni post hoc analysis, mean +/- SD for all experiments shown.*

5.1.2 Expression analysis of B16-luc and mB16-luc cells

The characterization of gene expression changes was performed for six major angiogenic genes: Angeopoetin-1 (Ang1), Angeopoetin-2 (Ang-2), Notch1, EphB4, ephrinB2 and vascular endothelial growth factor (VEGF). RT-PCR expression analy-

sis of B16-luc and mB16-luc compared to B16-F1 control cells was performed (*Figure 12*). Ang1 (4.1 ± 2.0) and EphB4 (51.6 ± 10.6) mRNA were significantly upregulated after lentiviral infection and VEGF (0.0027 ± 0.0031) mRNA was significantly down-regulated. No significance was found for Ang2 (1.8 ± 0.3), ephrinB2 (2.1 ± 0.5) and Notch1 (0.37 ± 11). Only EphB4 (16.9 ± 7.8) mRNA was significantly upregulated in primary explanted mB16-luc. VEGF (0.017 ± 0.0033) was significantly down regulated. The expression of Ang1 (1.8 ± 0.1), Ang2 (0.64 ± 0.017), Notch1 (5.9 ± 1.1) and ephrinB2 (4.5 ± 1.6) did not show significant changes (B16-F1 mRNA expression = 1).

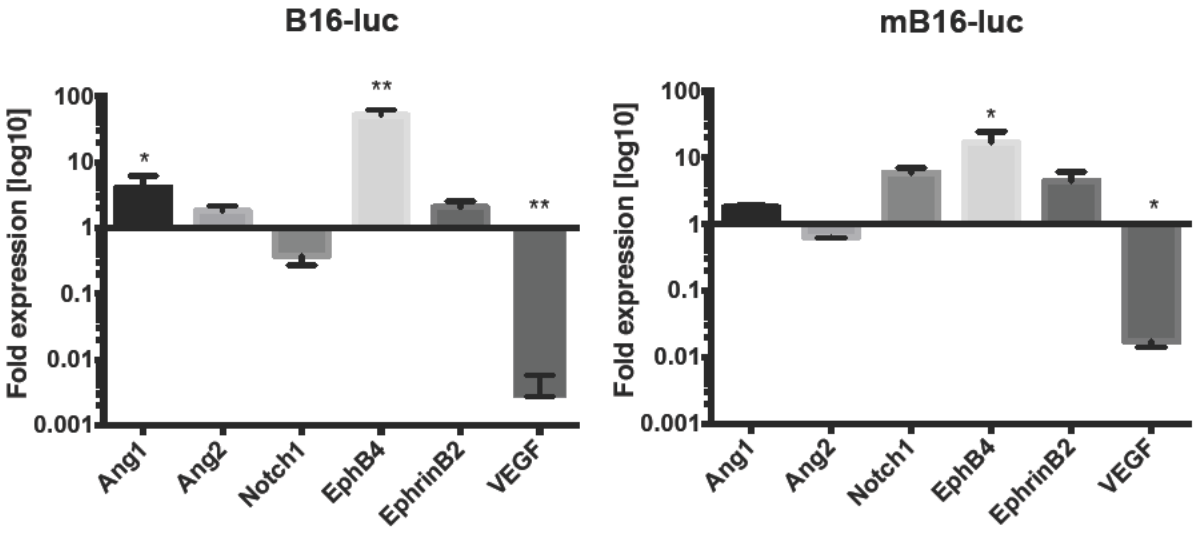

Figure 12: qPCR expression analysis of B16-luc and mB16-luc cells. *Regulatory changes of six major angiogenic genes in B16-luc and mB16-luc compared to B16-F1 controls (B16-F1 = 1). RT-PCR shows regulation of Ang1 (B16-luc p=0.0228), Ang2, Notch1, EphB4 (B16-luc p=0.0044, mB16-luc p=0.0198), ephrinB2 and VEGF-A (B16-luc p=0.0040, mB16-luc p=0.0165). Student's two-tailed t-test, n=3, mean +/- SD for all experiments shown.*

Comparison of angiogenic gene expression in mB16-luc to B16-luc revealed significantly increased Notch1 (16.1 ± 2.96), ephrinB2 (2.2 ± 0.8) and VEGF (9.8 ± 1.9) mRNA levels and decreased Ang2 (0.36 ± 0.01) and EphB4 (0.33 ± 0.15) mRNA expression. Ang1 (0.48 ± 0.029) was unchanged (*Figure 13*).

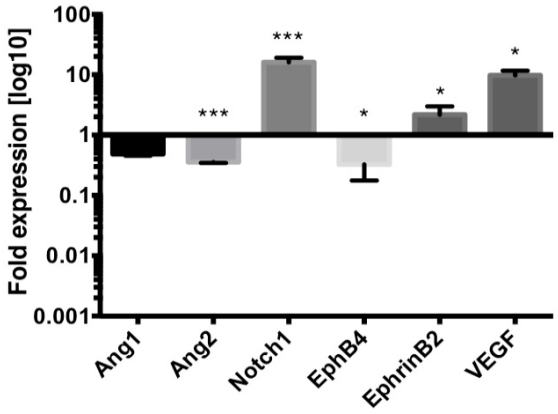

Figure 13: qPCR expression analysis mB16-luc compared to B16-luc cells*. RT-PCR showed significant mRNA expression changes to the angiogenic genes in mB16-luc cells. Ang2 (p=0.0006), Notch1 (p=0.0001), EphB4 (p=0.0293), ephrinB2 (p=0.0354) and VEGF-A (p=0.0249) are significantly altered and Ang1 was unchanged. Student's two-tailed t-test, n=3, mean +/- SD for all experiments shown.*

5.1.3 Migration and viability of B16-luc and mB16-luc cells

Migration characteristics were measured using standard scratch / wound healing assay *in-vitro*. The mB16-luc cells closed the wound faster compared to B16-luc cells (*Figure 14*). Consequently, migration speed of mB16-luc (16.14 ± 1.89) was significantly higher compared to B16-luc (10.30 ± 3.72).

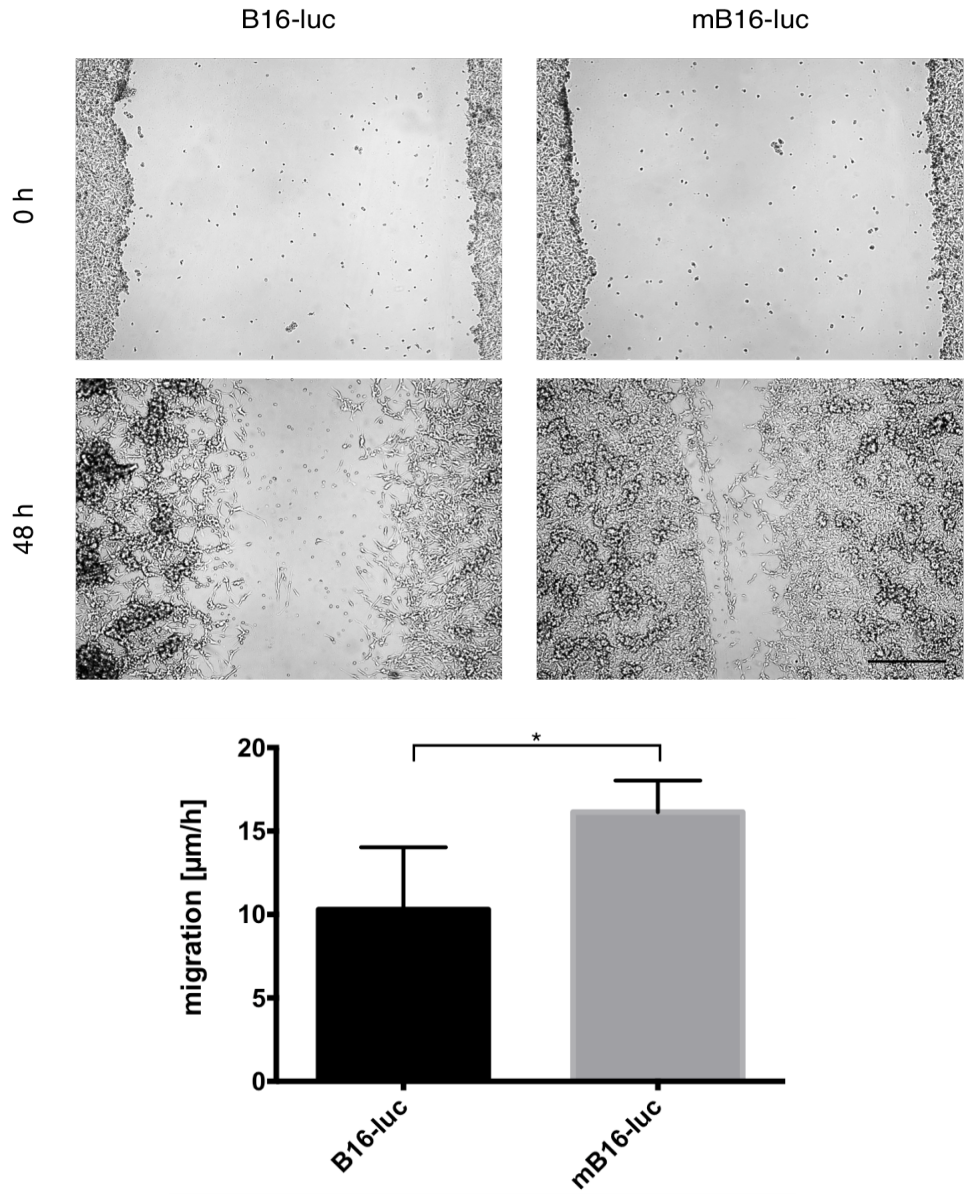

Figure 14: Migratory analysis of B16-luc and mB16-luc cells. *Representative images of scratch assay performed with B16-luc and mB16-luc at time points 0 h post scratch and 48 h end point (Scale bar = 500 µm). Migration speed analysis showed significant difference between the B16-luc and mB16-luc cells (p=0.0254). Student's two-tailed t-test, n=3, mean +/- SD for all experiments shown.*

Cell viability was measured by MTT assay controlled to B16-F1 (100%). Cells were seeded at different densities A: 2500, B: 5000 and C: 10000 cells per 96 well (*Figure 15*). B16-luc cells showed significantly higher viability compared to mB16-luc cells (B16-luc A: 104.3% ± 6.3, B: 115.8 ± 8.9, C: 123.5 ± 12.0; mB16-luc A: 85.25 ± 4.8, B: 91.2 ± 12.8, C: 94.0 ± 7.5).

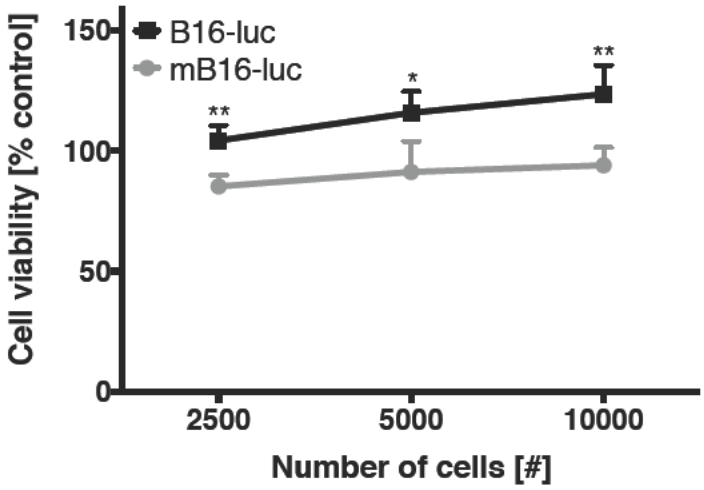

Figure 15: MTT cell viability analysis of B16-luc and mB16-luc cells. *B16-luc cells showed significantly higher viability at all cell densities (2500 cells / 96 well p=0.0031, 5000 cells / 96 well p=0.0198, 10000 cells / 96 well p=0.0059) 24 h post seeding compared to mB16-luc (normalized to B16 cell viability = 100%). Student's two-tailed t-test, n=5, mean +/- SD for all experiments shown.*

5.1.4 Retroviral infection of B16-luc with EphB4

B16-luc cells were treated with PhoenixECO isolated viruses. PhoenixECO cells expressed mouse specific retroviruses carrying pLXSN-EphB4 or pLXSN (control) constructs. Verification of EphB4 overexpression at the protein level by western blot showed a strong 108kDa EphB4 band in B16-luc-EphB4 cells and light band in B16-luc-pLXSN. Protein loading was controlled with beta Actin (*Figure 16*).

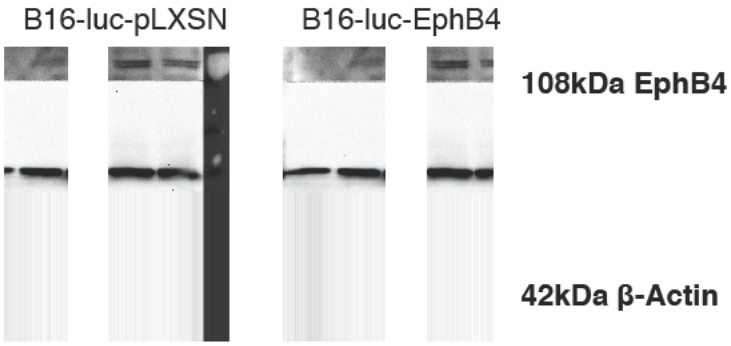

Figure 16: Western blot of B16-luc cells infected with pLXSN empty vector / EphB4 vector. *B16-luc-pLXSN showed light band of 108kDa EphB4 and B16-luc-EphB4 shows strong EphB4 band. Protein loading was controlled by 42kDa beta Actin, n=3.*

5.1.5 Migration and viability of B16-luc-pLXSN and B16-luc-EphB4 cells

Scratch / wound healing assay identified cellular migration of B16-luc-EphB4 cells and B16-luc-pLXSN controls after 48 hours. B16-luc-EphB4 cells (20.20 ± 1.22) closed the wound significantly faster compared to B16-luc-pLXSN cells (10.87 ± 1.4) control cells (*Figure 17*).

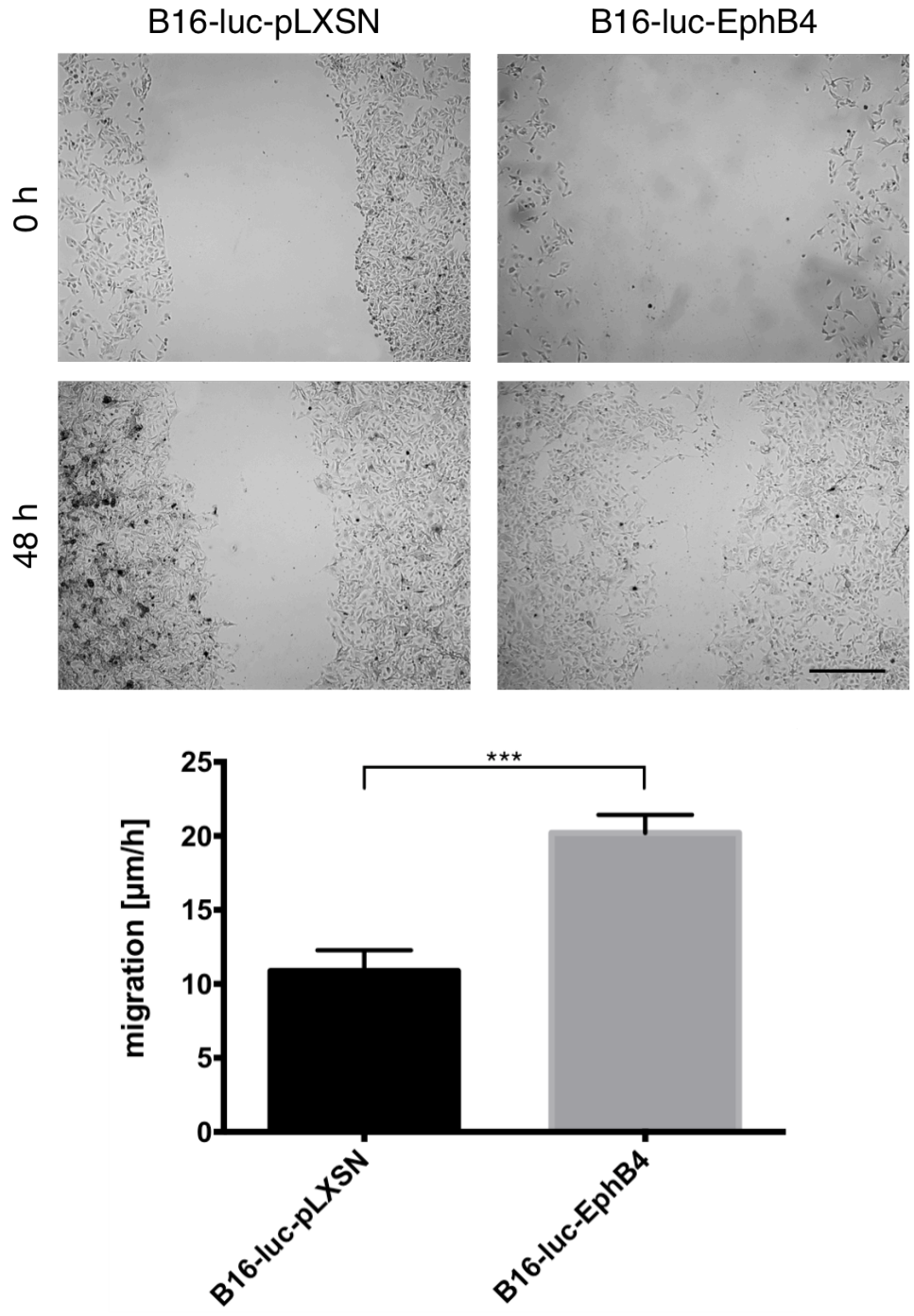

Figure 17: Migratory analysis of B16-luc-pLXSN and B16-luc-EphB4 cells. *Representative images of scratch assay performed with B16-luc-pLXSN and B16-luc-EphB4 cells at time points 0 h post*

scratch and at the 48 h end point (scale represents 500 µm). Migration speed analysis showed significant differences between the B16-luc-pLXSN and B16-luc-EphB4 cells (p<0.0001). Student's two-tailed t-test, n=3, mean +/- SD for all experiments shown.

MTT cell viability was controlled against B16-luc-pLXSN cells (100%). B16-luc-EphB4 cells showed decreased cell viability at increased cellular density A: 112.8 ± 47.1, B: 87.5 ± 24.5, C: 55.9 ± 8.3 for A: 2500, B: 5000 and C: 10000 cells per 96 well (***Figure 18***).

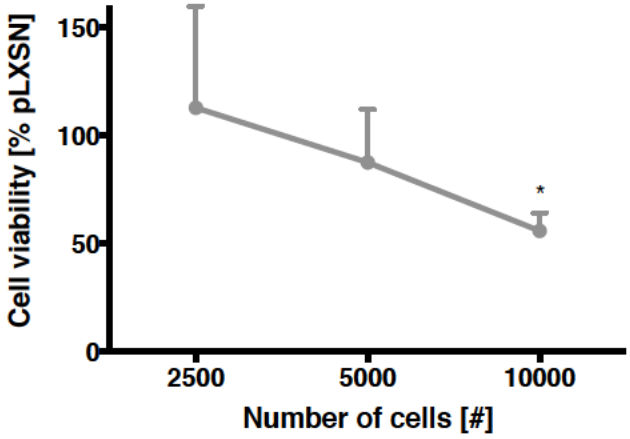

Figure 18: MTT cell viability assay of B16-luc-EphB4 cells. *B16-luc-EphB4 cells showed significant lower viability in high cell density seeding conditions 24 h post seeding (10000 cells / 96 well; p=0.0382, normalized to B16-luc-pLXSN cells = 100%). Student's two-tailed t-test, n=3, mean +/- SD for all experiments shown.*

5.2 *In-vivo* target validation

Expression of ephrinB2 in vertebral microvessels was verified by fluorescence immunohistochemistry. Blood vessels were stained with CD31 antibody (red). Pericytes were stained with desmin antibody (green). There was no co-localisation of desmin and CD31 (*Figure 17*). Double stain of CD31 (red) and ephrinB2 (green) identified vertebral microvessels expressed ephrinB2 (arrows). A co-stain of CD31 (red) and EphB4 (green) showed very weak EphB4 signal and no co-localisation in vertebral bone marrow.

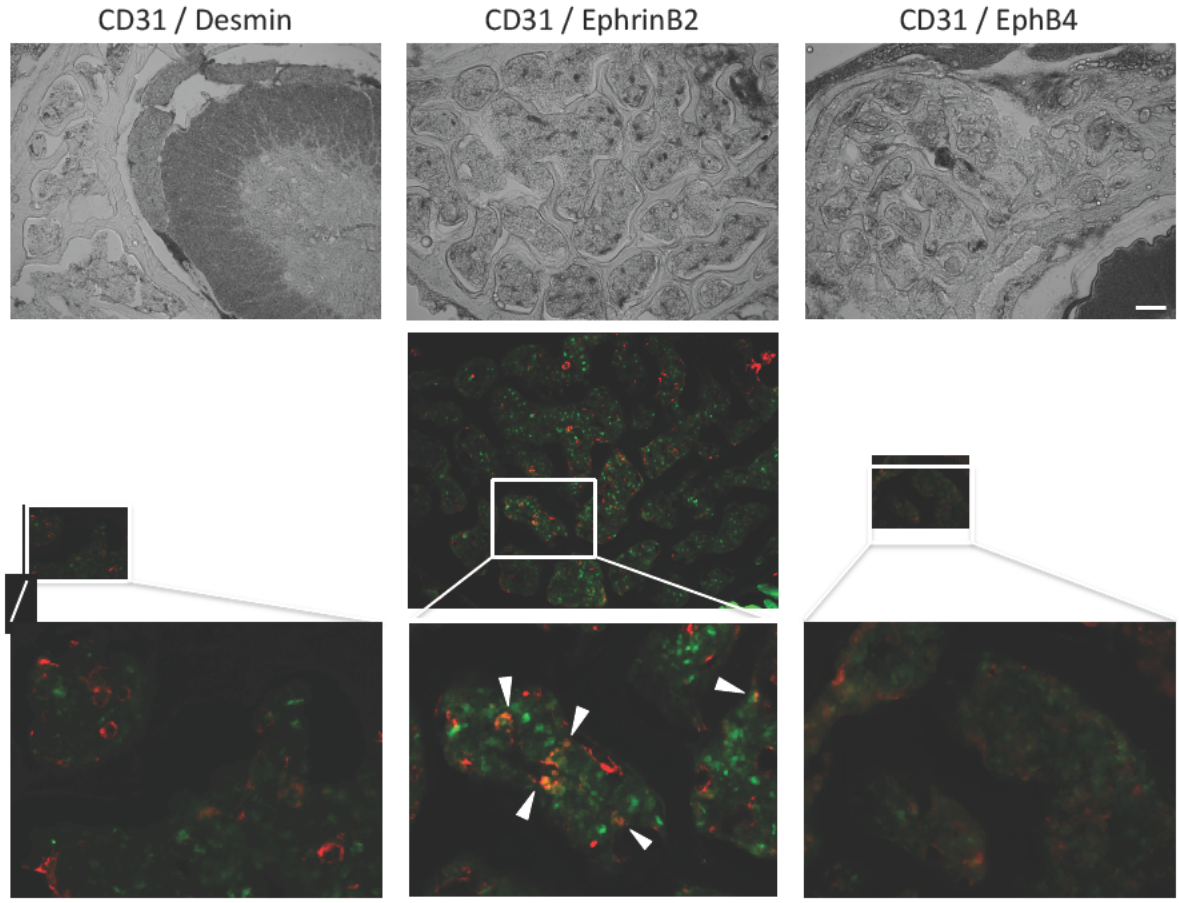

Figure 19: Vertebral bone marrow microvessels express ephrinB2. *Upper row: white light overview of the stained vertebral body cryo sections. Second row: corresponding overview of fluorescence immunohistochemistry. Last row: detailed magnification of the selected area (white square). CD31 / desmin showed no desmin positive pericytes in the bone marrow. Co-staining of CD31 and ephrinB2 showed strong ephrinB2 expression in bone marrow (green cells) and double positive vessels (yellow indicated by the arrowheads). EphB4 stained weak in vertebral bone marrow (n=3, scale bar = 100 µm)*

Endothelial cell specific knockdown of ephrinB2 was evaluated using lung tissue [71]. *Efnb2* mRNA reduction by $1.12 \times 10^{-5} \pm 1.53 \times 10^{-5}$ was found in lung tissue of *iΔefnb2* animals compared to *CDH5*-CreERT^2 negative controls (*efnb2*$^{lox/lox}$). Western blot of lung tissue showed a strong reduction of ephrinB2 in *iΔefnb2* mice compared to *CDH5*-CreERT^2 negative controls. *Beta actin* served as protein loading control (*Figure 20*).

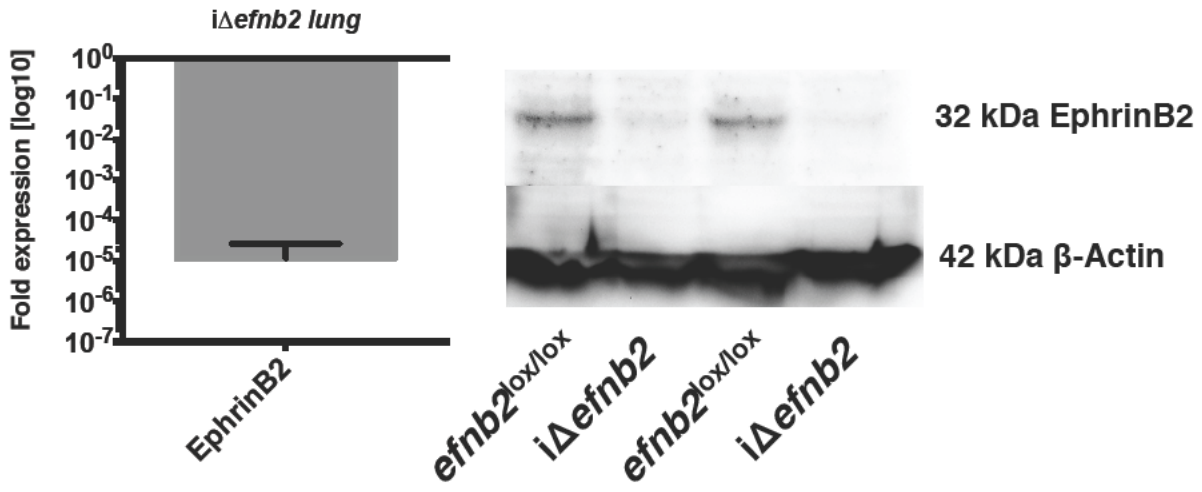

Figure 20: RT-PCR and western blot verification of endothelial ephrinB2 knockout. *Lung tissue isolated form tamoxifen induced endothelial specific ephrinB2 depleted animals showed strong reduction of ephrinB2 compared to control animals. Western blot of iΔefnb2 and efnb2$^{lox/lox}$ control lung tissue post tamoxifen induction. Endothelial ephrinB2 knockout could be verified on protein level. Beta actin served as loading control. Mean +/- SD, n=2 from independent litter for all experiments shown.*

5.3 Hematogenous spinal metastasis model characterization

Initial experiments focused on both particles and cells dissemination to different organs. In this regard dissemination represents a prerequisite for metastasis formation but does not necessarily lead to tumor cell extravasation or metastasis formation in organs, as these steps have to be defined down-stream of tumor cell dissemination.

5.3.1 Biologically inert particle dissemination

General biophysical dissemination of biological inert particles was evaluated using two particle sizes. First, particles approximately the size of the nucleus (7µm Ø) and second, particles approximately the size of the complete cell (16µm Ø) were used. The diameter size was based on the Casy Tone TT cell counter plot (*Figure 21 A*). A standard curve was determined, which defined fluorescence intensity of beads diluted over the range of: 200'000, 100'000, 50'000, 25'000, 12'500, 6'250, 3'125, 1'563, 781, 391, 195, 98, 49, 24 and 12. The resulting curves slope, (95% confidence interval) was 0.1812, (0.1761-0.1864) and 0.3766, (0.3655-0.3876) for 7µm Ø and 16µm Ø respectively (*Figure 21 B*).

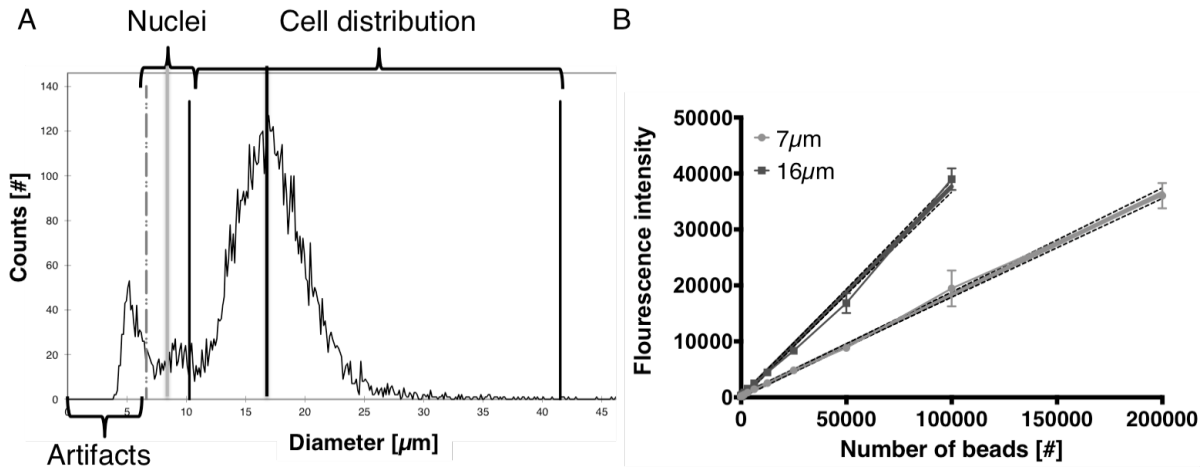

Figure 21: Definition and fluorescence intensity standard curve of biologically inert fluoresce cent particles *A) Casy TT cell count plot of B16-luc cells indicated nuclei diameter of 7-10μm and mean cell diameter of 16μm (+/- 5μm). Measurements below 6μm were considered artifacts. B) Standard curve links fluorescence intensity with the number of microbeads, which emitted the light. Beads with 16μm diameter emitted more light per bead compared to the smaller 7μm beads (7μm R^2: 0.9915, 16μm R^2: 0.9916, doted lines represent 95% confidence interval, bold lines represent calculated standard curve, thin gray lines represent individual values). N=3, mean +/- SD for all experiments shown.*

Organ dissemination of biologically inert particles was achieved after injection of 100'000 particles retrograde into the left carotid artery. Multiorgan resection was performed 3 hours post injection. Microbead dissemination varied strongly between different organs. The greatest microbead dissemination was in organs that have high perfusion and / or tissue volume. These organs were kidneys (22649 ± 12138 [7μm Ø beads / organ] / 14830 ± 3836 [16μm Ø beads / organ]), liver (14912 ± 2881 [7μm Ø beads / organ] / 15371 ± 2126 [16μm Ø beads / organ]) and skin (11003 ± 4792 [7μm Ø beads / organ] / 11742 ± 1084 [16μm Ø beads / organ]). Beads load of other soft tissues was comparably low (*Figure 22*). Interestingly, the injection showed also relatively little dissemination to osseous microvessels (*Figure 22*).

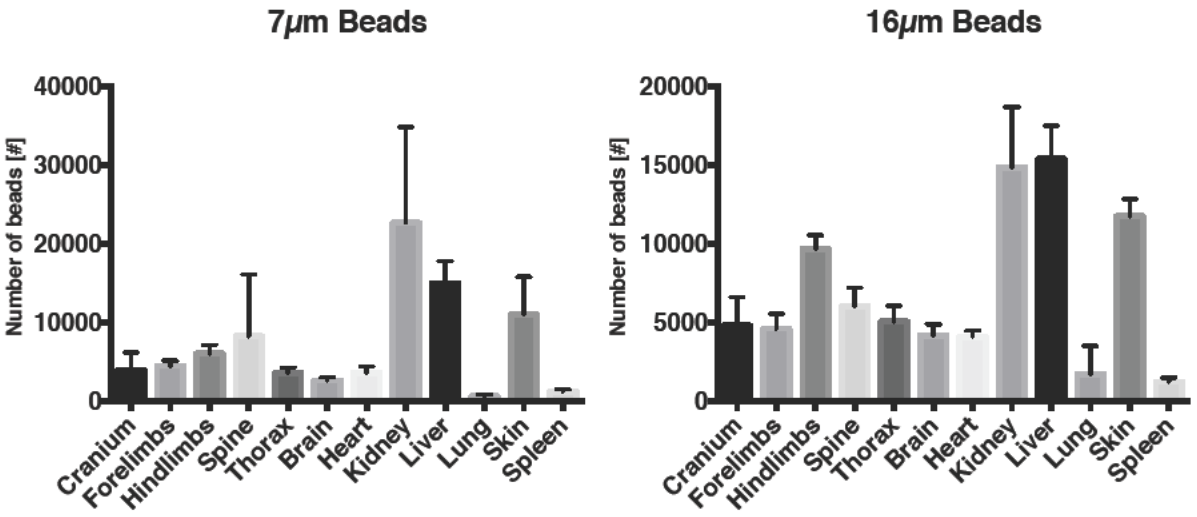

Figure 22: Complete organ dissemination analysis of biologically inert particles. *Organs were homogenized and lysed 3 hours post injection. Biologically inert particles disseminated preferably in skin, kidney and liver. (n=5, mean +/- SD for all experiments shown).*

Further, we compared total beads disseminated to osseous and other organs. Biologically inert particles of 7µm Ø (bone: 26260 ± 11734, other: 51612 ± 16250) and 16µm Ø (bone: 30138 ± 3033, other: 53143 ± 5150) show significant initial dissemination preference towards none osseous organs (*Figure 23*).

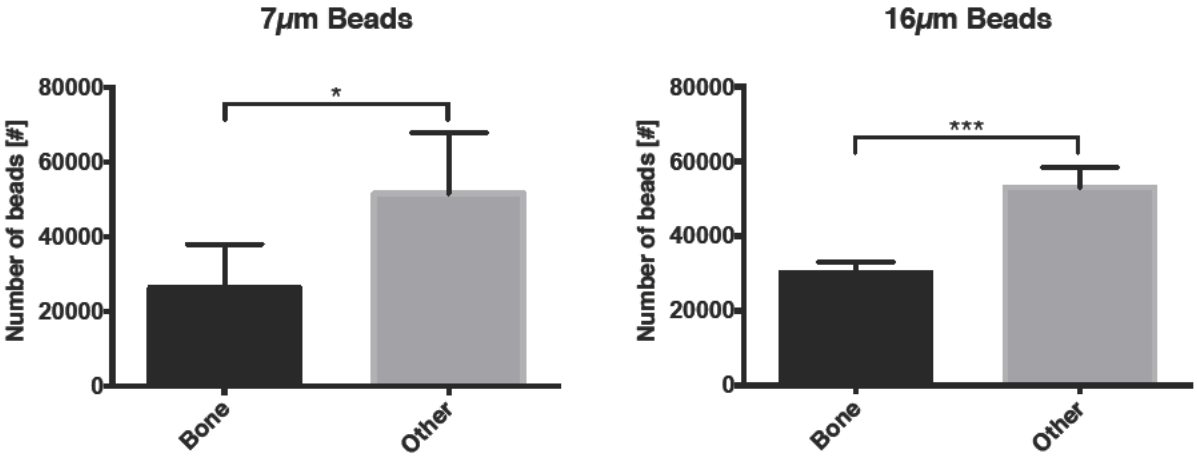

Figure 23: Beads dissamination to bone and other organs. *Beads independent of their diameter (7µm p=0.0222 and 16µm p=0.00005) showed dissemination preference towards non-bone microvasculature. Student's two-tailed t-test, n=5, mean +/- SD for all experiments shown.*

5.3.2 B16-luc and mB16-luc cell dissemination

As described before a standard curve was generated plotting relative light units (RLU) against the number of cells emitting light (# Cells). Cells were counted and diluted to numbers of: 100000, 50000, 25000, 12500, 6250, 3125 and 1563. The slope of the standard curve (95% confidence interval) was: 35.45 (31.93 to 38.97) for B16-luc, 17.55 (16.04 to 19.06) for mB16-luc (*Figure 24*).

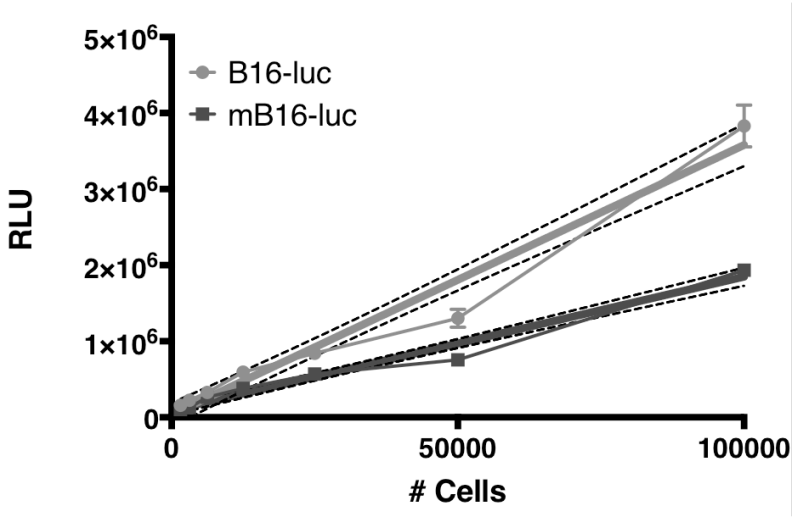

Figure 24: Standard curve of B16-luc and mB16-luc cells. *Standard curve plots luciferase photon emission in relative light units (RLU) versus number of B16-luc and mB16-luc cells (B16-luc R^2: 0.9589, mB16-luc R^2: 0.9689, doted lines represent 95% confidence interval, bold lines represent calculated standard curve, thin gray lines represent individual values). N=3, mean +/- SD for all experiments shown.*

B16-luc and mB16-luc cells were injected and their organ dissemination was analyzed 3 hours later. B16-luc cells disseminated preferably to lung (93 ± 78.12 cells / organ) whereas all other organs were low: cranium (10 ± 5.8 cells / organ, forelimbs (24.56 ± 7.4 cells / organ), hindlimbs (0 ± 5.9 cells / organ), spine (0 ± 16 cells / organ), thorax (23 ± 36.3 cells / organ), brain (0 ± 6 cells / organ), heart (10 ± 13 cells / organ), kidney (12 ± 22.6 cells / organ), liver (8 ± 13 cells / organ), skin (2 ± 11 cells / organ), spleen (6 ± 8 cells / organ). Generally increased dissemination to every organ studied was found in mB16-luc experiments, indicating a selection towards a more aggressive tumor cell subtype, which is better adapted to dissemination in the circulatory system. Metastatic B16-luc cells (mB16-luc) retained the preference for lung (552 ± 188 cells / organ) dissemination, but also showed high affinity towards skin vasculature (622 ± 217 cells / organ). The remaining organs showed equal dissemination (*Figure 25*).

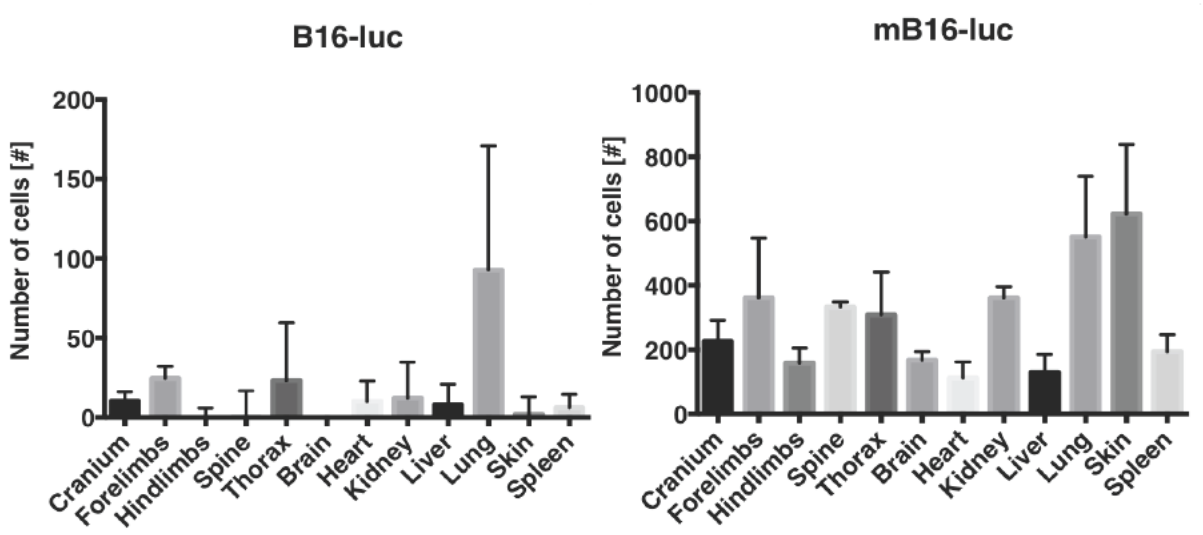

Figure 25: Complete organ dissemination analysis of B16-luc and mB16-luc cells. *B16-luc organ analysis revealed high intrinsic dissemination preference for lung tissue over all other tissues. Higher baseline dissemination was found in mB16-luc compared to B16-luc cells. The initial preference for lung tissue remained and was supplemented by skin, kidney, forelimbs, thorax and spine. N=5, mean +/- SD for all experiments shown.*

The comparison of the dissemination between bone and other organs of B16-luc cells revealed no bone preference (bone: 58 ± 51 cells / organ, other: 107 ± 114 cells / organ). In contrast, mB16-luc cells showed significantly higher dissemination to non osseous organs (bone: 1385 ± 207 cells / organ, other: 2136 ± 109 cells / organ, *Figure 26*).

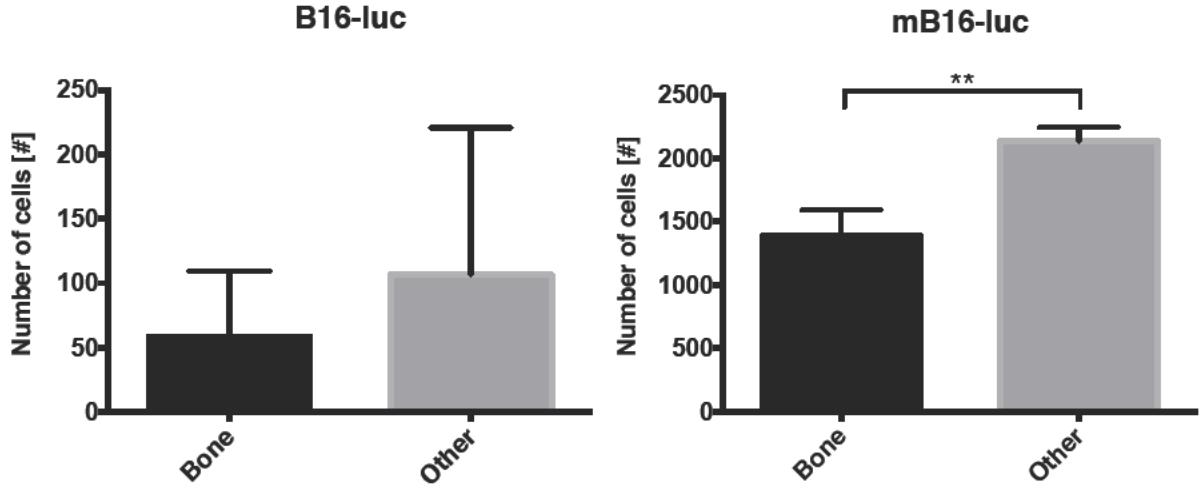

Figure 26: B16-luc and mB16-luc cell dissamination to bone and other organs*. B16-luc cells showed no initial dissemination preference to bone microvasculature versus other vascular beds.*

Stronger dissemination to soft tissue organs was found in mB16-luc (p=0.0051). Student's two-tailed t-test, n=5, mean +/- SD for all experiments shown.

5.3.3 B16-luc-pLXSN and B16-luc-EphB4 cell dissemination

Standard curve plots RLU against the number of B16-luc-pLXSN or B16-luc-EphB4 cells. Stable tumor cell clones were counted and diluted to numbers of: 100000, 50000, 25000, 12500, 6250, 3125, 1563, 781, 391 and 195. The standard curve slope (95% confidence interval) was: 50.62 (49.46 to 51.79) for B16-luc-pLXSN and 41.26 (39.52 to 43.00) for B16-luc-EphB4 cells (*Figure 27*).

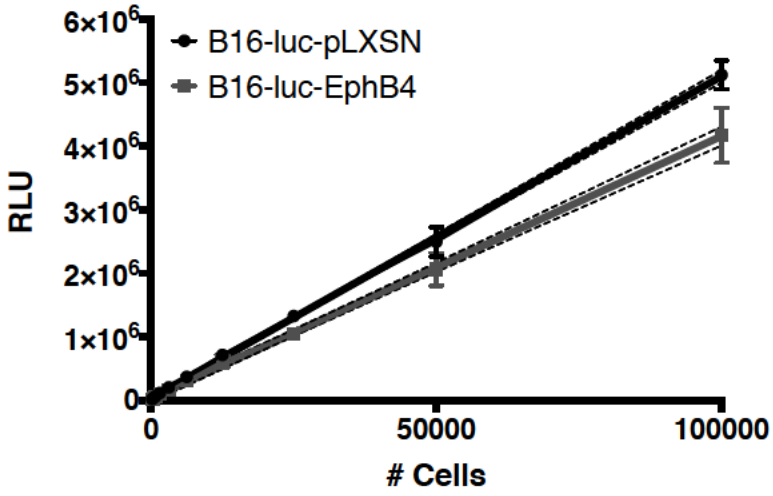

Figure 27: Standard curves of B16-luc-pLXSN and B16-luc-EphB4 cells. *Standard curve plots luciferase photon emission in relative light units (RLU) versus number of cells (B16-luc-pLXSN R^2: 0.9965, B16-luc-EphB4 R^2: 0.9883, doted lines represent 95% confidence interval, bold lines represent calculated standard curve, thin gray lines represent individual values). N=3, mean +/- SD for all experiments shown.*

Dissemination of B16-luc-pLXSN and B16-luc-EphB4 clones was analyzed 3 hours post 1 x 10^5 cell injection retrograde into the carotid artery. Luminescence of the organ lysates was measured and total cell dissemination to different organs was calculated with individual standard curve parameters (*Figure 28*). B16-luc-pLXSN control cells demonstrated preferred dissemination to the lung (814 ± 639 cells / organ). Moreover, strong cell dissemination was found to forelimbs (287 ± 193 cells / organ). Low cell numbers were found in other organs analyzed (*Figure 28*). B16-luc-EphB4 demonstrated lower and more diverse organ dissemination (*Figure 28*). Highest number of cells was discovered in the lung (251 ± 85 cells / organ).

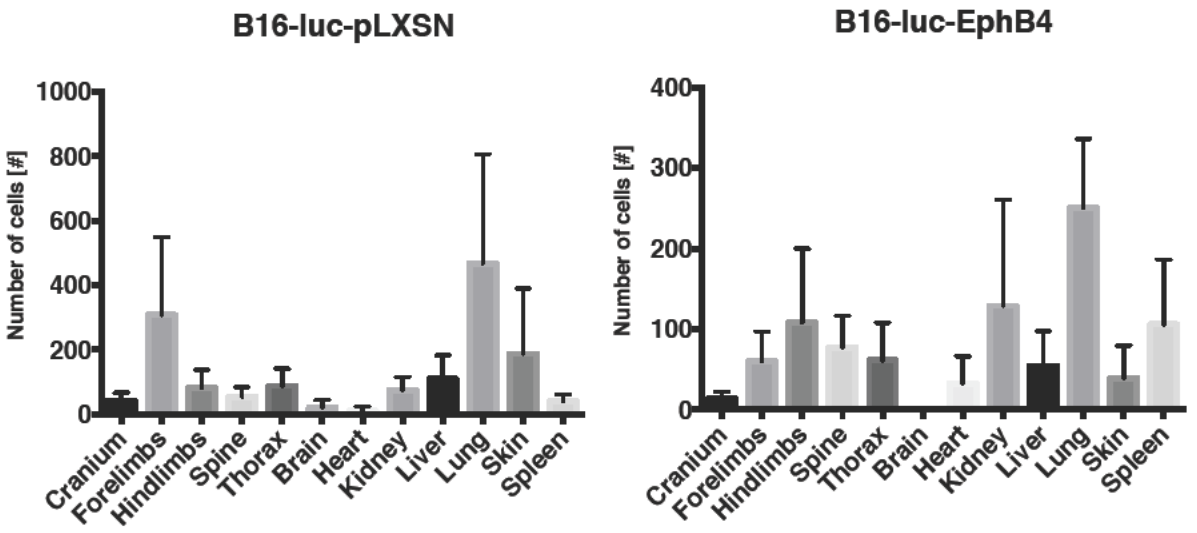

Figure 28: Complete organ dissemination analysis of B16-luc-pLXSN and B16-luc-EphB4 cells. *B16-luc-pLXSN organ analysis showed high dissemination preferences for lung and forelimb tissue over other tissues. B16-luc-EphB4 cells showed generally equal and reduced dissemination. The preference for lung tissue remained. N=5, mean +/- SD for all experiments shown.*

A comparison of osseous and soft tissue organs showed no preference to either microvasculature bed for B16-luc-pLXSN (bone: 261 ± 525 cells / organ other: 998 ± 717 cells / organ). In contrast, B16-luc-EphB4 cells showed significantly higher dissemination to soft tissue organs (bone: 322 ± 90 cells / organ other: 612 ± 206 cells / organ, *Figure 29*).

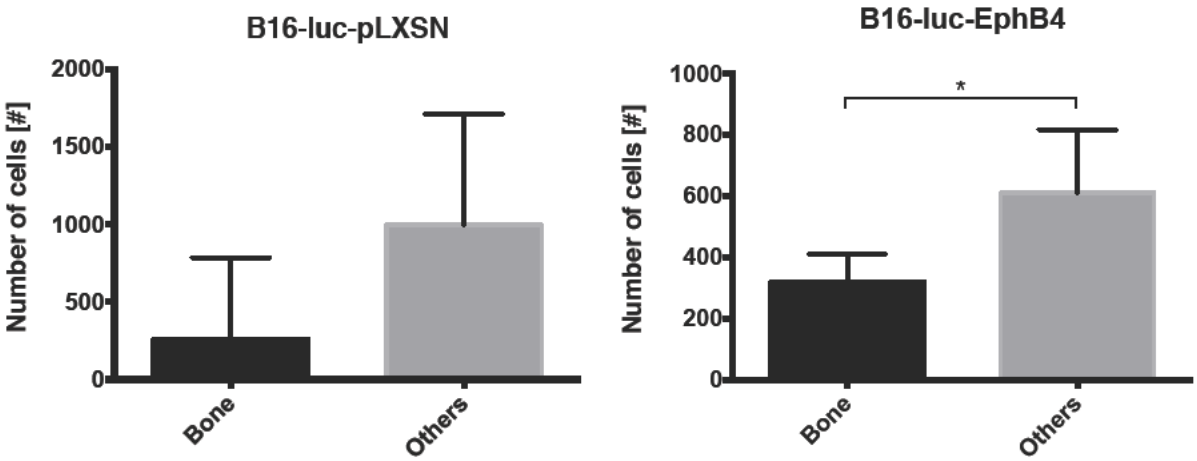

Figure 29: B16-luc-pLXSN and B16-luc-EphB4 cell dissamination to bone and other organs. *B16-luc-pLXSN cells showed no initial dissemination preference to bone microvasculature versus other vascular beds. B16-luc-EphB4 clones showed significantly higher dissemination to non-osseous organs. Student's two-tailed t-test, * p=0.02, n=5, mean +/- SD for all experiments shown.*

5.3.4 B16-luc-EphB4 cell dissemination changes in control animals

In order to analyze differences in dissemination behavior, B16-luc-pLXSN control cell dissemination was subtracted from B16-luc-EphB4 cell dissemination (Δ number of cells). B16-luc-EphB4 cells disseminated different to B16-luc-pLXSN control cells. Cranium (-28 ± 8), forelimbs (-248 ± 37 cells / organ), thorax (-26 ± 47) brain (-21 ± 17 cells / organ), liver (-54.66 ± 43), lung (-217 ± 85 cells / organ) and skin (-148 ± 41 cells / organ) revealed fewer disseminated cells compared to controls. Bone compared to soft tissue was shown in *Figure 29*.

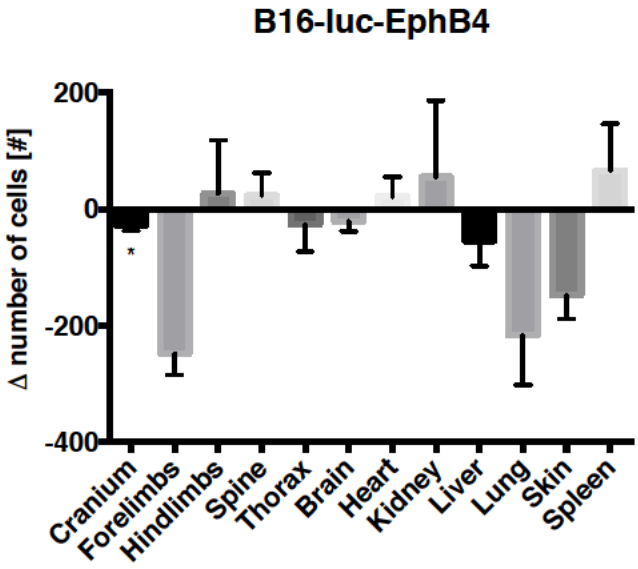

Figure 30 Complete organ dissemination difference of EphB4 overexpression to pLXSN control cells. *B16-luc-EphB4 cells show significant dissemination differences to cranium (p=0.03). Highly decreased fore limbs, lung and skin dissemination, although not significant was found. (Student's two-tailed t-test, n=5, mean +/- SD for all experiments shown).*

5.3.5 Dissemination of B16-luc cells in response to pharmacological intervention with ephrinB2 – EphB4 signaling

Two different agents were chosen to manipulate the ephrinB2 – EphB4 system. First, the extracellular domain of murine EphB4 fused to a mouse IGG long chain (EphB4-FC), was used to block extracellular interactions of ephrinB2 with EphB4 [24]. Second, NVP-BHG712 selectively inhibits the intercellular kinase of EphB4 and blocks phosphorylation dependent intracellular signaling [72]. Animals were sacrificed 3 hours post injection and multiorgan resection was performed. Dissemination of control animals (IGG antibody / vehicle injected) was subtracted from therapy animals cell dissemination (Δ number of cells). Significant higher cell dissemination to

hindlimbs (23 ± 17 cells / organ), spine (136 ± 119 cells / organ) and liver (37 ± 18 cells / organ) was found. Remaining organ cell dissemination was unchanged (brain (217 ± 169 cells / organ), cranium (117 ± 128 cells / organ), forelimbs (91 ± 121 cells / organ), thorax (-3 ± 22 cells / organ), heart (26 ± 39 cells / organ), kidney (30 ± 58 cells / organ), lung (10 ± 27 cells / organ), skin (16 ± 28 cells / organ), spleen (13 ± 23 cells / organ)). No dissemination preference to osseous organs was observed (367 ± 106 cells / organ) compared to other organs (427 ± 210 cells / organ) (*Figure 31 A*). After EphB4 kinase inhibition, more organs with significantly higher tumor cell counts were found (cranium (154 ± 99 cells / organ), hindlimbs (12 ± 5 cells / organ), spine (44 ± 30 cells / organ), brain (163 ± 106 cells / organ), liver (94 ± 75 cells / organ) and lung (271 ± 143 cells / organ). There was a significant shift in cell dissemination towards non-osseous organs (704 ± 254 cells / organ) compared to bony organs (295 ± 102 cells / organ) (*Figure 31 B*).

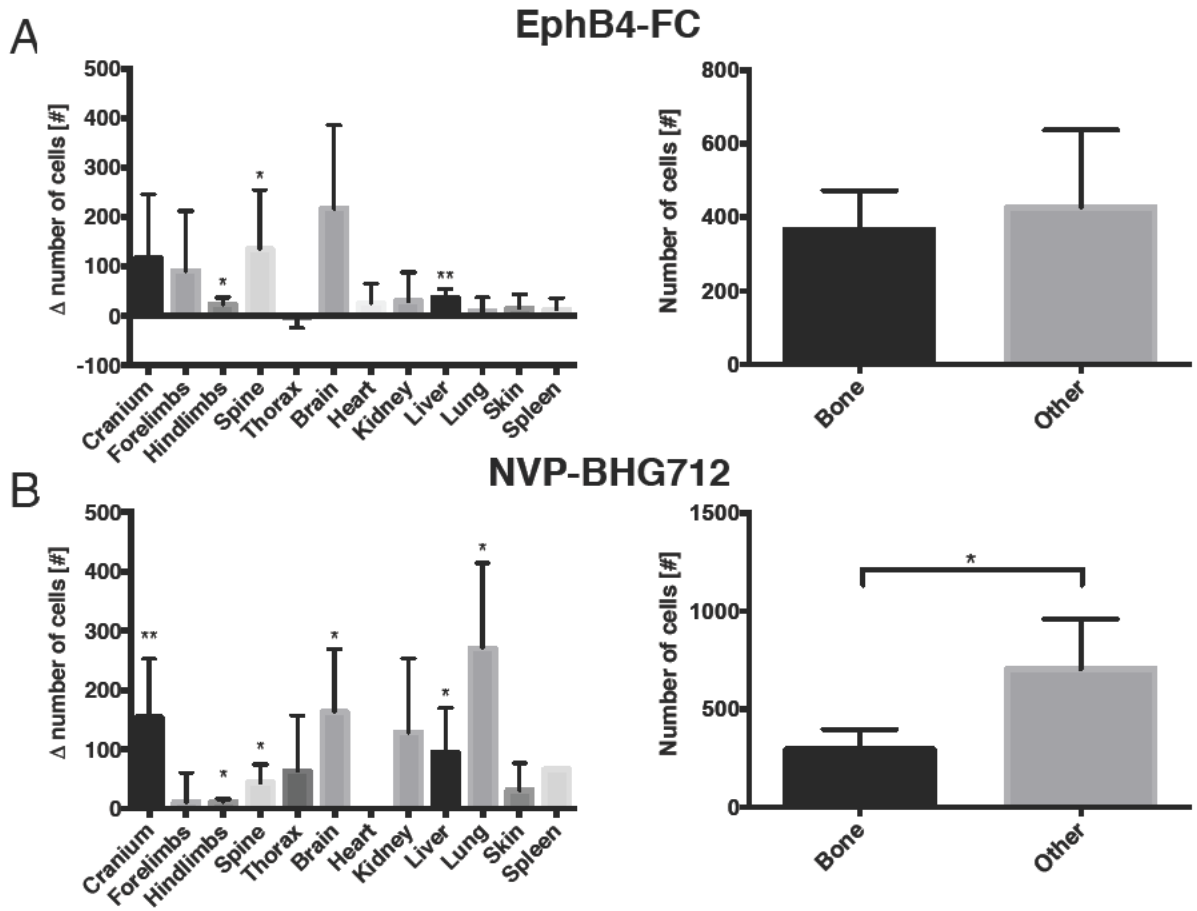

Figure 31: Complete organ dissemination analysis of B16-luc after EphB4 and ephrinB2 therapy including dissamination to bone and other organs. *Changes in cell dissemination were calculated by subtracting IGG-FC control injected groups from therapy groups (Δ number of cells). A) Adju-*

vant 1h therapy of EphB4-FC (20 µg i.p.) results in marginal increased cell dissemination. Three organs: hindlimbs (p=0.0176), spine (p=0.0476) and liver (p=0.0054) showed significant tumor cell dissemination increase. There is no dissemination preference for bone microvasculature. B) Adjuvant 25h and 1h therapy of EphB4 kinase small molecule inhibitor NVP-BHG712 (50 mg/kg i.p.) results in significant increased cell dissemination to six organs: cranium (p=0.0083), hindlimbs (p=0.0112), spine (p=0.0377), brain (p=0.0420), liver (p=0.0454) and lung (p=0.0120). This therapy resulted in dissemination preference for soft tissue organs (p=0.010). Student's two-tailed t-test, n=5, mean +/- SD for all experiments shown.

5.3.6 Dissemination of B16-luc cells in i∆*efnb2* animals

Next, dissemination changes were analyzed after genetic manipulation of the ephrinB2 – EphB4 system in the host vasculature as well as in tumor cells. i∆*efnb2* animals were injected with B16-luc cells and sacrificed 3 hours post injection. Dissemination of control animals was subtracted from i∆*efnb2* dissemination (∆ number of cells). In i∆*efnb2* animals B16-luc cells disseminate significantly higher to the majority of organs analyzed: Cranium (114 ± 35 cells / organ), forelimbs (287 ± 201 cells / organ), hindlimbs (121 ± 95 cells / organ), spine (62 ± 30 cells / organ), thorax (144 ± 78 cells / organ), liver (60 ± 48 cells / organ), lung (488 ± 206 cells / organ), skin (229 ± 85 cells / organ). However, a preference towards osseous organs was not detected (bone 617 ± 408 cells / organ versus other organs 1084 ± 431 cells / organ, *Figure 32*).

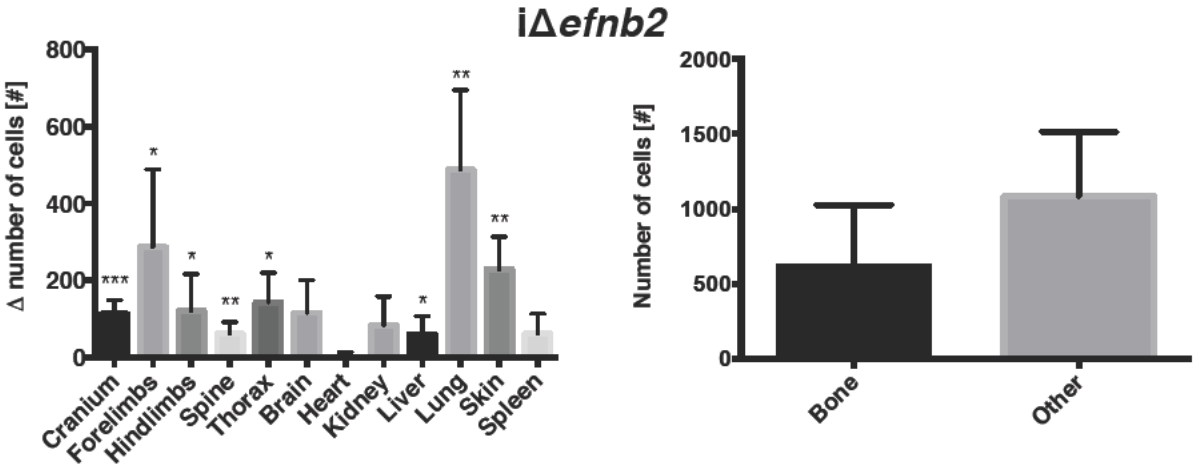

Figure 32 Complete organ dissemination analysis of B16-luc after endothelial ephrinB2 deletion. *A) Endothelial cell specific efnb2 deletion (i∆efnb2) increases cellular dissemination to cranium (p=0.0001), forelimbs (p=0.0141), hindlimbs (p=0.0461), spine (p=0.0052), thorax (p=0.0458), liver (p=0.0432), lung (p=0.0030) and skin (p=0.0061). There is no difference between bone and other*

vascular beds. (Student's two-tailed t-test, n=5, mean +/- SD for all experiments shown).

5.4 Total tumor cell dissemination difference after ephrinB2 – EphB4 signaling manipulation

The strongest total dissemination of tumor cells (sum of individual organs) was observed in i*Δefnb2* animals (1738 ± 806 cells / organ) followed NVP-BHG712 EphB4 kinase inhibition group (1009 ± 334 cells / organ) and the EphB4-FC antibody group (794 ± 464 cells / organ). In the EphB4 overexpression group (B16-luc EphB4) dissemination was significantly reduced (-291 ± 283 cells / organ) compared to EphB4-FC, NVP-BHG712 and i*Δefnb2* groups (*Figure 33*). Conclusively, the experiments show that blocking ephrinB2 – EphB4 interaction results in increased dissemination whereas activation reduced total tumor cell dissemination.

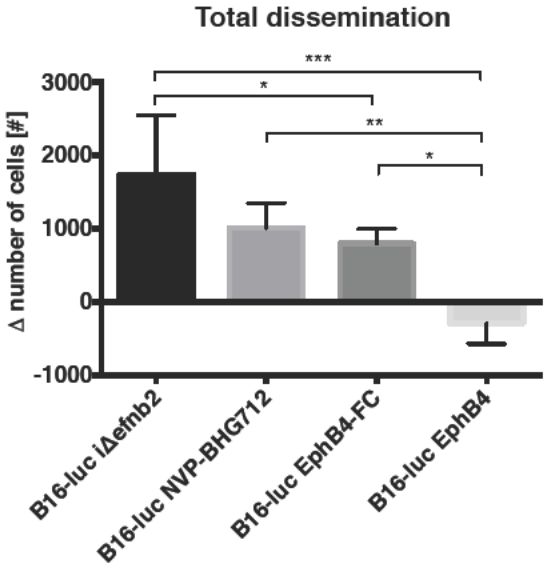

Figure 33 Total B16-luc cell dissemination changes after different ephrinB2 – EphB4 interventions. *Total number of increased / decreased cell dissemination to all organs (sum) showed significant increased cells dissemination in iΔefnb2, NVP-BHG712 and EphB4-FC animals compared to EphB4 overexpressing B16-luc cells. EphB4-FC total cell dissemination was significantly reduced compared to iΔefnb2. One way ANOVA (p=0.0002) with Bonferroni post hoc analysis, n=5, mean +/- SD for all experiments shown.*

5.5 Long-term spinal metastasis characterization

The metastatic potential towards bone of B16 melanoma is an accepted characteristic of this cell line [34]. Spinal metastasis identification was performed using *in-vivo*

bioluminescence imaging and magnetic resonance imaging (MRI). Affected spinal loci could be identified 15 days post injection by *in-vivo* bioluminescence imaging and when animals developed a neurological deficit with MRI.

5.5.1 B16-luc and mB16-luc long-term spinal metastasis formation

In-vivo bioluminescence imaging revealed stronger metastatic potential of mB16-luc tumor cells compared to B16-luc cells. Multifocal tumor lesions were verified with MRI at day of phenotype (*Figure 34 A*). Neurological deficit occurred significantly faster in mB16-luc injected animals (median: 22 days) compared to B16-luc animals (median: 26 days). The number of vertebral tumors (B16-luc: 1.2 ± 0.4472, mB16-luc: 3.8 ± 1.643) and total tumor volume (B16-luc: 2.815mm^3 ± 2.558mm^3, mB16-luc: 9.209mm^3 ± 5.561mm^3) was significantly higher in mB16-luc animals whereas mean tumor volume of single metastasis was unchanged (B16-luc: 2.111mm^3 ± 0.9006mm^3, mB16-luc: 2.454mm^3 ± 1.389mm^3, *Figure 34 B*). Spinal metastasis identification protocol is described in the methods section (*Figure 10*).

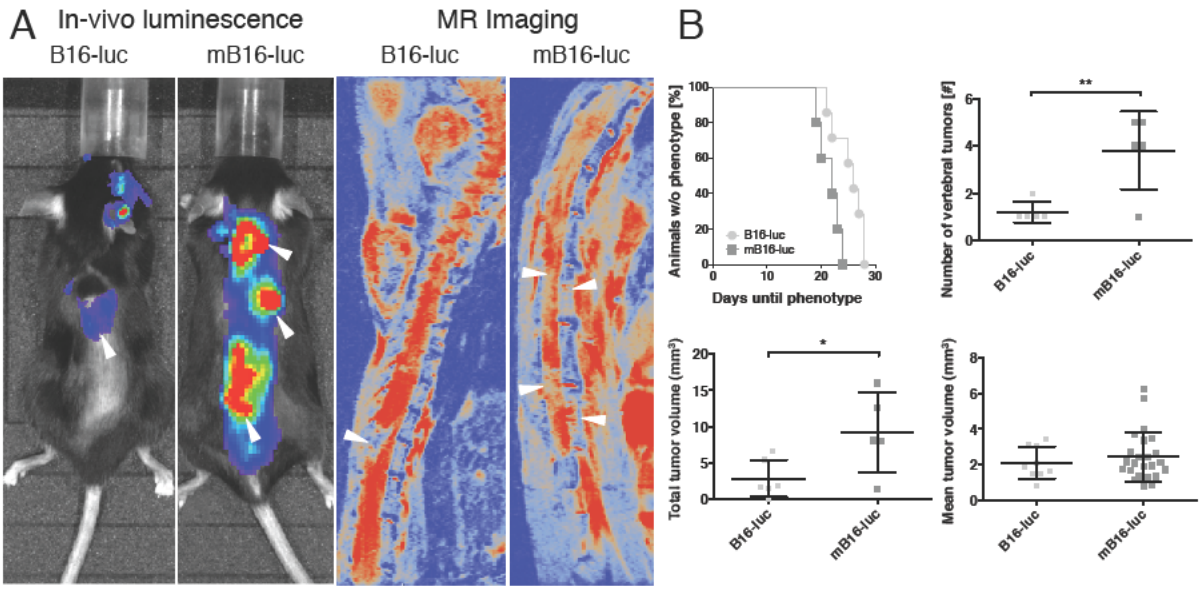

Figure 34 In-vivo bioluminescence and MR imaging identified B16-luc and mB16-luc tumors in the spine. *A) 15 Days post cell injection, tumors located in the spine were observed with bioluminescence. Diverse and more intense loci were found in mB16-luc compared to B16-luc (white arrowheads), MR imaging at day of phenotype shows one spinal compression locus in B16-luc and multiple in mB16-luc (white arrowheads). B) Neurological deficit occurred significantly earlier in mB16-luc compared to B16-luc mice, Log-rank (Mantel-Cox) test (p=0.0186, B16-luc n=7, mB16-luc n=5). The number of vertebral tumors (p=0.0092, B16-luc n=5, mB16-luc n=5) and the total tumor volume (p=0.0321, B16-luc n=5, mB16-luc n=5) was significantly higher in mB16-luc injected mice. Mean tumor size was*

unchanged (p=0.4981, B16-luc n=5, mB16-luc n=5). Student's two-tailed t-test, mean +/- SD for all experiments shown.

After phenotype occurrence we performed multiorgan resection and homogenized the tissues to identify the number of tumor cells grown in individual organs. B16-luc cells preferably grew in osseous organs: cranium ($9.767 \times 10^5 \pm 8.164 \times 10^5$ cells / organ), forelimbs ($1.127 \times 10^6 \pm 1.103 \times 10^6$ cells / organ), hindlimbs ($6.067 \times 10^5 \pm 4.286 \times 10^5$ cells / organ), spine ($1.384 \times 10^6 \pm 1.219 \times 10^6$ cells / organ), thorax ($4.659 \times 10^5 \pm 4.266 \times 10^5$ cells / organ) and their homing tissue skin ($1.415 \times 10^6 \pm 1.508 \times 10^6$ cells / organ). Other organs demonstrated less metastasis (Brain ($1.022 \times 10^5 \pm 3.451 \times 10^4$ cells / organ), heart ($3.037 \times 10^5 \pm 1.425 \times 10^5$ cells / organ), kidney ($1.562 \times 10^5 \pm 6.264 \times 10^4$ cells / organ), liver ($9.216 \times 10^5 \pm 1.473 \times 10^5$ cells / organ), lung ($2.479 \times 10^6 \pm 1.371 \times 10^6$ cells / organ) and spleen ($1.890 \times 10^6 \pm 1.238 \times 10^6$ cells / organ)). Osseous organs ($4.559 \times 10^6 \pm 1.839 \times 10^6$ cells / organ) were tendentially higher metastasized by B16-luc than soft tissue organs ($2.506 \times 10^6 \pm 1.735 \times 10^6$ cells / organ, *Figure 35*).

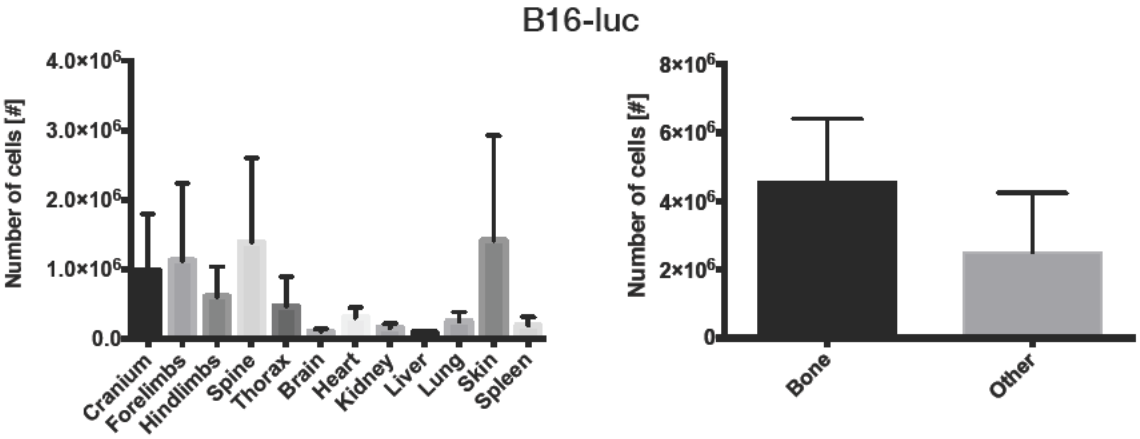

Figure 35 Complete organ metastasis analysis of B16-luc including growth in osseous and other organs. *B16-luc luminescence analyses in different organs at day of neurological deficit showed osseous organs were highly metastasized. Bone metastasis was tendentially higher compared to other organs (p=0.1070). Student's two-tailed t-test, n=5, mean +/- SD for all experiments shown.*

Animals injected with mB16-luc presented the same metastatic tumor burden in a significant shorter time (*Figure 34 B*). Bone organs were 6.97 fold higher affected by mB16-luc metastasis (Bone: $2.299 \times 10^7 \pm 6.539 \times 10^6$ cells / organ, other: $4.352 \times 10^6 \pm 4.615 \times 10^6$ cells / organ). Organ distribution of mB16-luc metastasis was high-

est in Cranium (1.265 x 10^7 ± 1.470 x 10^7 cells / organ) and forelimbs (1.380 x 10^7 ± 1.318 x 10^7 cells / organ). Remaining tissues were comparably low metastasized: hindlimbs (6.175 x 10^5 ± 8.375 x 10^5 cells / organ), spine (2.071 x 10^6 ± 8.375 x 10^6 cells / organ), thorax (1.197 x 10^6 ± 1.268 x 10^6 cells / organ), brain (2.950 x 10^5 ± 3.829 x 10^5 cells / organ), heart (1.823 x 10^5 ± 3.980 x 10^5 cells / organ), kidney (1.872 x 10^5 ± 2.957 x 10^5 cells / organ), liver (2.244 x 10^5 ± 4.810 x 10^5 cells / organ), lung (6.930 x 10^4 ± 4.438 x 10^4 cells / organ), skin (3.392 x 10^6 ± 4.129 x 10^6 cells / organ), spleen (1.890 x 10^3 ± 861 cells / organ) (*Figure 36*).

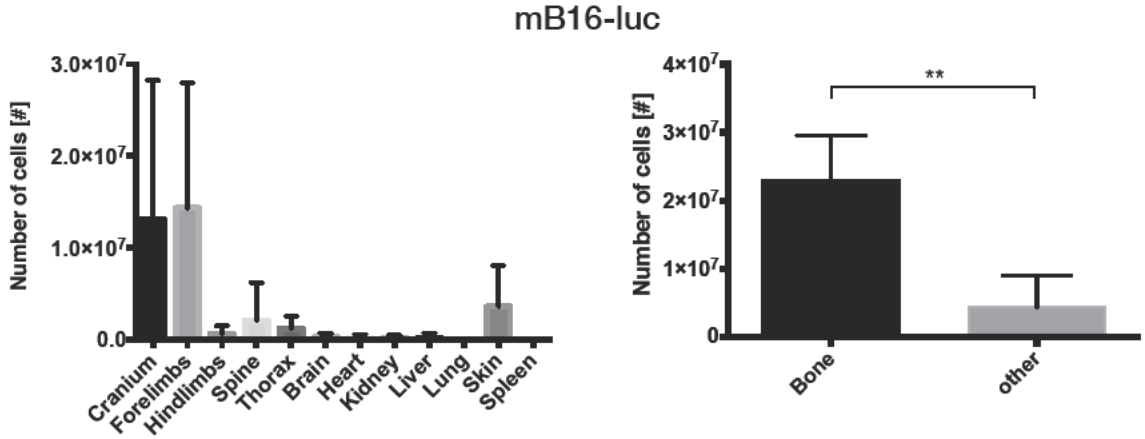

Figure 36 Complete organ mB16-luc metastasis growth analysis, including growth in osseous versus other organs. *Luminescence analysis of mB16-luc at day of neurological phenotype showed high metastatic occurrence in osseous organs. Metastasis formation was significantly higher in bone compared to other organs (p=0.0015). Student's two-tailed t-test, n=5, mean +/- SD for all experiments shown.*

5.5.2 Influence of endothelial ephrinB2 deletion on spinal metastasis formation

Mice lacking ephrinB2 on the endothelium exhibit potentially a higher number of spinal tumors 15 days post tumor cell injection in bioluminescence imaging (white arrowheads). Significant more vertebral tumor loci were identified at day of phenotype (*efnb2*$^{lox/lox}$: 1.2 ± 0.4472, i*Δefnb2:* 3.2 ± 1.643; *Figure 37 A*). Neurological deficit occurred significantly earlier in i*Δefnb2* mice (median: 21 days) compared to controls (median: 26 days). The total tumor volume in the spine was also significantly larger (*efnb2*$^{lox/lox}$: 2.815mm^3 ± 2.558mm^3, i*Δefnb2:* 9.999mm^3 ± 5.596mm^3). However,

mean tumor volume of each metastatic lesion was unchanged (*efnb2*$^{lox/lox}$: 2.111mm^3 ± 0.9006mm^3, i*Δefnb2:* 2.671mm^3 ± 1.61mm^3, *Figure 37 B*).

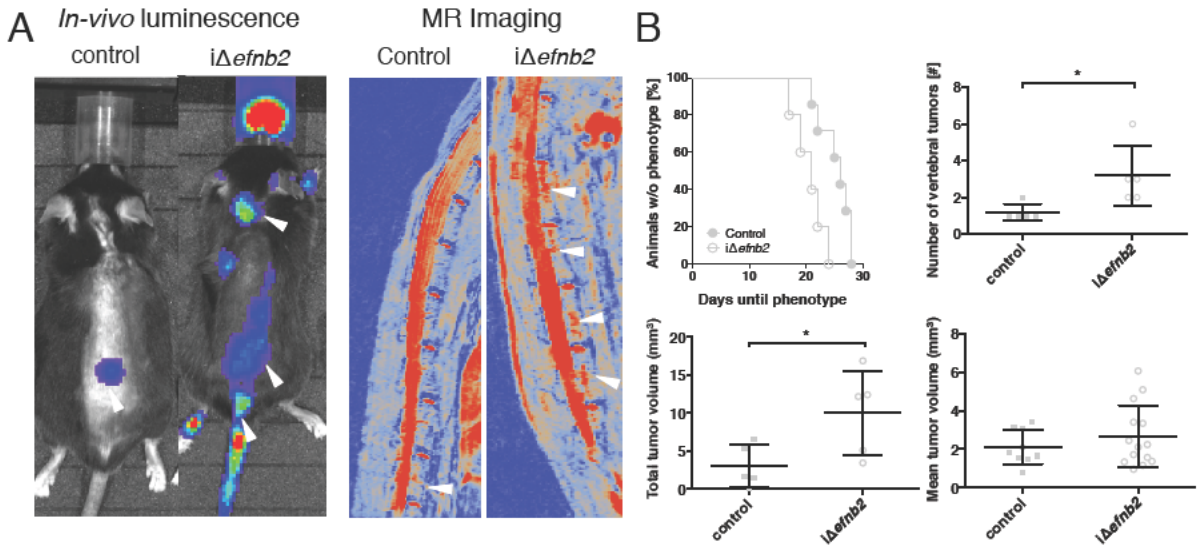

Figure 37 In-vivo bioluminescence and MR imaging identified B16-luc tumors in the spine of control and iΔefnb2 animals. *A) In-vivo bioluminescence 15 days post tumor cell injection showed one spinal metastasis in controls and multi focal metastasis in iΔefnb2 animals (white arrowheads). MRI at day of phenotype revealed metastasis loci of control and iΔefnb2 animals in the spine (white arrowheads). B) Neurological deficit occurred significantly earlier in iΔefnb2 animals (n=5) compared to controls (n=7), Log-rank (Mantel-Cox) test (p=0.0098). Number of vertebral tumors (p=0.0304, control n=5, iΔefnb2 n=5) and total tumor volume (p=0.0372, control n=5, iΔefnb2 n=5) were significant increased in iΔefnb2 animals. Mean tumor volume was unchanged (p=0.3541, control n=5, iΔefnb2 n=5). Student's two-tailed t-test, * p≤0.05, mean +/- SD for all experiments shown.*

After multiorgan resection, homogenization and lysis of the organs, the number of metastasized cells was evaluated. Osseous organs were 5.81 fold (1.910 x 10^7 ± 7.139 x 10^6 cells / organ) higher affected than other organs (3.286 x 10^6 ± 4.551 x 10^6 cells / organ, *Figure 38*). Analyzed organs showed metastasis in: cranium (6.143 x 10^6 ± 7.086 x 10^6 cells / organ), forelimbs (7.213 x 10^6 ± 1.198 x 10^7 cells / organ), hindlimbs (1.252 x 10^7 ± 1.515 x 10^7 cells / organ), spine (2.593 x 10^6 ± 1.442 x 10^6 cells / organ), thorax (9.768 x 10^6 ± 2.036 x 10^7 cells / organ), brain (6.667 x 10^4 ± 1.146 x 10^5 cells / organ), heart (6.971 x 10^5 ± 8.267 x 10^5 cells / organ), kidney (2.6481 x 10^6 ± 4.139 x 10^6 cells / organ), liver (7.083 x 10^6 ± 1.530 x 10^7 cells / organ), lung (2.623 x 10^6 ± 5.624 x 10^5 cells / organ), skin (6.476 x 10^6 ± 6.856 x 10^6 cells / organ), spleen (2.227 x 10^6 ± 4.613 x 10^6 cells / organ) (*Figure 38*).

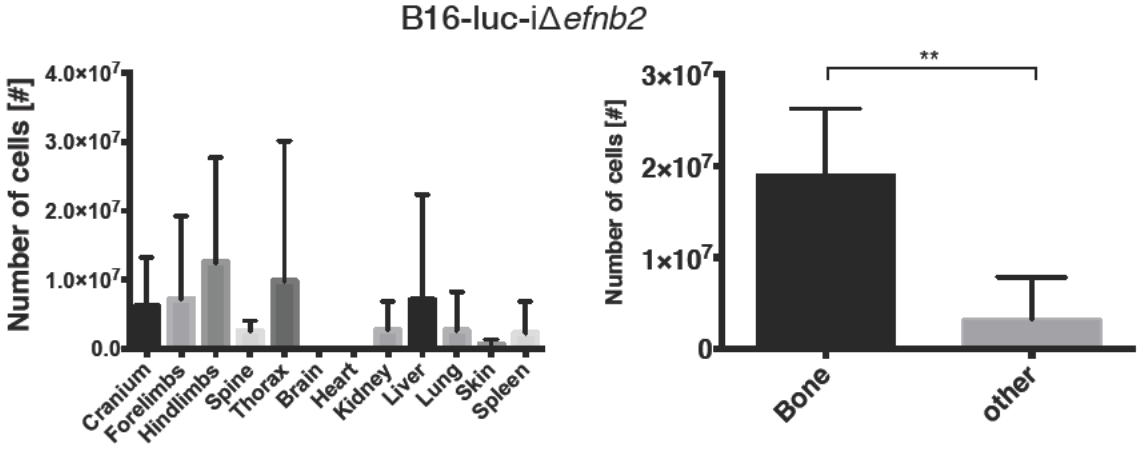

Figure 38 Complete organ metastasis growth analysis of B16-luc cell in iΔefnb2 animals, including growth in osseous and other organs. *B16-luc luminescence analysis in different organs of iΔefnb2 animals indicated growth preference in osseous organs. B16-luc metastasis formation was increased in bone tissue of iΔefnb2 animals (p=0.0031). Student's two-tailed t-test, n=5, mean +/- SD for all experiments shown.*

Comparison of B16-luc bone preference with mB16-luc and B16-luc cells injected in ephrinB2 endothelial depleted mice revealed significant higher bone metastasis in the two later groups (B16-luc: 4.559 x 10^6 ± 1.839 x 10^6, mB16-luc: 2.299 x 10^7 ± 6.539 x 10^6, B16-luc i*Δefnb2:* 1.910 x 10^7 ± 7.139 x 10^6, *Figure 39*).

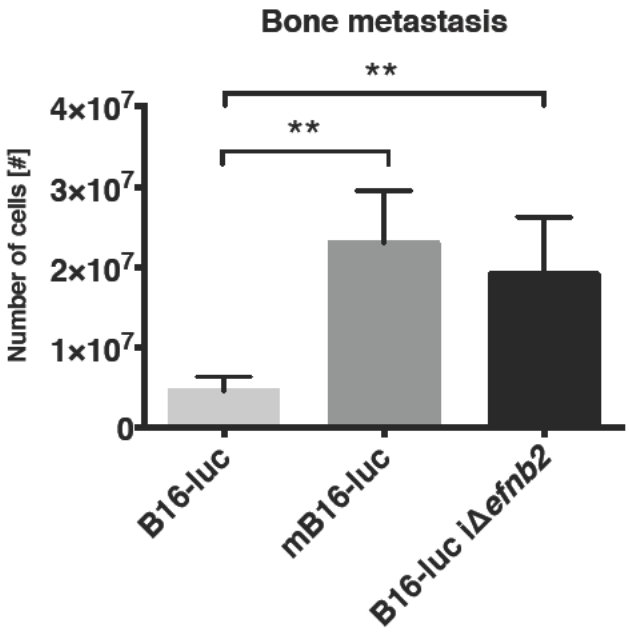

Figure 39 Bone preference of B16-luc, mB16-luc and B16-luc iΔefnb2. *Bone metastasis was sig-*

nificant higher in mB16-luc and B16-luc iΔefnb2 animals compared to B16-luc. One-way ANOVA (p=0.0009) with Bonferroni post hoc analysis, n=5, mean +/- SD for all experiments shown.

5.5.3 Influence of tumor expressed EphB4 on spinal metastasis

In order to investigate the influence of the ephrinB2 – EphB4 system on spinal metastasis in more detail a rescue experiment was performed using EphB4 overexpressing tumor cells. In EphB4 overexpressing B16-luc cells bone specificity of metastasis growth was lost. Only 2 of 5 animals generated a neurological deficit (*Figure 40*). The number of spinal metastatic lesions was also significantly reduced using EphB4 overexpressing B16-luc cells (B16-luc-pLXSN: 1.4 ± 0.5477, B16-luc-EphB4: 0.4 ± 0.5477). Correspondingly, mice injected with B16-luc-EphB4 cells showed a significant delay in the time period until a neurological deficit developed (median: 25 days, B16-luc-pLXSN median: 18). Total tumor volume (B16-luc-pLXSN: 3.645mm^3 ± 2.106mm^3, B16-luc-EphB4: 4.218mm^3 ± 1.638mm^3) and mean tumor volume was unchanged (B16-luc-pLXSN: 2.637mm^3 ± 0.6673mm^3, B16-luc-EphB4: 4.218mm^3 ± 1.638mm^3). Spinal metastasis identification protocol can be found in the methods section (*Figure 10*).

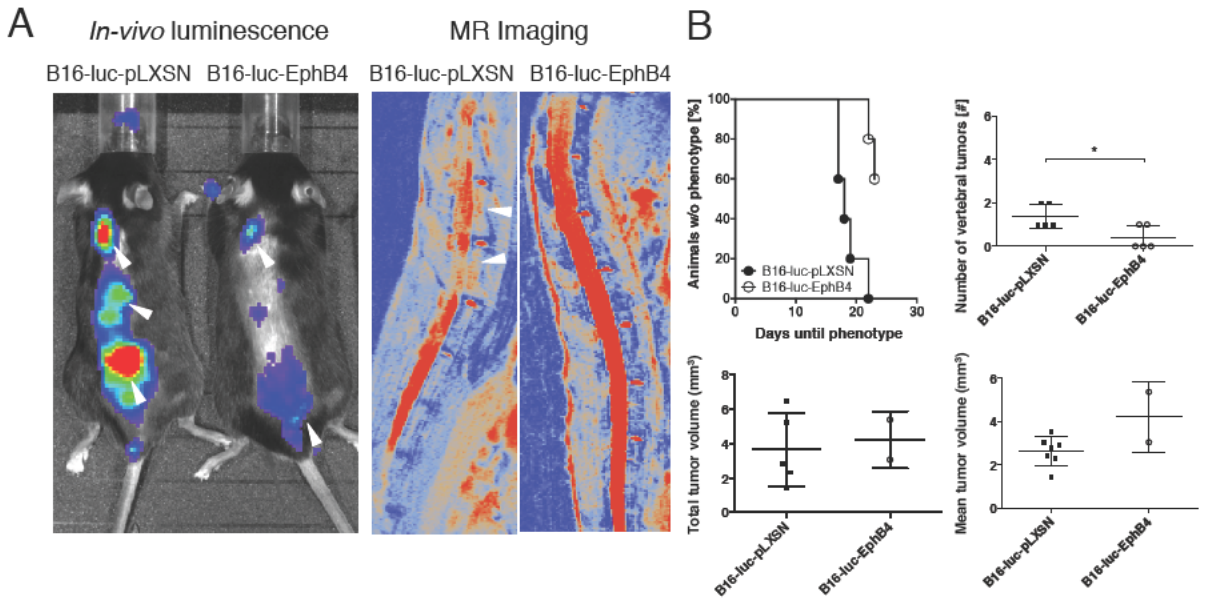

Figure 40 In-vivo bioluminescence and MR imaging identified B16-luc-pLXSN and B16-luc-EphB4 tumors in the spine. *A) In-vivo bioluminescence 15 days post tumor cell injection showed three potential spinal metastasis loci in controls and two in B16-luc-EphB4 injected animals (white arrowheads). MRI at day of phenotype showed two spinal metastasis loci in control animals and none in B16-luc-EphB4 animals (white arrowheads). B) Significant delay in neurological deficit was found in B16-luc-EphB4 animals compared to B16-luc-pLXSN controls, Log-rank (Mantel-Cox) test (p=0.0042,*

*B16-luc-pLXSN n=5, B16-luc-EphB4 n=5). The number of vertebral tumors was significantly decreased in B16-luc-EphB4 animals (p=0.0203, B16-luc-pLXSN n=5, B16-luc-EphB4 n=5). Total (p=0.2126, B16-luc-pLXSN n=5, B16-luc-EphB4 n=5) and mean (p=0.3443, B16-luc-pLXSN n=5, B16-luc-EphB4 n=5) tumor volume was unchanged. Student's two-tailed t-test, * p≤0.05, mean +/- SD for all experiments shown.*

Organ specific metastasis analysis demonstrated B16-luc-pLXSN control cells show the characteristic B16-luc cells osseous growth preference (bone: $7.096 \times 10^7 \pm 1.730 \times 10^7$ cells / organ; soft tissue: $2.799 \times 10^7 \pm 3.101 \times 10^7$ cells / organ, *Figure 41 A*). Accordingly, individual osseous organs showed larger tumor burdens compared to soft tissue organs. The organs: cranium ($2.458 \times 10^6 \pm 1.123 \times 10^6$ cells / organ), forelimbs ($1.518 \times 10^7 \pm 4.691 \times 10^6$ cells / organ), hindlimbs ($4.733 \times 10^7 \pm 1.052 \times 10^7$ cells / organ), spine ($1.044 \times 10^7 \pm 6.119 \times 10^6$ cells / organ), thorax ($7.216 \times 10^6 \pm 4.386 \times 10^6$ cells / organ) showed large tumor cell numbers compared to: brain ($1.374 \times 10^5 \pm 1.768 \times 10^5$ cells / organ), heart ($4.536 \times 10^4 \pm 4.324 \times 10^4$ cells / organ), kidney ($4.353 \times 10^6 \pm 4.813 \times 10^6$ cells / organ), liver ($5.911 \times 10^6 \pm 7.878 \times 10^6$ cells / organ), lung ($2.353 \times 10^5 \pm 2.521 \times 10^5$ cells / organ), skin ($1.460 \times 10^7 \pm 1.506 \times 10^7$ cells / organ) and spleen ($6.115 \times 10^5 \pm 7.295 \times 10^7$ cells / organ).

In contrast, B16-luc-EphB4 overexpressing cells grew equally in osseous ($6.581 \times 10^7 \pm 2.706 \times 10^7$ cells / organ) and soft tissue organs ($6.605 \times 10^7 \pm 5.652 \times 10^7$ cells / organ, *Figure 41 B*). Compared to B16-luc-pLXSN controls, higher tumor burden was found in liver ($2.690 \times 10^7 \pm 2.640 \times 10^7$ cells / organ), lung ($9.495 \times 10^6 \pm 1.271 \times 10^7$ cells / organ) and skin ($4.358 \times 10^7 \pm 3.532 \times 10^7$ cells / organ). The other organs showed relatively even metastasis formation: cranium ($2.555 \times 10^7 \pm 3.205 \times 10^7$ cells / organ), forelimbs ($2.761 \times 10^7 \pm 8.892 \times 10^6$ cells / organ), hindlimbs ($1.399 \times 10^7 \pm 1.531 \times 10^7$ cells / organ), spine ($7.273 \times 10^6 \pm 3.078 \times 10^6$ cells / organ), thorax ($1.054 \times 10^7 \pm 5.106$ cells / organ), brain ($3.602 \times 10^5 \pm 3.582 \times 10^5$ cells / organ), heart ($2.853 \times 10^6 \pm 2.640 \times 10^6$ cells / organ), kidney ($3.050 \times 10^6 \pm 4.119 \times 10^6$ cells / organ) and spleen ($4.545 \times 10^6 \pm 4.366 \times 10^6$ cells / organ).

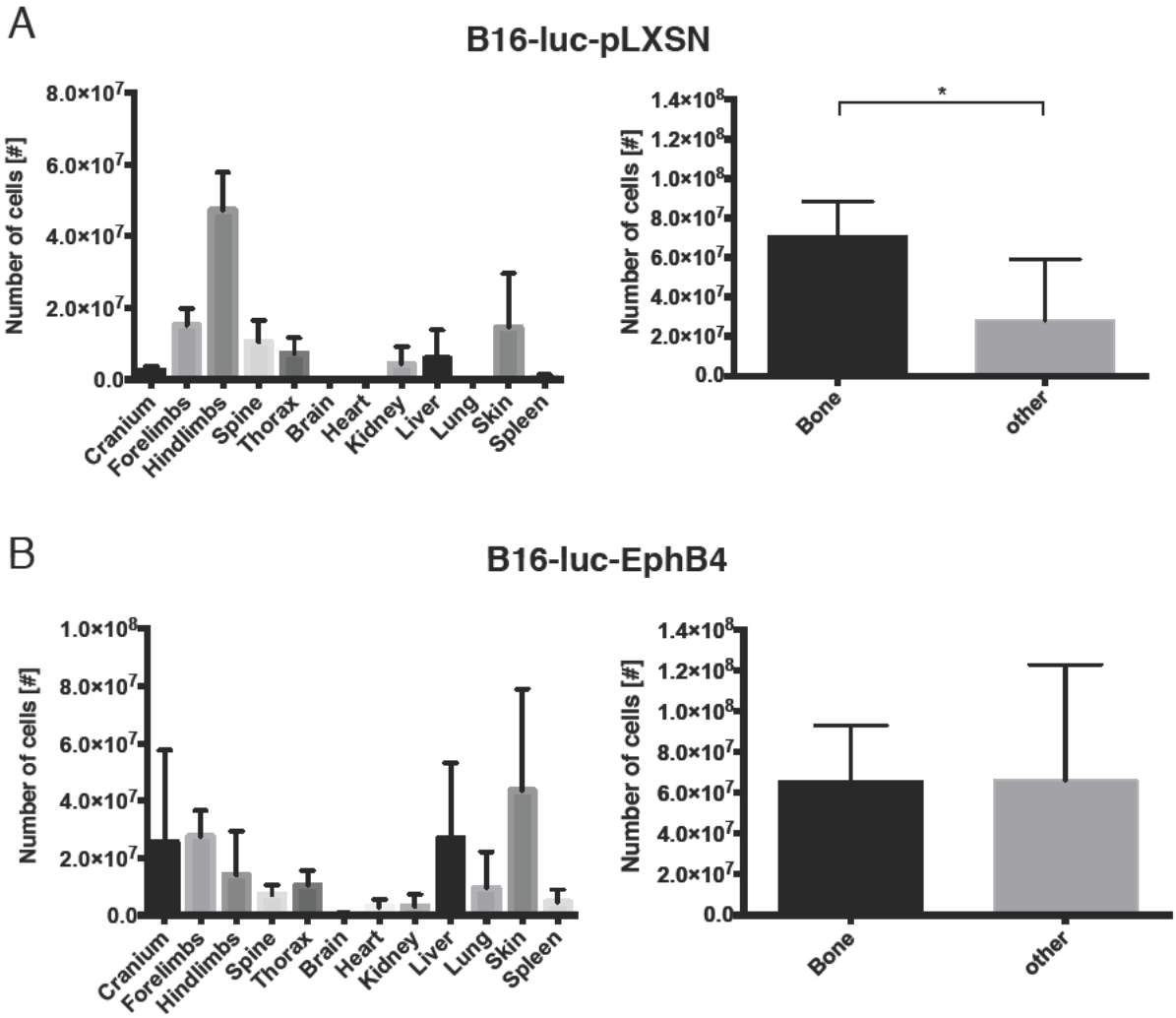

Figure 41: Complete organ metastasis growth analysis of B16-luc-pLXSN cells and B16-luc-EphB4 cells, including growth in bone versus other organs*. A) B16-luc-pLXSN cell metastasis formation in different organs showed increased metastasis in osseous organs. B16-luc-pLXSN metastasis formation in bone was significantly higher compared to non-osseous organs (p=0.0268). B) B16-luc-EphB4 metastasis distribution in different organs showed increased metastasis in liver, lung and skin. B16-luc-EphB4 metastasis formation was equal in bone and soft tissue organs (p=0.9933). Student's two-tailed t-test, n=5, mean +/- SD for all experiments shown.*

6 Discussion

In this Ph.D. thesis we investigated the hypothesis that metastatic cell dissemination is not purely biomechanically driven and endothelial ephrinB2 – tumor cell EphB4 interactions mediate metastatic cell dissemination and long-term metastasis. These hypothesis are based on Patget's seed and soil theory (1889) of metastatic cancer [27]. He proposed that two factors define the site of metastasis: First, only subpopulations of tumor cells acquire cumulative mutations to metastasize (seed features). Second, tumor cells only grow in organ microenvironments, which present adequate survival, migration and growth input (soil features). Fidler (1973) tested the seed hypothesis with B16-F1 mouse melanoma cells. Tumor heterogeneity was narrowed towards a hypermetastatic phenotype by repeated i.v. injection and explantation of lung metastasis [73]. He found massive increase in pulmonary metastasis after *in-vivo* selection independent of *in-vitro* cultivation time and described the highly metastatic B16-F10 cell line [73]. However, this approach accounts for the progeny of cancer cells that survive in a new microenvironment rather then a specific highly metastatic subpopulation [73]. Using a modified fluctuation assay, Fidler and Kripke later showed that individual tumor cell clones form one parent melanoma tumor vary strongly in their metastatic behavior [74]. These findings strengthen the seed hypothesis and identified the individual tumor cell as an important contributor to metastasis. In 1929 James Ewing opposed the seed and soil theory and proposed that metastatic dissemination is purely caused by biomechanical factors [75]. The conflict was elucidated when Zeidman and colleagues observed tumor cell arrest and destruction in mesenteric capillaries of the rabbit [76]. They described different tumor cell types varied in their potential to arrest in the capillary system [76]. However, tail vein injection of B16 melanoma cells results primary in pulmonary metastasis whereas intracardiac injection causes metastasis to different organs, which indicates a large contribution of biomechanical factors [34, 74, 77]. Based on this we introduce a modified arterial injection approach. We injected tumor cells retrograde into the left carotid artery in order to circumvent cranial circulation after cardiac injection via both carotid arteries. Cell tracking and *in-vivo* metastasis formation was analyzed using bioluminescence of firefly luciferase positive B16-luc melanoma clones.

6.1 Methods discussion

6.1.1 Generation of B16-luc cells

The utilization of 2A peptide-based self-cleaving was previously applied to allow for the expression of up to four genes simultaneously on one retroviral vector [78]. In consequence, we infected B16-F1 murine melanoma with a lentiviral vector carrying firefly luciferase – 2A peptide – eGFP – 2A peptide – puromycin resistance gene [79]. Inframe expression of the puromycin resistance gene was verified by adding 5 µg / ml puromycin. GFP expression and firefly luciferase expression were identified by fluorescence microscopy / photometry respectively (*Figure 11*). The superiority of 2A self-cleavage is primarily based on the equivalent expression of all genes fused to each other. Vectors using internal ribosomal entry sites (IRES) or different promoters often show different expression levels of the genes expressed [80]. Cap-dependent expression is usually higher compared to IRES mediated transcription but multiple promoters potentially down regulate their individual expression via promoter interference [81, 82]. Additionally, promoters and IRES sequences are often multiple 100 base pairs long. Their use results in large retroviral vectors. However, large vectors reduce viral titers [83, 84]. Multiple IRES elements on a single vector have different cell line specific effects such as homologous recombination and / or competition of translation factors [85]. The 2A peptide self-cleaving strategy minimizes the problems observed with IRES elements and additional promoters. In contrast to these elements, the 2A cleavage event is described as an autonomous and independent of intracellular factors [86]. The small 19 amino acid peptide does not provide significantly more base pairs to the viral vector constructs and was utilized as an N-terminal tag to identify the cleaved protein on immune blots [86]. This N-terminal residual of the 2A peptide may interfere with proteins sensitive for secondary and tertiary folding and therefore limit their functions. However, there is no evidence for this limitation today [78, 87].

The classically used retroviral long term repeats (LTR) promoter elements are down regulated after *in-vivo* growth [88]. The Ubiquitin B promoters instead showed unchanged expression *in-vivo* over 84 days, where CMV promoter expression declined to background by day 60 [89]. Furthermore, Gill et al., classified Ubiquitin B promoter expression in lung tissue for several months after viral infection [90]. Thus, we embraced the human Ubiquitin C promoter for this study. After explantation of vertebral

bone metastasis, we found GFP expression, luciferase expression and puromycin resistance present in mB16-luc (*Figure 11*). However, luciferase gene expression was moderately down regulated using *in-vitro* luminescence (*Figure 11*). This might be a consequence of the *in-vivo* selection where only a subpopulation of the original heterogeneous tumor cells is capable to metastasize and form tumors [73, 74].

6.1.2 *In-vitro* migration and metastasis

Migration of B16-luc cells was comparable to other reports [91]. Migration speed of mB16-luc cells was significantly faster compared to B16-luc cells (*Figure 14*). Netland and Zetter discovered corresponding effects when they observed, that *in-vivo* selected B16 melanoma cells showed higher chemokinetic motilities [92]. Metastatic subpopulations of other cell types such as murine Lewis lung carcinoma and rat mammary carcinoma cells were shown to migrate faster out of glass capillary tubes [93, 94]. This suggests that higher *in-vitro* cell motility is related to higher metastatic potential [95]. Nevertheless, *in-vitro* migration does not fully resemble the complex process of *in-vivo* extravasation and extracellular matrix invasion. Werling et al., found high metastatic rat BSp73 cells behaved statically during *in-vitro* migration studies [96]. However, when confronted with syngeneic lung tissue fragments, BSp73 cells lost their spherical shape and invaded the tissue rapidly. This highlights the importance of cancer cell interactions with the microenvironment [97]. This is reflected in other *in-vitro* studies where malignant metastatic cells show increased migration properties when seeded on basement membrane components, fibroblastic cell monolayers or endothelial cell monolayers [98-100]. Using mB16-luc *in-vivo,* we found correlating effects of *in-vitro* cell migration with higher dissemination and more metastasis.

Besides migration, proliferation represents another prerequisite for solid metastasis formation. Hence, we analyzed the viability of mB16-luc cells compared to B16-luc cells. In line with Nicolson and Dulski who compared B16-F1, B16-F10 (lung colonizing), B16-O10 (ovary colonizing) and B16-B15b (brain colonizing) cells, we found mB16-luc less viable then B16-luc (B16-F1, *Figure 15*) [101]. Simultaneously, mB16-luc cell migration was significantly enhanced (*Figure 14*). This indicates the selection of a more invasive B16-luc subclone that underwent permanent EMT. EMT is essential for tumors to invade the surrounding tissue. It is speculated that EMT is a critical

morphological change in experimental metastasis to gain extravasation capability [10].

6.1.3 Spontaneous and experimental metastasis models

Basic metastasis research models can be divided in two different types; spontaneous and experimental models [102]. Spontaneous models refer to orthotopically implanted tumors that spontaneously metastasize to distinct organs, including genetically modified animals with spontaneous metastatic phenotypes. In experimental models on the other hand, cancer cells are delivered systemically by direct vascular injection. In this study we developed a modified experimental model based on previous work by Arguello et al.[34].

There are several limitations of the more frequently used experimental metastasis models. Most importantly, they only resemble certain aspects of the metastatic cascade. Direct injection of the tumor cells bypasses the pro-invasive and intravasation steps completely. It is unnecessary for the tumor cells to acquire several mutations and prepare the pro metastatic niche. Spontaneous orthotopic implanted metastasis on the other hand involve all metastatic steps. However, they show an even larger variability than experimental metastasis models and it takes months for metastasis to grow [103, 104]. Commonly, the excess primary tumor burden of orthotopically implanted tumors has to be resected during the course of the experiment. This additional intervention can enhance or suppress metastasis development depending on the model used [104, 105]. Besides these syngeneic models, xenograft models are also widely used. However, a major drawback of xenograft models is the use of immunocompromised mice. Immunodeficiency changes metastatic behavior of human cancer cells and tumor angiogenesis significantly [106-108].

Genetically induced tumor mouse models resemble reliable organ predictable growth. However, most of these mouse models do not metastasize spontaneously [102]. Transgenic mice that do metastasize spontaneously are generally reliable in terms of the affected organs that are metastasized [109]. Drawbacks of genetic mouse models are the long time period until metastasis develops. Approximately 50% of the transgenic mouse population develops metastasis, which makes the investigation laborious and increases the costs of experiments. Moreover, these models probably do not represent the genetic variability of primary human tumors since

only one, maybe two, altered genes generate the phenotype [109-112]. Even though, genetic mouse models were shown to metastasize to bone, no spontaneous spinal metastasis model is described in the literature [109].

Pioneering work by Arguello et al., described reproducible B16 spinal metastasis post intracardiac injection of 100'000 cell [34]. In a modified method of administering the injection we injected the same cell number retrograde into the left carotid artery (*Figure 9*). Post operation the left carotid artery was occluded completely. Cerebral hemodynamics in mice is not altered by the occlusion of one common carotid artery and therefore cerebral ischemia does not develop if one carotid artery is occluded [2, 113]. This injection route was preferred to avoid cardiac arrest or lung collapse found after intracardiac injections. Moreover, this injection was used to reduce cerebral metastasis in order to avoid interference of clinical symptoms induced by spinal and brain metastasis. Arguello et al., demonstrated that intracardiac injection of B16 melanoma causes brain metastasis in 30% of the animals [34]. Direct injection into the left carotid artery circumvents brain circulation because tumor cells enter the bloodstream in the distal aortic arch. Long-term formation of brain metastasis after retrograde left carotid artery injection was low to undetectable (*Figure 35 & Figure 38*). Arguello et al., speculated that arterial injected B16 melanoma cells provoke metastasis primarily due to biophysical effects [34]. We extensively tested this hypothesis by substituting GFP microspheres for cells in our injection protocol.

6.1.4 Dissemination of microspheres and B16-luc cells

For investigating Ewing`s biomechanical filtration hypothesis by injecting biologically inert fluorescent microspheres [75]. Dissemination of either nuclei (7µm) or cell body sized (16µm) microspheres after retrograde left carotid artery injection was analyzed. These two microsphere sizes where evaluated, since the cellular membrane is plastic and cells are able to elongate and minimize their diameter when they arrive in the microvascular system [114, 115]. Right carotid artery injection of 15µm microspheres was already performed in mice to measure cardiac output [116]. Similar to our findings, highest inert particle dissemination was found in kidneys, liver and skin (*Figure 22*) [116]. Quintana et al., injected the microspheres via the right carotid artery and found dissemination to brain and heart, organs less affected in our model (*Figure 22*) [116]. Independent of the diameter size, the injected microbeads rarely passed the first capillary system they arrived in. Only few microbeads were found in the brain,

heart and lung. The experiments with 7 and 16µm microbeads indicate that pure biomechanical filtration after retrograde left carotid artery injection leads to dissemination to kidney, liver and skin (*Figure 22*). In contrast, B16-luc cells following the same injection protocol disseminated primarily to the lung (*Figure 25*). We found generally low numbers of B16-luc cell disseminate, compared to Fidler and Nicolson who tested B16-F10 and B16-F1 cells [117]. Only a small percentage of our lentivirally infected B16-F1 (B16-luc) cells survived in the blood circulation [118]. Survival relies on multiple factors such as platelet recruitment, tumor cell aggregate formation, osmotic stability and endothelial cell adhesion / repulsion [20]. In order to investigate molecular changes in tumor cells that may influence tumor cell dissemination by altering tumor cell - endothelial cell interactions, we chose to profile six major genes involved in this mechanism [119]. Significant up regulation of Ang1 and EphB4 and down regulation of VEGF was found in B16-luc cells compared to B16-F1 (*Figure 12*). We hypothesized that these significant changes in gene expression may be the result of tumor cell heterogeneity [74]. Hence, a global transcription analysis post HIV-based vector infection, showed only modest expression differences caused by retroviral infection alone [120]. In this context, B16-luc cells may represent a subclone of B16-F1 able to survive the puromycin selection.

6.2 Results

6.2.1 B16-luc and mB16-luc long-term spinal metastasis formation

The expression of luciferase allowed the exact localization of metastatic tumors in specific locations. Two weeks post intracardiac injection Arguello et al., identified the formation of solid bone metastasis microscopically [34]. With bioluminescence imaging we verified potential spinal tumor loci 15 days post retrograde left carotid artery injection. Tumor location was mostly lumbar in consensus with the literature (*Figure 34*) [34]. We could confirm that most animals that received 1 x 10^5 cells developed neurological deficits of the hindlimbs and consequently we found the bladder-enlarged due to urinary retention (paragraph 4.6.3, *Figure 10*) [34]. In our experimental setting B16-luc induced neurological deficit in a median of 26 days (*Figure 34*). This 12 day difference possibly occurred due to the use of the B16-F1 G3.26 subclone by Arguello et al,. [34]. This clone showed increased pulmonary metastasis post i.v. injection [34, 121]. The B16-luc clone did not induce spinal metastasis phenotype in

the same time period. However general metastatic growth pattern in different organs was comparable to the earlier findings with the B16-F1 G3.26 subclone (*Figure 35*) [34].

We hypothesized, that sequential metastasis increases aggressiveness and organ selectivity of B16-luc cells. In primary dissemination studies we demonstrate that mB16-luc showed increased unspecific dissemination (*Figure 25*). In long-term studies we found that mB16-luc cells were generally more aggressive and induced more spinal metastatic tumors (*Figure 34*). The primary organ growth specificity for bone microenvironment persisted, without demonstrating a spinal bone specific pattern (*Figure 36*). Stackpole et al., described the effects of B16 melanoma variants selected by one or multiple cycles of spontaneous metastasis in detail [26]. They cultivated subcutaneous, lymph nod, lung, brain, adrenals, and ovary metastasis of first / sequential injections and found an overall increase in secondary metastatic activity, regardless of the primary metastatic site or the number of injection cycles [26]. Organ specific seeding was not accomplished using this method. They speculate the enhanced growth potential or the enhanced secondary dissemination capability to be a major contributor [26]. We show that dissemination capability was increased and contributes to increased aggressiveness of the metastatic cells (*Figure 26*, *Figure 36*). However, enhanced growth was only seen in organs that previously promoted tumor growth. Organs that had initially reduced metastatic frequency again showed low metastatic occurrence in mB16-luc cells (*Figure 36*). Hence, organs with suitable microenvironment (e.g. bone) showed higher tumor loads, spinal tumor number was significantly higher and spinal cord compression occurrence was significantly earlier compared to the primary B16-luc cells (*Figure 34*).

6.2.2 Expression analysis of mB16-luc cells

We speculated that after *in-vivo* selection, the expression pattern of the six angiogenic genes previously analyzed had changed. When mB16-luc expression was compared to B16-F1 we observed a comparable expression profile as seen in B16-luc. EphB4 again was upregulated and VEGF was downregulated (*Figure 12*). This experiments showed that lentiviral infection and selection of a subclone generate larger regulatory changes compared to one time *in-vivo* selection. In line with these findings are the observations by Fidler and Kripke that *in-vitro* selected colonies changed *in-vivo* metastasis more efficiently than sequential *in-vivo* selection [73, 74]. However,

one time *in-vivo* selection had a small but profound effect on B16-luc angiogenic gene transcription machinery (*Figure 13*). Most interestingly, ephrinB2 was up regulated and EphB4 was down regulated respectively in mB16-luc.

6.3 *In-vivo* target validation

The sinusoidal spinal bone microvascular system was characterized by endothelial / pericyte co-staining. No double positive staining of the pericyte marker desmin with CD31 positive vessels was detected (*Figure 19*). Kusumbe et al. show identical observations in juvenile mice with the pericyte / smooth muscle marker α-SMA [122]. Generally, vertebral bone showed few CD31 positive blood vessels consistent with other findings [122]. EphrinB2 was identified on CD31 positive vertebral sinusoids (*Figure 19*). Expression of EphB4 was absent in CD31 positive vertebral structures (*Figure 19*). Isolated bone endothelial cells from bone tissue (femur) showed mRNA expression of both molecules[123]. However, the data does not present absolute expression levels and therefore EphB4 expression might be undetectable by immunohistochemistry.

6.4 *In-vitro* effects of EphB4 overexpression

We generated EphB4 overexpression B16-luc cells by retroviral infection and found decreased cell viability at high cellular densities and increased 2D cell migration (*Figure 16*) [60]. Previous work on *in-vitro* proliferation of B16/EphB4 cells by counting cell numbers or measuring OD (595 nm-650 nm) revealed no significant differences to controls [53]. In contrast, we investigated cell viability at different cell densities and found decreased viability at high cell densities of B16-luc-EphB4 cells (***Figure 18***). Similar effects were found by Noren et al., in MDA-MB-435c mamma carcinoma cells [47]. Downstream analysis revealed ephrinB2-FC depended EphB4 kinase phosphorylation of Abl leads to Crk phosphorylation on Tyr221. Phospho-Crk acts as scaffold protein, blocks other proteins and halts proliferation [50, 52]. EphrinB2 is expressed in B16-luc and mB16-luc cells (*Figure 12*). Thus, EphB4 in B16-luc-EphB4 cells might be activated at high cell densities when cell – cell contact is established. Accordingly, reduced B16/EphB4 survival was found in co-culture of ephrinB2 expressing mouse endothelial cells [53]. B16/EphB4 overexpressing cells showed reduced viability and increased apoptosis compared to controls similar to B16-luc-EphB4 (***Figure 18***) [53]. Besides proliferation, we investigated EphB4 induced migra-

tion effects and found increased 2D migration. Similar to our findings Héroult et al., found EphB4 overexpressing human melanoma to show increased migratory capacity (*Figure 17*) [24]. Xuqing et al. and Héroult et al. characterized this pro-migratory phenotype independent of the EphB4 kinase domain [24, 124]. Two pathways are speculated to be involved in this pro-migratory phenotype: First, EphB4 activation in thyroid papillary carcinoma cells resulted in a phosphorylation loss of focal adhesion kinase (FAK) and Paxillin. Second, EphB3 kinase deficient colorectal tumor cells showed RhoGTPase mediated inhibition of cellular adhesion [124, 125]. Both pathways regulate migration by controlling focal adhesion changes [124, 125]. We further investigated the consequence of this pro-migratory effect *in-vitro* for *in-vivo* cell dissemination.

6.5 B16-luc-pLXSN and B16-luc-EphB4 dissemination

In-vitro migration of B16-luc-EphB4 was significantly enhanced (*Figure 17*). However, initial dissemination of B16-luc-EphB4 was generally reduced compared to B16-luc-pLXSN controls. This data contradicts previous findings, which described a dissemination preference towards lung, liver and kidney after intracardiac injection [24]. In contrast to this study, which investigated dissemination one hour post tumor cell injection, tumor cell dissemination was analyzed 3 hours after tumor cell injection in our experiments. In dissemination experiments, time is a crucial factor: 2 min post intracardiac injection of B16-F10 melanoma, 31% of the tumor cells were found in the lung, 5,7% were found in the liver and 7.6% remained in the blood circulation [117]. Liver dissemination remained constant at 5% one-hour post injection and decreased to 3.6 % after three hours. High liver dissemination probably resembles pure biomechanical filtration [117]. This is further supported by our microsphere injection experiments, were liver was highly affected (*Figure 22*). The reduction after 3 hours to 3.6% disseminated cells in the liver suggests biomechanical filtration effects vanish three hours post injection and cellular surface interactions become important. Liapis et al., found similar effects where tumor cells covered by platelets after three hours started to loosely adhere to lung endothelial cells in electron microscopic observations [126]. Presumably, molecules on platelets such as integrins play a role in tumor cell adhesion (*Figure 3*). Additionally to initial adhesion, recirculation of tumor cells is relevant for their final dissemination. Two minutes after intracardiac injection 7.6% of tumor cells are still circulating. This number decreased to 1.6% and 1.4%, one and three

hours post injection, respectively [117]. Interestingly, one-day past intracardiac injection 0.5% of tumor cells remained recirculating [117]. Three days post injection no circulating tumor cells were identified [117]. Recirculation can be induced biomechanically by shear stress at the endothelial wall or biologically by cellular repulsion. EphB4 intracellular signaling in endothelial cells is known to be repulsive in angiogenesis and neurogenesis [127-129]. This constant repulsion might have resulted in equal organ dissemination phenotype revealed in B16-luc-EphB4 cells (*Figure 28*). This EphB4 mediated repulsion effect might be abolished, when EphB4 is blocked pharmacologically.

6.5.1 Dissemination of B16-luc cells after medical alteration of ephrinB2-EphB4 signalling

Two different pharmacological interventions were carried out to evaluate EphB4 mediated interaction of B16-luc cells with endothelial cells. First, we blocked ephrinB2-binding sites with the EphB4-FC antibody as described previously [24]. However, EphB4-FC was used in multiple studies to induce ephrinB2 forward signaling [44, 49, 50]. Hence, an EphB4 kinase small molecule inhibitor was used as a second strategy. The NVP-BHG712 was evaluated for EphB4 kinase specificity *in-vitro* [72]. Our data shows that non-osseous organ dissemination increased in B16-luc tumor cells when EphB4-FC covered ephrinB2 binding sites (*Figure 31*). Hind limbs, spine and liver showed significantly increased dissemination (*Figure 31*). However, the molecular mechanism of EphB4-FC covering / activating endothelial ephrinB2 and the intracellular consequence of this on disseminating tumor cells remains unknown. Füller et al., showed direct involvement of EphB4 kinase domain to cellular repulsion in endothelial cells [44]. In mixed cultures of ephrinB2 – EphB4 overexpressing porcine aortic endothelial cells, EphB4 overexpressing clones showed agglomeration and island formation, whereas control cells dispersed into each other [44]. However, research in BaF3 murine pro-B-cells showed kinase independent pro adhesive effects of ephrinB2 – EphB4 interaction [130]. To evaluate the involvement of EphB4 kinase in tumor cell – endothelial cell repulsion, we injected the small molecule inhibitor NVP-BHG712 [72]. Upon systemic inhibition of EphB4 kinase using NVP-BHG712 we found significantly higher dissemination to cranium, hind limbs, spine, brain, liver and lung (*Figure 31*). Moreover, dissemination towards bone was reduced leading to an organ-specific dissemination phenotype that resembles the purely biomechanical

dissemination phenotype observed with microspheres (*Figure 22*, *Figure 31*). This could be explained by reduced EphB4 repulsion in tumor cells. Thus, making them more likely to adhere in the first microvascular system they encounter after intra-arterial injection. However, one major issue with small molecule kinase inhibitors is the lack of specificity. Even though NVP-BHG712 selectivity was evaluated *in-vitro, in-vivo* use could cause partial inhibition of other kinases [72]. For this reason, dissemination was evaluated upon induced genetic depletion of ephrinB2 on the endothelium (iΔ*efnb2*).

6.5.2 Dissemination of B16-luc cells in iΔ*efnb2* animals

EphrinB2 endothelial deletion was accomplished by crossing *CDH5*-(Pac)-CreERT^2 animals with ephrinB2 floxed mice. Multiple studies confirmed the successful endothelial specific recombination in the *CDH5*-(Pac)-CreERT^2 mouse model [61, 71, 122, 131]. We controlled our tamoxifen injection protocol using qPCR and Western Blot of lung tissue (*Figure 20*). Knocking out ephrinB2 on the endothelium caused significantly increased dissemination to most organs (cranium, forelimbs, hind limbs, spine, thorax, liver, lung and skin) (*Figure 32*). There was no dissemination preference to non-bony organs indicating a difference between systemic EphB4 kinase inhibition and endothelial specific ephrinB2 depletion. Total dissemination of cells revealed that an extra of 1738 ± 806 tumor cells disseminated in iΔ*efnb2* animals as compared to the experiment with B16-luc-EphB4 cells (*Figure 33*). Summarizing our results, tumor cell – endothelial cell interactions contribute to metastatic tumor cell dissemination in our experiments. Tumor cell dissemination was significantly increased by inhibition of ephrinB2 and EphB4 signaling.

6.6 Influence of endothelial ephrinB2 depletion on spinal metastasis formation

Long-term spinal metastasis formation after endothelial ephrinB2 depletion was significantly increased in our experiments (*Figure 37*). Multi focal spinal metastasis with higher total metastatic volume was observed in these animals. Consequently, earlier neurological deficit was found compared to controls (*Figure 37*). Two factors potentially influence these observations: increased tumor cell extravasation to spinal bone (vascular mechanism) and / or increased tumor growth in spinal bone after tumor cell ex-

travasation (microenvironmental mechanism). Our previous observations described increased tumor cell dissemination after endothelial ephrinB2 depletion and EphB4 kinase inhibition (*Figure 33*). Since only adhesive tumor cells extravasate, higher dissemination could lead to more metastatic lesions [21]. Even though our model does not allow visualization of tumor cell adhesion and extravasation, indirect evidence points to enhanced extravasation as the origin of increased spinal metastasis in i∆*efnb2* animals. Increased number of spinal metastasis and similar average size of the metastases detected imply, that the extravasation process was primarily affected by ephrinB2 depletion, whereas metastasis growth after extravasation remained unchanged (*Figure 37*). However, similar average size was accomplished in a significantly shorter time period. This indicates that in spinal bone, B16-luc cells overcome the anti-tumor effects of endothelial ephrinB2 depletion found by others [49, 131]. Sawamiphak et al. showed endothelial ephrinB2 regulates VEGFR2 internalization signaling. In a glioma tumor model, mice lacking ephrinB2 had significant smaller tumors at the occurrence of neurological deficits and total vascular density was significantly reduced [49]. Additionally, Ramasamy et al. described that bone endothelium differs from normal endothelium. Notch activity promotes angiogenesis in bone in contrast to its inhibitory function in other organs [123, 132]. We therefore speculate that the increased sinusoidal extravasation results in higher tumor cell seeding to spinal bone and multi focal metastasis formation (*Figure 37*). Together with distinct bone specific tumor angiogenesis, spinal metastasis growth may be enhanced after endothelial *efnb2* deletion (*Figure 38*). This bone specific effect is supported by our data showing initial higher lung dissemination in i∆*efnb2* animals but little long-term metastasis (*Figure 31 and Figure 38*). The loose configuration of spinal bone sinusoids are likely to be more affected by the loss of ephrinB2 and may allow tumor cells to extravasate more easily.

6.7 Influence of tumor expressed EphB4 on spinal metastasis

Considering our previous data, we speculated EphB4 overexpression on B16-luc cells would reduce spinal metastasis by enhanced spinal sinusoidal repulsion. Control B16-luc-pLXSN cell showed significantly increased bone specific metastasis (*Figure 41 A)* whereas bone specificity was abolished in B16-luc-EphB4 (*Figure 41 B)*. B16-luc-pLXSN spinal metastasis number was comparable to B16-luc and reduced in B16-luc-EphB4. Correspondingly, B16-luc-EphB4 cells showed a significant delay in

the development of a neurological deficit and reduced spinal metastasis (*Figure 40*). These findings could have two different origins: first, spinal bone sinusoids represent a distinct endothelial subpopulation that repels circulating tumor cells efficiently via tumor cell EphB4 signaling. Second, the spinal bone microenvironment is particularly anti-proliferative to EphB4 overexpressing tumor cells and induces tumor cell dormancy or apoptosis. In dissemination experiments, EphB4 clones showed reduced dissemination resembling the same dissemination phenotype as biologically inactive microbeads (*Figure 22*, *Figure 28*). This observation might be explained by increased repulsion from endothelial cells. However, *in-vitro* studies demonstrated increased tumor cell - tumor cell interactions in response to EphB4 overexpression. A similar effect may occur after intra-arterial injection of EphB4 overexpressing tumor cells leading to an increased occurrence of tumor cell emboli in microvasculature due to increased tumor cell – tumor cell interactions [44]. Correspondingly we found bone-specific metastasis formation was abolished using EphB4 overexpressing B16-luc cells. The hypothetical mechanism underlying this effect may be loss of tumor cell – endothelial cell interactions during the extravasation process [55, 59]. In support of our observations, double transgenic overexpression NeuT/EphB4 mice develop spontaneous lung metastasis, whereas single NeuT transgenic animals show non-malignant tumor growth in the mammary gland without metastasis formation [58, 133]. Hence, EphB4 may represent a trigger to metastatic tumor development and progression in soft tissue. However, changes in metastasis development after extravasation to the bone could also lead to reduced spinal metastasis in response to EphB4 overexpression. Huang et al., described EphB4 overexpressing B16 cells to grow slower in subcutaneous tumor models, whereas EphB4 knock down tumors showed significantly increased tumor size [53]. This effect was caused by decreased angiogenesis and higher vascular density [53]. Contradictory, in MDA-MB-435 human breast cancer cells dominant negative EphB4 overexpression, leaking the intracellular kinase domain, show increased subcutaneous tumor volume [50]. This study found the EphB4 ectodomain to increase endothelial cell migration and angiogenesis [50]. These contradictory findings indicate the variability of EphB4 signaling depending on receptor status, reverse signaling and cell / organ type. Our data shows a comparable mean volume of spinal metastasis between EphB4 overexpressing tumor cells and controls indicating that posthoming effects may only play a minor role in spinal metastasis (*Figure 40*).

7 Conclusions

The most significant findings of this Ph.D. thesis are the following:

1) Metastatic tumor cell dissemination is significantly influenced by biological properties and not purely a biomechanical filtration effect. Inhibition of ephrinB2 – EphB4 signaling induces increased tumor cell dissemination after intra-arterial tumor cell injection in an *in-vivo* metastasis model.

2) Sequential reinjection of metastatic B16-luc cells results in a non-specific pro metastatic phenotype. Secondary metastatic tumor cells show significantly increased, non-specific dissemination in contrast to primary B16-luc cells. However, non-specific dissemination of secondary metastatic tumor cells does not correlate with long-term metastasis formation. Moreover, only the persisting osseous organ metastasis preference of B16-luc was enhanced in mB16-luc.

3) EphrinB2 – EphB4 signaling controls metastasis formation especially in osseous organs including the spinal bone. Endothelial ephrinB2 depletion results in increased spinal metastasis formation with earlier development of neurological deficits. This phenomenon is not a spine specific, but a bone specific effect as EphrinB2 depletion leads to significant increase in metastasis formation in osseous organs. Tumor cell EphB4 overexpression leads to reduced spinal metastasis formation and a significantly later development of neurological deficits. This effect is the consequence of a loss of bone specificity in response to EphB4 downregulation.

8 Acknowlegment

I would like to sincerely thank:

- My supervisor PD. Dr. Marcus Czabanka for giving me the opportunity to work on this exiting topic and to take his time at 6 am to guide and discuss my Ph.D thesis. I am also grateful to Prof. Dr. Peter Vajkoczy for the encouraging support, supervision and guidance.

- Thanks to the Berlin cancer society for providing the Ernst von Leyden fellowship

- My colleges and friends from the Neurosurgery department at Charité medical school. For the creation of motivating work environment.

- My friends form the Neuropathology Institute, for the inspiring and funny coffee breaks and the share of their running enthusiasm.

- Dr. Carsten Grötzinger, Susanne Müller for introduction to the techniques of bioluminescence imaging and magnetic resonance imaging.

- The FEM-Unit 2 and Quarantine 7 for quick actions on mouse breeding that helped me keep my experiments running.

- Our collaborator Prof. Dr. Ralf Adams, MPI for tissue morphogenesis Münster and his technician Inga Schmidt for sharing mice and protocols.

- Benedikt Salmen and the International Graduate Program of Medical Neuroscience office staff for inspiring 5 years Master and Ph.D in Berlin and organizing great off lab activities.

- Special thanks go to my wife Nicole Broggini for the patience and strong support during all these years. You make my world go round. I also thank my parents for constant support, care and encouragement.

9 References

1. Klimo, P., Jr. and M.H. Schmidt, *Surgical management of spinal metastases.* Oncologist, 2004. **9**(2): p. 188-96.
2. Kitagawa, K., et al., *Chronic mild reduction of cerebral perfusion pressure induces ischemic tolerance in focal cerebral ischemia.* Stroke, 2005. **36**(10): p. 2270-4.
3. Ryken, T.C., et al., *Evidence-based review of the surgical management of vertebral column metastatic disease.* Neurosurg Focus, 2003. **15**(5): p. E11.
4. Mina, L.A. and G.W. Sledge, Jr., *Rethinking the metastatic cascade as a therapeutic target.* Nat Rev Clin Oncol, 2011. **8**(6): p. 325-32.
5. Koppenol, W.H., P.L. Bounds, and C.V. Dang, *Otto Warburg's contributions to current concepts of cancer metabolism.* Nat Rev Cancer, 2011. **11**(5): p. 325-37.
6. Kerbel, R.S., *Tumor angiogenesis.* N Engl J Med, 2008. **358**(19): p. 2039-49.
7. Bergers, G. and L.E. Benjamin, *Tumorigenesis and the angiogenic switch.* Nat Rev Cancer, 2003. **3**(6): p. 401-10.
8. Wyckoff, J.B., et al., *Direct visualization of macrophage-assisted tumor cell intravasation in mammary tumors.* Cancer Res, 2007. **67**(6): p. 2649-56.
9. Gerhardt, H. and H. Semb, *Pericytes: gatekeepers in tumour cell metastasis?* J Mol Med (Berl), 2008. **86**(2): p. 135-44.
10. Kalluri, R. and R.A. Weinberg, *The basics of epithelial-mesenchymal transition.* J Clin Invest, 2009. **119**(6): p. 1420-8.
11. Yang, J. and R.A. Weinberg, *Epithelial-mesenchymal transition: at the crossroads of development and tumor metastasis.* Dev Cell, 2008. **14**(6): p. 818-29.
12. Camerer, E., et al., *Platelets, protease-activated receptors, and fibrinogen in hematogenous metastasis.* Blood, 2004. **104**(2): p. 397-401.
13. Gasic, G.J., T.B. Gasic, and C.C. Stewart, *Antimetastatic effects associated with platelet reduction.* Proc Natl Acad Sci U S A, 1968. **61**(1): p. 46-52.
14. Karpatkin, S., et al., *Role of adhesive proteins in platelet tumor interaction in vitro and metastasis formation in vivo.* J Clin Invest, 1988. **81**(4): p. 1012-9.
15. Palumbo, J.S., et al., *Fibrinogen is an important determinant of the metastatic potential of circulating tumor cells.* Blood, 2000. **96**(10): p. 3302-9.
16. Jones, D.S., A.C. Wallace, and E.E. Fraser, *Sequence of events in experimental metastases of Walker 256 tumor: light, immunofluorescent, and electron microscopic observations.* J Natl Cancer Inst, 1971. **46**(3): p. 493-504.
17. Crissman, J.D., et al., *Arrest and extravasation of B16 amelanotic melanoma in murine lungs. A light and electron microscopic study.* Lab Invest, 1985. **53**(4): p. 470-8.

18. Sindelar, W.F., T.S. Tralka, and A.S. Ketcham, *Electron microscopic observations on formation of pulmonary metastases.* J Surg Res, 1975. **18**(2): p. 137-61.

19. Borsig, L., et al., *Heparin and cancer revisited: mechanistic connections involving platelets, P-selectin, carcinoma mucins, and tumor metastasis.* Proc Natl Acad Sci U S A, 2001. **98**(6): p. 3352-7.

20. Gay, L.J. and B. Felding-Habermann, *Contribution of platelets to tumour metastasis.* Nat Rev Cancer, 2011. **11**(2): p. 123-34.

21. Veronika A.M. te Boekhorst, P.F., *Intravital imaging of organ colonization by circulating melanoma cells: steps and strategies of individual cells versus tumor cell clusters*, in *15th International Biennial Congress of the Metastasis Research Society*. 2014, MRS Society: Heidelberg.

22. Ludwig, R.J., et al., *Endothelial P-selectin as a target of heparin action in experimental melanoma lung metastasis.* Cancer Res, 2004. **64**(8): p. 2743-50.

23. Kim, Y.J., et al., *Distinct selectin ligands on colon carcinoma mucins can mediate pathological interactions among platelets, leukocytes, and endothelium.* Am J Pathol, 1999. **155**(2): p. 461-72.

24. Heroult, M., et al., *EphB4 promotes site-specific metastatic tumor cell dissemination by interacting with endothelial cell-expressed ephrinB2.* Mol Cancer Res, 2010. **8**(10): p. 1297-309.

25. Nguyen, D.X., P.D. Bos, and J. Massague, *Metastasis: from dissemination to organ-specific colonization.* Nat Rev Cancer, 2009. **9**(4): p. 274-84.

26. Stackpole, C.W., A.L. Alterman, and E.F. Valle, *B16 melanoma variants selected by one or more cycles of spontaneous metastasis to the same organ fail to exhibit organ specificity.* Clin Exp Metastasis, 1991. **9**(3): p. 319-32.

27. Paget, S., *The distribution of secondary growths in cancer of the breast. 1889.* Cancer Metastasis Rev, 1989. **8**(2): p. 98-101.

28. Roos, E. and K.P. Dingemans, *Mechanisms of metastasis.* Biochim Biophys Acta, 1979. **560**(1): p. 135-66.

29. Aguirre-Ghiso, J.A., *Models, mechanisms and clinical evidence for cancer dormancy.* Nat Rev Cancer, 2007. **7**(11): p. 834-46.

30. Fokas, E., et al., *Metastasis: the seed and soil theory gains identity.* Cancer Metastasis Rev, 2007. **26**(3-4): p. 705-15.

31. Uhr, J.W., et al., *Cancer dormancy: opportunities for new therapeutic approaches.* Nat Med, 1997. **3**(5): p. 505-9.

32. Goss, P.E. and A.F. Chambers, *Does tumour dormancy offer a therapeutic target?* Nat Rev Cancer, 2010. **10**(12): p. 871-7.

33. Dunn, G.P., C.M. Koebel, and R.D. Schreiber, *Interferons, immunity and cancer immunoediting.* Nat Rev Immunol, 2006. **6**(11): p. 836-48.

34. Arguello, F., R.B. Baggs, and C.N. Frantz, *A murine model of experimental metastasis to bone and bone marrow.* Cancer Res, 1988. **48**(23): p. 6876-81.

35. Sanchez-Sweatman, O.H., et al., *Direct osteolysis induced by metastatic murine melanoma cells: role of matrix metalloproteinases.* Eur J Cancer, 1997. **33**(6): p. 918-25.

36. Peinado, H., et al., *Melanoma exosomes educate bone marrow progenitor cells toward a pro-metastatic phenotype through MET.* Nat Med, 2012. **18**(6): p. 883-91.

37. Lisabeth, E.M., G. Falivelli, and E.B. Pasquale, *Eph receptor signaling and ephrins.* Cold Spring Harb Perspect Biol, 2013. **5**(9).

38. Salvucci, O. and G. Tosato, *Essential roles of EphB receptors and EphrinB ligands in endothelial cell function and angiogenesis.* Adv Cancer Res, 2012. **114**: p. 21-57.

39. Dummer, A., *Role of EphB4 and ephrinB2 in breast cancer metastasis final version*, in *Science department*. 2014, University Library Utrecht.

40. Wang, H.U., Z.F. Chen, and D.J. Anderson, *Molecular distinction and angiogenic interaction between embryonic arteries and veins revealed by ephrin-B2 and its receptor Eph-B4.* Cell, 1998. **93**(5): p. 741-53.

41. Gerety, S.S., et al., *Symmetrical mutant phenotypes of the receptor EphB4 and its specific transmembrane ligand ephrin-B2 in cardiovascular development.* Mol Cell, 1999. **4**(3): p. 403-14.

42. Adams, R.H., et al., *Roles of ephrinB ligands and EphB receptors in cardiovascular development: demarcation of arterial/venous domains, vascular morphogenesis, and sprouting angiogenesis.* Genes Dev, 1999. **13**(3): p. 295-306.

43. Klein, R., *Eph/ephrin signalling during development.* Development, 2012. **139**(22): p. 4105-9.

44. Fuller, T., et al., *Forward EphB4 signaling in endothelial cells controls cellular repulsion and segregation from ephrinB2 positive cells.* J Cell Sci, 2003. **116**(Pt 12): p. 2461-70.

45. Marston, D.J., S. Dickinson, and C.D. Nobes, *Rac-dependent trans-endocytosis of ephrinBs regulates Eph-ephrin contact repulsion.* Nat Cell Biol, 2003. **5**(10): p. 879-88.

46. Carmeliet, P., et al., *Abnormal blood vessel development and lethality in embryos lacking a single VEGF allele.* Nature, 1996. **380**(6573): p. 435-9.

47. Shalaby, F., et al., *Failure of blood-island formation and vasculogenesis in Flk-1-deficient mice.* Nature, 1995. **376**(6535): p. 62-6.

48. Zhao, C., et al., *Bidirectional ephrinB2-EphB4 signaling controls bone homeostasis.* Cell Metab, 2006. **4**(2): p. 111-21.

49. Sawamiphak, S., et al., *Ephrin-B2 regulates VEGFR2 function in developmental and tumour angiogenesis.* Nature, 2010. **465**(7297): p. 487-91.

50. Noren, N.K., et al., *The EphB4 receptor suppresses breast cancer cell tumorigenicity through an Abl-Crk pathway.* Nat Cell Biol, 2006. **8**(8): p. 815-25.

51. Ma, X., et al., *Suppression of EphB4 improves the inhibitory effect of mTOR shRNA on the biological behaviors of ovarian cancer cells by down-regulating Akt phosphorylation.* J Huazhong Univ Sci Technolog Med Sci, 2012. **32**(3): p. 358-63.

52. Kumar, S.R., et al., *Receptor tyrosine kinase EphB4 is a survival factor in breast cancer.* Am J Pathol, 2006. **169**(1): p. 279-93.

53. Huang, X., et al., *EphB4 overexpression in B16 melanoma cells affects arterial-venous patterning in tumor angiogenesis.* Cancer Res, 2007. **67**(20): p. 9800-8.

54. Pasquale, E.B., *Eph receptors and ephrins in cancer: bidirectional signalling and beyond.* Nat Rev Cancer, 2010. **10**(3): p. 165-80.

55. Kaenel, P., M. Mosimann, and A.C. Andres, *The multifaceted roles of Eph/ephrin signaling in breast cancer.* Cell Adh Migr, 2012. **6**(2): p. 138-47.

56. Steinle, J.J., et al., *Eph B4 receptor signaling mediates endothelial cell migration and proliferation via the phosphatidylinositol 3-kinase pathway.* J Biol Chem, 2002. **277**(46): p. 43830-5.

57. Yang, N.Y., et al., *The EphB4 receptor-tyrosine kinase promotes the migration of melanoma cells through Rho-mediated actin cytoskeleton reorganization.* J Biol Chem, 2006. **281**(43): p. 32574-86.

58. Munarini, N., et al., *Altered mammary epithelial development, pattern formation and involution in transgenic mice expressing the EphB4 receptor tyrosine kinase.* J Cell Sci, 2002. **115**(Pt 1): p. 25-37.

59. Haldimann, M., et al., *Deregulated ephrin-B2 expression in the mammary gland interferes with the development of both the glandular epithelium and vasculature and promotes metastasis formation.* Int J Oncol, 2009. **35**(3): p. 525-36.

60. Erber, R., et al., *EphB4 controls blood vascular morphogenesis during postnatal angiogenesis.* EMBO J, 2006. **25**(3): p. 628-41.

61. Pitulescu, M.E., et al., *Inducible gene targeting in the neonatal vasculature and analysis of retinal angiogenesis in mice.* Nat Protoc, 2010. **5**(9): p. 1518-34.

62. Feil, R., et al., *Regulation of Cre recombinase activity by mutated estrogen receptor ligand-binding domains.* Biochem Biophys Res Commun, 1997. **237**(3): p. 752-7.

63. Lois, C., et al., *Germline transmission and tissue-specific expression of transgenes delivered by lentiviral vectors.* Science, 2002. **295**(5556): p. 868-72.

64. Dittgen, T., et al., *Lentivirus-based genetic manipulations of cortical neurons and their optical and electrophysiological monitoring in vivo.* Proc Natl Acad Sci U S A, 2004. **101**(52): p. 18206-11.

65. Datwyler, A.L., et al., *SUMO2/3 conjugation is an endogenous neuroprotective mechanism.* J Cereb Blood Flow Metab, 2011. **31**(11): p. 2152-9.

66. Seiler, A.E. and H. Spielmann, *The validated embryonic stem cell test to predict embryotoxicity in vitro.* Nat Protoc, 2011. **6**(7): p. 961-78.

67. Liang, C.C., A.Y. Park, and J.L. Guan, *In vitro scratch assay: a convenient and inexpensive method for analysis of cell migration in vitro.* Nat Protoc, 2007. **2**(2): p. 329-33.

68. Lamprecht, M.R., D.M. Sabatini, and A.E. Carpenter, *CellProfiler: free, versatile software for automated biological image analysis.* Biotechniques, 2007. **42**(1): p. 71-5.

69. Grunwald, I.C., et al., *Hippocampal plasticity requires postsynaptic ephrinBs.* Nat Neurosci, 2004. **7**(1): p. 33-40.

70. Broggini, T., *Molecular mechanisms of PRG3 induced Axon Growth and Regeneration*, in *Institute of molecular biology*. 2005, University of appleid sciences Zürich: Wädenswil. p. 75.

71. Benedito, R., et al., *Notch-dependent VEGFR3 upregulation allows angiogenesis without VEGF-VEGFR2 signalling.* Nature, 2012. **484**(7392): p. 110-4.

72. Martiny-Baron, G., et al., *The small molecule specific EphB4 kinase inhibitor NVP-BHG712 inhibits VEGF driven angiogenesis.* Angiogenesis, 2010. **13**(3): p. 259-67.

73. Fidler, I.J., *Selection of successive tumour lines for metastasis.* Nat New Biol, 1973. **242**(118): p. 148-9.

74. Fidler, I.J. and M.L. Kripke, *Metastasis results from preexisting variant cells within a malignant tumor.* Science, 1977. **197**(4306): p. 893-5.

75. Ewing, J., *Neoplastic Diseases: A Treatise on Tumors*. 1928: W.B. Saunders.

76. Zeidman, I. and J.M. Buss, *Transpulmonary passage of tumor cell emboli.* Cancer Res, 1952. **12**(10): p. 731-3.

77. Fisher, E.R. and B. Fisher, *Circulating cancer cells and metastases.* Int J Radiat Oncol Biol Phys, 1975. **1**(1-2): p. 87-91.

78. Szymczak, A.L., et al., *Correction of multi-gene deficiency in vivo using a single 'self-cleaving' 2A peptide-based retroviral vector.* Nat Biotechnol, 2004. **22**(5): p. 589-94.

79. Broggini, T., et al., *ICAM1 depletion reduces spinal metastasis formation in vivo and improves neurological outcome.* Eur Spine J, 2015.

80. Ryan, M.D. and M. Flint, *Virus-encoded proteinases of the picornavirus super-group.* J Gen Virol, 1997. **78 (Pt 4)**: p. 699-723.

81. Mizuguchi, H., et al., *IRES-dependent second gene expression is significantly lower than cap-dependent first gene expression in a bicistronic vector.* Mol Ther, 2000. **1**(4): p. 376-82.

82. Emerman, M. and H.M. Temin, *Genes with promoters in retrovirus vectors can be independently suppressed by an epigenetic mechanism.* Cell, 1984. **39**(3 Pt 2): p. 449-67.

83. de Felipe, P., et al., *Use of the 2A sequence from foot-and-mouth disease virus in the generation of retroviral vectors for gene therapy.* Gene Ther, 1999. **6**(2): p. 198-208.

84. Klump, H., et al., *Retroviral vector-mediated expression of HoxB4 in hematopoietic cells using a novel coexpression strategy.* Gene Ther, 2001. **8**(10): p. 811-7.

85. Wang, S., et al., *Development of a VSV-G protein pseudotyped retroviral vector system expressing dominant oncogenes from a lacO-modified inducible LTR promoter.* Gene, 1996. **182**(1-2): p. 145-50.

86. Fang, J., et al., *Stable antibody expression at therapeutic levels using the 2A peptide.* Nat Biotechnol, 2005. **23**(5): p. 584-90.

87. Kim, J.H., et al., *High cleavage efficiency of a 2A peptide derived from porcine teschovirus-1 in human cell lines, zebrafish and mice.* PLoS One, 2011. **6**(4): p. e18556.

88. Prasad Alur, R.K., et al., *Modification of multiple transcriptional regulatory elements in a Moloney murine leukemia virus gene transfer vector circumvents silencing in fibroblast grafts and increases levels of expression of the transferred enzyme.* Gene Ther, 2002. **9**(17): p. 1146-54.

89. Yew, N.S., et al., *High and sustained transgene expression in vivo from plasmid vectors containing a hybrid ubiquitin promoter.* Mol Ther, 2001. **4**(1): p. 75-82.

90. Gill, D.R., et al., *Increased persistence of lung gene expression using plasmids containing the ubiquitin C or elongation factor 1alpha promoter.* Gene Ther, 2001. **8**(20): p. 1539-46.

91. Jeong, Y.M., et al., *Imidazole inhibits B16 melanoma cell migration via degradation of beta-catenin.* J Pharm Pharmacol, 2010. **62**(4): p. 491-6.

92. Netland, P.A. and B.R. Zetter, *Metastatic potential of B16 melanoma cells after in vitro selection for organ-specific adherence.* J Cell Biol, 1985. **101**(3): p. 720-4.

93. Young, M.R., M. Newby, and J. Meunier, *Relationships between morphology, dissemination, migration, and prostaglandin E2 secretion by cloned variants of Lewis lung carcinoma.* Cancer Res, 1985. **45**(8): p. 3918-23.

94. Badenoch-Jones, P. and I.A. Ramshaw, *Spontaneous capillary tube migration of metastatic rat mammary adenocarcinoma cells.* Invasion Metastasis, 1984. **4**(2): p. 98-110.

95. Raz, A. and A. Ben-Ze'ev, *Cell-contact and -architecture of malignant cells and their relationship to metastasis.* Cancer Metastasis Rev, 1987. **6**(1): p. 3-21.

96. Werling, H.O., et al., *Adhesion and spreading characterization of a rat tumor cell system exhibiting different metastatic behavior.* Invasion Metastasis, 1985. **5**(5): p. 270-94.

97. Paku, S., et al., *Invasive activities of metastasizing and nonmetastasizing tumor cell variants in vitro. II. Studies on confrontations with aorta, vein, ductus thoracicus, diaphragm, and lung.* Anticancer Res, 1986. **6**(1): p. 17-26.

98. McCarthy, J.B., et al., *The role of cell adhesion proteins--laminin and fibronectin--in the movement of malignant and metastatic cells.* Cancer Metastasis Rev, 1985. **4**(2): p. 125-52.

99. Verschueren, H., D. Dekegel, and P. De Baetselier, *Difference in motile behavior between lymphoma variants with different invasive and metastatic capabilities.* Invasion Metastasis, 1988. **8**(1): p. 31-44.

100. Kramer, R.H. and G.L. Nicolson, *Interactions of tumor cells with vascular endothelial cell monolayers: a model for metastatic invasion.* Proc Natl Acad Sci U S A, 1979. **76**(11): p. 5704-8.

101. Nicolson, G.L. and K.M. Dulski, *Organ specificity of metastatic tumor colonization is related to organ-selective growth properties of malignant cells.* Int J Cancer, 1986. **38**(2): p. 289-94.

102. Khanna, C. and K. Hunter, *Modeling metastasis in vivo.* Carcinogenesis, 2005. **26**(3): p. 513-23.

103. Hoffman, R.M., *Orthotopic metastatic mouse models for anticancer drug discovery and evaluation: a bridge to the clinic.* Invest New Drugs, 1999. **17**(4): p. 343-59.

104. Khanna, C., et al., *An orthotopic model of murine osteosarcoma with clonally related variants differing in pulmonary metastatic potential.* Clin Exp Metastasis, 2000. **18**(3): p. 261-71.

105. Bibby, M.C., *Orthotopic models of cancer for preclinical drug evaluation: advantages and disadvantages.* Eur J Cancer, 2004. **40**(6): p. 852-7.

106. Garofalo, A., et al., *Comparative study on the metastatic behavior of human tumors in nude, beige/nude/xid and severe combined immunodeficient mice.* Invasion Metastasis, 1993. **13**(2): p. 82-91.

107. Mueller, B.M. and R.A. Reisfeld, *Potential of the scid mouse as a host for human tumors.* Cancer Metastasis Rev, 1991. **10**(3): p. 193-200.

108. Takizawa, Y., et al., *New immunodeficient (nude-scid, beige-scid) mice as excellent recipients of human skin grafts containing intraepidermal neoplasms.* Arch Dermatol Res, 1997. **289**(4): p. 213-8.

109. Garabedian, E.M., P.A. Humphrey, and J.I. Gordon, *A transgenic mouse model of metastatic prostate cancer originating from neuroendocrine cells.* Proc Natl Acad Sci U S A, 1998. **95**(26): p. 15382-7.

110. Grippo, P.J. and E.P. Sandgren, *Highly invasive transitional cell carcinoma of the bladder in a simian virus 40 T-antigen transgenic mouse model.* Am J Pathol, 2000. **157**(3): p. 805-13.

111. Jansen, A.P., et al., *Protein kinase C-epsilon transgenic mice: a unique model for metastatic squamous cell carcinoma.* Cancer Res, 2001. **61**(3): p. 808-12.

112. Jeffers, M., et al., *The mutationally activated Met receptor mediates motility and metastasis.* Proc Natl Acad Sci U S A, 1998. **95**(24): p. 14417-22.

113. Hecht, N., et al., *Cerebral hemodynamic reserve and vascular remodeling in C57/BL6 mice are influenced by age.* Stroke, 2012. **43**(11): p. 3052-62.

114. Parmaksiz, G., et al., *Antiangiogenic therapy inhibits the recruitment of vascular accessory cells to the perivascular niche in glioma angiogenesis.* J Vasc Res, 2014. **51**(2): p. 102-9.

115. Vajkoczy, P., et al., *Multistep nature of microvascular recruitment of ex vivo-expanded embryonic endothelial progenitor cells during tumor angiogenesis.* J Exp Med, 2003. **197**(12): p. 1755-65.

116. Quintana, A., E. Raczka, and A. Bonaccorsi, *Cardiac output distribution measured with radioactive microspheres in the mouse.* Pharmacol Res Commun, 1979. **11**(3): p. 245-52.

117. Fidler, I.J. and G.L. Nicolson, *Organ selectivity for implantation survival and growth of B16 melanoma variant tumor lines.* J Natl Cancer Inst, 1976. **57**(5): p. 1199-202.

118. Fisher, B. and E.R. Fisher, *The organ distribution of disseminated 51 Cr-labeled tumor cells.* Cancer Res, 1967. **27**(2): p. 412-20.

119. Adams, R.H. and K. Alitalo, *Molecular regulation of angiogenesis and lymphangiogenesis.* Nat Rev Mol Cell Biol, 2007. **8**(6): p. 464-78.

120. Mitchell, R., et al., *Global analysis of cellular transcription following infection with an HIV-based vector.* Mol Ther, 2003. **8**(4): p. 674-87.

121. Stackpole, C.W., A.L. Alterman, and D.M. Fornabaio, *Growth characteristics of clonal cell populations constituting a B16 melanoma metastasis model system.* Invasion Metastasis, 1985. **5**(3): p. 125-43.

122. Kusumbe, A.P., S.K. Ramasamy, and R.H. Adams, *Coupling of angiogenesis and osteogenesis by a specific vessel subtype in bone.* Nature, 2014. **507**(7492): p. 323-8.

123. Ramasamy, S.K., et al., *Endothelial Notch activity promotes angiogenesis and osteogenesis in bone.* Nature, 2014. **507**(7492): p. 376-80.

124. Xuqing, W., et al., *EphB4 is overexpressed in papillary thyroid carcinoma and promotes the migration of papillary thyroid cancer cells.* Tumour Biol, 2012. **33**(5): p. 1419-27.

125. Miao, H., et al., *Inhibition of integrin-mediated cell adhesion but not directional cell migration requires catalytic activity of EphB3 receptor tyrosine kinase. Role of Rho family small GTPases.* J Biol Chem, 2005. **280**(2): p. 923-32.

126. Lapis, K., S. Paku, and L.A. Liotta, *Endothelialization of embolized tumor cells during metastasis formation.* Clin Exp Metastasis, 1988. **6**(1): p. 73-89.

127. Oike, Y., et al., *Regulation of vasculogenesis and angiogenesis by EphB/ephrin-B2 signaling between endothelial cells and surrounding mesenchymal cells.* Blood, 2002. **100**(4): p. 1326-33.

128. Wang, H.U. and D.J. Anderson, *Eph family transmembrane ligands can mediate repulsive guidance of trunk neural crest migration and motor axon outgrowth.* Neuron, 1997. **18**(3): p. 383-96.

129. Krull, C.E., et al., *Interactions of Eph-related receptors and ligands confer rostrocaudal pattern to trunk neural crest migration.* Curr Biol, 1997. **7**(8): p. 571-80.

130. Sakamoto, H., et al., *Cell adhesion to ephrinb2 is induced by EphB4 independently of its kinase activity.* Biochem Biophys Res Commun, 2004. **321**(3): p. 681-7.

131. Wang, Y., et al., *Ephrin-B2 controls VEGF-induced angiogenesis and lymphangiogenesis.* Nature, 2010. **465**(7297): p. 483-6.

132. Benedito, R., et al., *The notch ligands Dll4 and Jagged1 have opposing effects on angiogenesis.* Cell, 2009. **137**(6): p. 1124-35.

133. Muller, W.J., et al., *Single-step induction of mammary adenocarcinoma in transgenic mice bearing the activated c-neu oncogene.* Cell, 1988. **54**(1): p. 105-15.

10 Abbreviations

Commonly used abbreviations are listed underneath in Table 11 Abbreviations.

Table 11 Abbreviations

Abbreviations	
A	adult
BME	2-Mercaptoethanol
BW	Body weight
cDNA	Complementary DNA
CNS	central nervouse system
CSS	candidate sphingomyelin synthases
DAPI	4',6-diamidino-2-phenylindole
DMEM	Dulbecco's Modified Eagle's Medium
DMSO	Dimethoxysulfoxide
DNA	Deoxyribonucleic acid
E	embryonic
ECL	Enhanced chemiluminescence
ECO	ecotropic
EDTA	Ethylenediaminetetraacetic acid
EGFP	enhanced green fluorescent protein
EMT	Epithelial–mesenchymal transition
FCS	fetal calf serum
G6Pase	glucose-6-phosphatase
GAPDH	Glyceraldehyde 3-phosphate dehydrogenase
GTPase	guanosine triphosphatase
HBS	HEPES buffered saline
HC	horse serum
HRP	Horseradish peroxidase
IP	Intraperitoneal
IRES	Internal ribosomal entry sites
MOPS	3-(N-morpholino)propanesulfonic acid
MRI	Magnetic resonance imaging
mRNA	Messenger RNA
MTT	3-(4,5-dimethylthiazol-2-yl)-2,5-diphenyltetrazolium bromide
O/N	Over night
P	postnatal
PBS	Phosphate buffered saline
PEG	Polyethylene glycol
PFA	paraformaldehyde
PNS	peripheral nerve system
PVDF	Polyvinylidene fluoride
qPCR	Quantitative poly chain reaction
RLU	Relative light unit
RNA	Ribonucleic acid
RT	Room temperature
RT-PCR	Real time poly chain reaction
SD	Standard deviation
SDS-PAGE	sodium dodecyl sulfate polyacrylamide gel electrophoresis

siRNA	small interfering ribonucleic acid
SMS	sphingomyelin synthases
SOC	one shot cells and growth medium
TAE	Tris-acetate buffer
Tris	2-Amino-2-hydroxymethyl-propane-1,3-diol

11 Curriculum vitae

Mein Lebenslauf wird aus datenschutzrechtlichen Gründen in der elektronischen Version meiner Arbeit nicht veröffentlicht

12 Own Publications

1) **Broggini T**, Wüstner M, Harms C, Stange L, Blaes J, Thomé C, Harms U, Mueller S, Weiler M, Wick W, Vajkoczy P, Czabanka M. NDRG1 overexpressing glioma are characterized by reduced tumor vascularisation and resistance to antiangiogenic treatment. **Can. Letters,** Accepted.
2) **Broggini T,** Czabanka M, Piffko A, Harms C, Hoffmann C, Mrowka R, Wenke F, Deutsch U, Grötzinger C, Vajkoczy P. ICAM1 depletion reduces spinal metastasis formation in vivo and improves neurological outcome. **Eur Spine J.** 2015 Feb 25.
3) Czabanka M, Bruenner J, Parmaksiz G, **Broggini T**, Topalovic M, Bayerl SH, Auf G, Kremenetskaia I, Nieminen M, Jabouille A, Mueller S, Harms U, Harms C, Koch A, Heppner FL, Vajkoczy P. Combined temozolomide and sunitinib treatment leads to better tumour control but increased vascular resistance in O(6)-methylguanine methyltransferase-methylated gliomas. **Eur J Cancer**. 2013 Mar 14.

13 Affidavit

"I, Thomas Broggini certify under penalty of perjury by my own signature that I have submitted the thesis on the topic Effects of ephrinB2 – EphB4 signaling on spinal metastasis. I wrote this thesis independently and without assistance from third parties, I used no other aids than the listed sources and resources.

All points based literally or in spirit on publications or presentations of other authors are, as such, in proper citations (see "uniform requirements for manuscripts (URM)" the ICMJE www.icmje.org) indicated. The sections on methodology (in particular practical work, laboratory requirements, statistical processing) and results (in particular images, graphics and tables) correspond to the URM (s.o) and are answered by me. My interest in any publications to this dissertation correspond to those that are specified in the following joint declaration with the responsible person and supervisor. All publications resulting from this thesis and which I am author correspond to the URM (see above) and I am solely responsible.

The importance of this affidavit and the criminal consequences of a false affidavit (section 156,161 of the Criminal Code) are known to me and I understand the rights and responsibilities stated therein.

Date Signature

Declaration of any eventual publications

Thomas Broggini had the following share in the following publications:

Publication 1: Thomas Broggini, Marcus Czabanka, Andras Piffko, Christoph Harms, Christian Hoffmann, Ralf Mrowka, Frank Wenke, Urban Deutsch, Carsten Grötzinger, Peter Vajkoczy. ICAM1 depletion reduces spinal metastasis formation in vivo and improves neurological outcome. European Spine Journal, European Spine Journal, Eur Spine J. 2015 Feb 25. [Epub ahead of print] PMID: 25711910

Contribution in detail (please briefly explain): Performed experiments, analysed data, designed figures and wrote/revised the manuscript

Publication 2: Nicolai E. Savaskan, Zheng Fan, Thomas Broggini, Michael Buchfelder1 & Ilker Y. Eyüpoglu. Neurodegenerative action in brain tumors: Glutamate and xCT/System xc^{-}in the limelight. Current Neuropharmacology, in press.

Contribution in detail (please briefly explain): prepared figures and revised the manuscript

Publication 3: Czabanka M, Bruenner J, Parmaksiz G, Broggini T, Topalovic M, Bayerl SH, Auf G, Kremenetskaia I, Nieminen M, Jabouille A, Mueller S, Harms U, Harms C, Koch A, Heppner FL, Vajkoczy P. Combined temozolomide and sunitinib treatment leads to better tumour control but increased vascular resistance in O(6)-methylguanine methyltransferase-methylated gliomas. Eur J Cancer. 2013.

Contribution in detail (please briefly explain): Performed experiments, analysed data and revised the manuscript

Publication 4: Broggini T, Nitsch R, Savaskan NE. Plasticity-related gene 5 (PRG5) induces filopodia and neurite growth and impedes lysophosphatidic acid- and nogo-A-mediated axonal retraction. Mol Biol Cell. 2010

Contribution in detail (please briefly explain): Performed experiments, analysed data and revised the manuscript

Signature, date and stamp of the supervising University teacher

_____

Signature of the doctoral candidate

_____